ICMRM 2023 Singapore

The 17th International Conference on

Magnetic Resonance Microscopy

27-31 August 2023, Singapore

Platinum Sponsors

Gold Sponsors

Paul Callaghan Young Investigator Award Sponsor

Special Thanks

Organizer

Partners

BRUKER

NMR

Reduced Helium Consumption

Bruker innovations advance research while reducing helium consumption.

Ascend Evo 1.0 GHz reduces helium consumption by 3-fold with a hold-time of 130 days

HelioSmart Recovery collects helium boil-off and has a typical recovery rate of 80-85%

For more information please visit www.bruker.com

Innovation with Integrity

WELCOME

Welcome to Singapore and welcome to the 17th International Conference on Magnetic Resonance Microscopy! We are glad and honoured to host the conference in the Asia-Pacific, a dynamic and culturally diverse region where East meets West. Singapore has been an international hub for centuries and is known for its strengths in trade and technology development. So, it is fitting that it is also a gathering place for international scientists and engineers to exchange new ideas.

Thank you to the sponsors and exhibitors, we are very grateful for your support. This has allowed us to lift the standard of the catering and beverages so we ask all attendees to show their appreciation by visiting the booths.

Most of all, we are grateful to you for travelling all this way to participate and for providing an exciting range of talks and posters. We hope that you will enjoy your stay, the scientific programme, and the discussions after talks or in front of posters. We also hope that you will enjoy the city, the food, and the social programme.

Shaoying Huang and Robin Dykstra

Conference Co-Chairs

ORGANIZING COMMITTEE

General Co-Chairs

Shaoying Huang
Singapore University of Technology and Design (SUTD)

Robin Dykstra
Victoria University of Wellington

Technical Program

Petrik Galvosas
Victoria University of Wellington

Sponsorship & Exhibition

Sergei Obruchkov
Resonint

Web & Design

Tingou Liang
SUTD

Local Arrangements

Pyae P. A.
@ Elvis K. Lin
SUTD

Jinghan Heng
SUTD

Yuyue Zhang
National University of Singapore

FULL PROGRAM

Aug. 27, 2023, Sunday		
10:30	Arrivals and registration	Campus center
13:00	**Educational Talk 1** Chair: Konstantin Momot, Queensland University of Technology	
13:00	*Meghan Halse, University of York* Parahydrogen-induced polarisation in NMR spectroscopy and imaging	Auditorium
14:00	*Luisa Ciobanu, NeuroSpin/CEA* Opportunities offered by ultra-high field MRI	
15:00	**Coffee break**	Campus center
15:30	**Educational Talk 2** Chair: Yi-Qiao Song, Harvard University	
15:30	*Michael Johns, University of Western Australia* Applications of (LF) Magnetic Resonance in Chemical Engineering	Auditorium
16:30	*Hilary Fabich, ABQMR, Inc.* Outside the lab: Unique applications of NMR	
17:30	**Break**	Campus center
17:45	**Plenary Lecture** Chair: Melanie Britton, University of Birmingham	
	William S. Price, Western Sydney University The Versatility of NMR Diffusion Measurements	Auditorium
18:45	**Break**	Campus center
19:00	**Welcome Reception**	Jackie Chan Place/ Campus center

Aug. 28, 2023, Monday		
08:45	**Opening** Guest of Honor: Prof. Chee Kai Chua, Associate Provost, Research, SUTD	Auditorium
09:30	**Session 1 – 28AM:** Biomedical I Chair: Bernard Siow, the Francis Crick Institute	
09:30 INV 1	*Le Roy Chong, Changi General Hospital* 3D MRI With CT-Like Bone Contrast – How I Do It	Auditorium
10:00 O1	*Di Zhang, Beijing U. of Posts and Telecomm.* Anatomy-guided and point-cloud-based deep learning framework for superficial white matter tractography parcellation	
10:15 O2	*Zaimin Zhu, Beijing U. of Posts and Telecomm.* Attention-based q-space Deep Learning: Fast Diffusion Magnetic Resonance Imaging with Varied Sampling Strategies	
10:30 O3	*Weng Kung Peng, Songshan Lake Materials Lab.* NMR-based traits: The Next Generation of Precision Medicine	
10:45	**Coffee break**	Campus Center
11:15	**Session 2 – 28NOON:** Diffusion in biology & medical applications Chair: Siegfried Stapf, TU Ilmenau	
11:15 INV 2	*Yang Xia, Oakland University* The First Study of Biomaterials by Nuclear Magnetic Resonance	Auditorium
11:45 O4	*Zofia Schneider, AGH University of Krakow* The correlation between healthy aging and DTI metrics of the brain regions	
12:00 O5	*Daniel Topgaard, Lund University* Double-rotation gradient waveforms and nonparametric distributions of frequency-dependent diffusion tensors	
12:15 O6	*Arabella Cox, Francis Crick and UCL* Fast Diffusion Exchange Spectroscopic Imaging (fDExSI) MRI - fast quantification diffusion exchange for cell permeability imaging.	
12:30 O7	*Yi-Qiao Song, Harvard University* Full Diffusion Tensor Distribution to Characterize Tissue Microstructure and Types in Brain Tumors	
12:45 O8	*Einar Fridjonsson, The U. of Western Australia* Rapid monitoring of cleaning efficiency of fouled hollow fiber membrane module via non-invasive NMR diffraction technique	
13:00 – 14:00	**Lunch**	Campus Center
14:00	**Session 3 – 28NOON:** Hardware & Methods I Chair: Evan Mccarney, inMR Measure Ltd	
14:00 INV 3	*Volker Behr, University of Würzburg* Magnetic Particle Imaging – when negative contrast becomes positive	Auditorium

14:30 O9	*Martin Bruschewski, University of Rostock* CFD-grade MRV measurements of the mean velocity vector and the Reynolds stress tensor in turbulent fluid flows	
14:45 O10	*Guowen Jin, China University of Petroleum* Bound and movable fluid microdistribution characterization in porous rocks based on nuclear magnetic resonance	
15:00 O11	*Jiali He, Chongqing University* Improving the SNR of Unilateral Magnetic Resonance Sensor using LC Resonator	
15:15 O12	*Huabing Liu, Beijing Limecho Technology Co., Ltd* Emerging progress of portable NMR instrumentation in industrial application	
15:30 O13	*Dan Xiao, University of Windsor* Adaptive Pulse Sequence Design using Neural Networks	
15:45 O14	*Liang Xuan, Chongqing University* Magnetic Resonance Fingerprinting applied on a 50mT Ultra-low field MRI scanner	
16:00 – 18:30	**Posters I (odd numbers) + Coffee break**	Campus center

Aug. 29, 2023, Tuesday		
08:45	**Session 4 – 29AM:** Hardware & Methods II Chair: Martin Bruschewski, University of Rostock	
08:45 INV 4	*Pablo Prado, Livivos Inc* Single-sided NMR technology to measure biomarkers of liver disease	Auditorium
09:15 O15	*Yi-Qiao Song, Harvard University* Miniaturized Magnetic Resonance Systems and their Applications	
09:30 O16	*Jiangfeng Guo, China University of Petroleum* Two-dimensional manetic resonance data denoising via EMD-SVD	
09:45 O17	*Zijian Jia, U. of Shanghai for Science and Technology* Application of artificial intelligence on 2D NMR to identify shale components	
10:00 O18	*Yuchen Wu, Southeast University* A Comparative Study of GSP Prediction Utilizing T2 Relaxation and T1-T2 Correlated Relaxation based on Convolutional Neural Network	
10:15 O19	*Yifeng Jiang, Chiba University* Trajectory design for Spatial Encoding Magnetic Fields	
10:30 O20	*Evan Mccarney, inMR Measure Ltd* Automated eating quality measurements on lamb carcases in a processing plant using unilateral NMR	
10:45 – 11:15	**Coffee break**	Campus center
11:15	**Session 5 – 29NOON:** MR Microscopy I Chair: Daniel Clarke, Victoria University of Wellington	
11:15 INV 5	*Ye Li, Shenzhen Institute of Advanced Technology, Chinese Academy of Sciences* 5 T Human MRI: RF system and initial in-vivo imaging	Auditorium
11:45 O21	*Dan Xiao, University of Windsor* Iterative Point Spread Function Correction for Fast Spin Echo T2 Mapping	
12:00 O22	*Diana Bernin, Chalmers University of Technology* MRI methodologies to follow water ingress in pulp-based packaging materials	
12:15 O23	*Chang Ni, Shanghaitech university* DTI-measured diffusion directionality captures fluctuation in renal water reabsorption induced by water diuresis	
12:30 O24	*Maxime Yon, Lund University* Massively multidimensional diffusion MRI: from concepts to restriction sensitive and sparsely-sampled acquisition	
12:45 O25	*Alfredo Ordinola, Linköping University* Effects of geometry and relaxation on diffusion exchange measurements	
13:00 – 14:00	**Lunch/Executive Meeting**	Campus center/ TT19, 2.304
14:00	**Session 6 – 29PM:** MR Microscopy II Chair: Diana Bernin, Chalmers University of Technology	

14:00 INV 6	*Maxim Zaitsev, University Medical Center Freiburg* Towards open-source MR software and hardware with Pulseq and CoilGen	Auditorium
14:30 O26	*Yuyue Zhang, National University of Singapore* Forward and Inverse Models on the 3-D MRI-Based Electrical Properties Imaging	
14:45 O27	*Xin Mu, Shanghaitech university* Precise tracking of calf muscle fiber orientations during plantarflexion with diffusion tensor imaging	
15:00 O28	*Nian Wang, Indiana University* High-resolution Quantitative Susceptibility Mapping for Beta-amyloid Pathology	
15:15 O29	*TBC*	
15:30 Bruker	*Thomas Oerther, Sarah Mailhiot, Wei Liang Wang* Application and Helium Recovery Solutions	
16:00 – 18:30	**Posters II (even numbers) + Coffee break**	Campus center

Aug. 30, 2023, Wednesday		
08:45	**Paul Callaghan Young Investigator Competition I** Chair: Volker Behr, University of Würzburg	
08:45	*Bernhard Blümich, RWTH Aachen University* A short speech for Erwin Hahn Lecturer	Auditorium
09:00	*Petrik Galvosas, Victoria University of Wellington* Introduction to the Paul Callaghan Young Investigator Award sessions	
09:05 PCYIA 1	*Neil Robinson, The University of Western Australia* When Relaxation Goes Wrong: Unexpected Spin Behaviour in Functional Porous Media	
09:30 PCYIA 2	*Feryal Guerroudj, Chalmers University of Technology* Investigating synergistic effects between cellulose and lignin for advanced forest carbon fibers: mass transport characterization with magnetic resonance methods	
09:55 PCYIA 3	*Qingyuan Zheng, University of Cambridge* Operando MR imaging of the products of Fischer Tropsch synthesis within catalyst pores	
10:20 PCYIA 4	*Joseph Okeke, University of Birmingham* In situ and operando Spectroscopy, Imaging and Tomography of Batteries	
10:45 – 11:15	**Coffee break**	Campus center
11:15	**Paul Callaghan Young Investigator Competition II** Chair: Einar Fridjonsson, the University of Western Australia	
11:15 PCYIA 5	*Johanna Günther, University of Würzburg* Chebyshev nodes-based fingerprinting of magnetic nanoparticles	Auditorium
11:40 PCYIA 6	*Tingou Liang, Singapore U. of Technology and Design* Optimization Scheme for Single-sided Inward-outward (IO)-ring Permanent Magnet Array	
12:05 PCYIA 7	*Devin Morin, University of New Brunswick* A Ceramic Magnet for Flow Profiling and Overhauser DNP	
12:30 PCYIA 8	*Julia Lasek, AGH U. of Science and Technology* AI-BSD – deep learning based model for DTI systematic error removal	
12:55 PCYIA 9	*Junqi Yang, Chiba University* An angle selection method for rSEM	
13:20 – 14:20	**Lunch/Division Meeting**	Campus center/ TT19, 2.304
14:20 – 16:30	Free afternoon	
16:30 – 21:15	**Conference Banquet at Mount Faber** Buses leave SUTD 16:30	Mount Faber

Aug. 31, 2023, Thursday		
08:45	**Session 7 – 31AM:** Mobile & Low Field Chair: Velencia Witherspoon, National Institutes of Health	
08:45 INV 7	*Konstantin Momot, Queensland U. of Technology* Portable NMR for point-of-care clinical applications: in vivo, ex-vivo and phantoms	Auditorium
09:15 O30	*Can Liang, Changzhou Institute of Technology* Upscaling simulation of NMR surface relaxation in porous media with Lattice Boltzmann method	
09:30 O31	*William Selby, University of New Brunswick* Characterizing shear properties with portable magnetic resonance – a phase interference technique	
09:45 O32	*Siegfried Stapf, TU Ilmenau* Depth-dependent brine transport in salt-rich topsoil monitored by the NMR-MOUSE	
10:00 O33	*Lei Yang, Chongqing University* Active EMI Suppression Method for a 50mT Portable MRI Scanner in NICU	
10:15 O34	*Zhengxiu Wu, Southeast University* An Rx coil array design for lightweight ultra-low MRI prototype of the breast: proof-of-concept imaging implementation	
10:30 O35	*Bernhard Blümich, RWTH Aachen University* NMR Depth Profiling of Painted Walls: Ostia Antica	
10:45 – 11:15	**Coffee break**	Campus center
11:30	**Session 8 – 31PM:** Engineering & Materials Chair: Andrew Sederman, University of Cambridge	
11:30 INV 8	*Daniel Clarke, Victoria University of Wellington* MRI for chemical engineering: Case studies in granular flow and porous media	Auditorium
11:45 O36	*Rok Peklar, Jozef Stefan Institute* MR Imaging and Kinetic Monte Carlo Simulation of Lithium Dendrite Growth	
12:00 O37	*Emmanouela Leventaki, Chalmers U. of Technology* Evaluation of mixing efficiency in bubble reactors for carbon dioxide capture using MRI	
12:15 O38	*Patrick Vogel, University of Würzburg* Toroidal and Poloidal Vortex Rotation of Halbach Rings for Determining the Spatial Distribution of Magnetic Nanoparticles – initial results	
12:30 O39	*Razyq Nasharuddin, The U. of Western Australia* Low field NMR probe of microstructural and mechanical strength evolution of cemented paste backfill prepared using varying salinity water	
12:45 – 14:00	**Lunch**	Campus center
14:00	General Assembly Meeting	Auditorium

14:30	**Session 9 – 31PM:** Biomedical II Chair: Weng Kung Peng, Songshan Lake Materials Lab.	
14:30 INV 9	*Thu Thao LE, National Heart Centre Singapore* Clinical applications of exercise stress-induced cardiac magnetic resonance imaging	Auditorium
15:00 O40	*Velencia Witherspoon, National Institutes of Health* 3D-printed micro-anisotropic, macro-isotropic, susceptibility-matched diffusion phantoms	
15:15 O41	*Bernard Siow, The Francis Crick Institute* Towards replacing 2D Inverse Laplace Transforms with Deep Neural Networks for processing Diffusion Exchange Spectroscopy data	
15:30 O42	*Rosie Zhou, University of Posts and Telecomm.* Tract-specific Microstructural Alterations in Intermittent exotropia identified by Fiber Quantification and Effect Size Analysis	
15:45 O43	*Qiji Shi, Beijing University of Posts and Telecomm.* Cerebral White Matter Dynamic Functional Connectivity in Patients with Brain Arteriovenous Malformations (AVM) using Multi-modal MRI	

LIST OF POSTERS

NUMBER	PRESENTER	TITLE
P01	*Weichao Yan* Ocean University of China	A Study on Evaluating Shale Oil Reservoir Parameters Using 2D Nuclear Magnetic Resonance Technology
P02	*Xiao Liang* China University of Geosciences	Effect of oil-based mud (OBM) invasion to nuclear magnetic resonance (NMR) responses in tight glutenite reservoirs
P03	*Siegfried Stapf* TU Ilmenau	The ExoMOUSE – detecting liquids on solar system bodies
P04	*Emanuel Bertizzolo* The University of Western Australia	Low field NMR as an optimization tool for mechanical dewatering of anaerobic digestate
P05	*Einar Fridjonsson* The University of Western Australia	Investigation of Spacer-induced Combined Organic-Inorganic Fouling inside SWRO element via portable Earth's field NMR
P06	*Paul Teal* Victoria University of Wellington	Use and overuse of deep learning in NMR
P07	*Shin Utsuzawa* SLB	Towards Deep-Look NMR Well Logging
P08	*Nicholas Ling* The University of Western Australia	Impact of Microplastics on Fouling of Hollow Fiber Membranes: Insights from Magnetic Resonance Imaging
P09	*Nicholas Ling* The University of Western Australia	Automated Solid-Phase Extraction and NMR Analysis for Accurate Assessment of Oil and Per-/Polyfluoroalkyl Substances (PFAS) Content in Water
P10	*Maria Anikeeva* Christian-Albrechts-Universität zu Kiel	Optimizing parameters for MR studies of packed beds using ethane
P11	*Abel Worku Tessema* Ulsan National Institute of Science and Technology	Robust Resolution Improvement of UTE-MR Angiogram using 3D Super-Resolution Generative Adversarial Network
P12	*Pak Shing Kenneth Or* Lund University	Frequency optimization in multidimensional diffusion-relaxation correlation MRI on a fixed mouse brain

P13	*Wei Liu* Institute of Geology and Geophysics, Chinese Academy of Sciences	Design of Ultra-low Noise NMR Logging While Drilling
P14	*Maria Anikeeva* Christian-Albrechts-Universität zu Kiel	MR based magnetic susceptibility measurements of 3D printing materials at 3 Tesla
P15	*Devin Morin* University of New Brunswick	An Optimized Unilateral Magnet with a Large Homogeneous Region
P16	*Xi Wang* Nanyang Technological University	Deep Learning Approaches for Estimation of Specific Absorption Rate of High-Field MRI via HDMR-Generated Surrogate Models
P17	*Bernhard Blümich* RWTH Aachen University	Asymmetry in Three-Site Relaxation-Exchange NMR
P18	*Dion G. Thomas* Victoria University of Wellington	Temperature stability for diffusion measurement in single-sided NMR systems
P19	*Meghan Halse* University of York	Parahydrogen-enhanced benchtop NMR spectroscopy for analytical applications
P20	*Andy Sederman* University of Cambridge	Velocity and turbulent kinetic energy imaging of gas in packed beds at industrially relevant conditions
P21	*Tran Duc Khang & Yap Yuan Xi* NUS High School of Math. and Science	Shielding-Free Signal Noise Suppression in Portable Low-Field MRI

Educational Talks

Educational Talk 1

Parahydrogen-induced polarisation in NMR spectroscopy and imaging

Megan Halse

University of York

Abstract

*Para*hydrogen-induced polarisation (PHIP) is an signal amplification technique that uses the singlet nuclear spin isomer of molecular hydrogen, *para*hydrogen, as the source of hyperpolarisation. The pair of 1H nuclei in *para*hydrogen have a total nuclear spin of zero and so give no NMR signal. However, once their symmetry is broken in a chemical reaction they exhibit NMR signals that are amplified, often by several orders of magnitude. This enhanced signal can be detected directly or transferred to a target analyte using a reversible exchange reaction via the SABRE (Signal Amplification By Reversible Exchange) method. In this educational talk, the fundamental principles of *para*hydrogen hyperpolarisation will be described, including both the original hydrogenative PHIP approach and the non-hydrogenative SABRE method. A brief history of the use of PHIP and SABRE in imaging and spectroscopy will be presented along with perspectives for future applications.

Educational Talk 2

Opportunities offered by ultra-high field MRI

Luisa Ciobanu

NeuroSpin, CEA-Saclay, Paris-Saclay University, Gif-sur-Yvette, France

Abstract

The purpose of this presentation is to offer a fundamental overview of MRI at ultra-high magnetic fields. Ultra-high fields offer notable advantages in terms of sensitivity, contrast, and biological information, but they also present certain challenges. To overcome these challenges and achieve the anticipated benefits, enhanced gradient performance, specialized radio-frequency detectors, and improved imaging methods are required. The presentation will cover several promising applications of ultra-high field MRI, such as functional MRI, chemical exchange saturation transfer and diffusion imaging.

Educational Talk 3

Applications of (LF) Magnetic Resonance in Chemical Engineering

Michael Johns
Department of Chemical Engineering
School of Engineering
University of Western Australia

Abstract:

Despite significant potential and endeavour, the use of magnetic resonance techniques in the Chemical Engineering research community is far from ubiquitous; this is even more pertinently true in the case of chemical engineering industrial practice. This educational presentation will showcase applications of magnetic resonance imaging, diffusometry and relaxometry across the range of underpinning scientific disciplines of Chemical Engineering whilst discussing what is ultimately important to Chemical Engineers. It will then progress to provide examples of industrial applications of low field magnetic resonance and detail the additional challenges and opportunities that such application incurs.

Educational Talk 4

Outside the lab: Unique applications of NMR

Hilary T. Fabich

ABQMR

Albuquerque, NM 87106, USA

Abstract:

Magnetic resonance is most often found in a lab setting with a large, superconducting magnet providing the B0 field. However, many applications do not require such high field strengths; permanent magnets and custom electromagnets have enabled applications in atypical settings. ABQMR specializes in applications of magnetic resonance outside the lab and has developed sensors for applications such as helicopter-borne NMR to detect oil under sea-ice and images of plant roots in the agricultural field. This presentation will explore some unusual applications and the challenges that come with developing NMR sensors for use outside the lab.

Plenary Lecture

The Versatility of NMR Diffusion Measurements

W.S. Price[a], T. Stait-Gardner[a], A. Torres[a]
[a]Nanoscale Group, Western Sydney University, Penrith, NSW, Australia

Those starting their journey in NMR microscopy [1] or NMR diffusion [2] are often initially surprised by the apparent paradox that the two fields are essentially one [3]. And that being able to measure self-diffusion is not only the key to being able to probe size and molecular weight but also structural details especially those of confining geometries. Further, NMR diffusion measurements (i.e., *q*-space imaging) provide the possibility of probing structural details at length scales far below the limits of traditional imaging (i.e., *k*-space, aka MRI). Although such *q*-space "images" do not provide the traditional image akin to microscopy, they do provide perhaps more pertinent information for the relevant sample types such as porosity and average structure factors.

Whilst the development of *k*-space imaging was hindered by the availability of high-speed computing, NMR diffusion measurements, which are technically more difficult from a magnetic resonance perspective due to the need for precisely matched magnetic gradient pulses, were effectively developed and used first although not commercially available until ~the early '90s. It is perhaps too easy to gloss over the performance limitations of commercial systems and careful attention must be paid to many aspects including gradient performance, calibration, convection [4] and background gradients if accurate diffusion data is to be obtained - because only then can correct physical inferences be drawn. Also, it is important to consider deviations of the theoretical model as might occur when the relaxation time after the last pulse of each increment is less than $5 \times T_1$. This can be achieved by determining the dynamic equilibrium [5, 6] or accounting for such effects explicitly by using the Torrey–Bloch equations to obtain recurrence relations for the bulk magnetization [7].

Even the best lateral thinkers could not fail to be amazed by the versatility and astounding range of applications [8, 9] and the connections with other seemingly disparate areas of science [10]. The enormous technical and theoretical advances in NMR diffusion have opened up an extraordinary range of applications. These include separating isomers to the coupling of diffusion measurements with MRI to provide an ever-expanding array of biomarkers for diseased states, such as tumour heterogeneity [11]. Recent years have seen enormous advances in the measurement of diffusion in restricted systems and also of time dependent systems [12] including the stability of emulsions [13].

In addition to surveying some recent developments in the field, some crucial experimental aspects and ways to optimize measurements will be examined and recent applications surveyed.

References:

[1] P.T. Callaghan, Principles of nuclear magnetic resonance microscopy, 1st ed., Oxford University Press, Oxford, 1991. [2] W.S. Price, NMR studies of translational motion: Principles and applications, 1st ed., Cambridge University Press, Cambridge, 2009. [3] Gupta, Adsorption (2021). [4] MacDonald, Angewandte Chemie (Int. Ed.) (2019). [5] Stait-Gardner, Chem.Phys.Lett. (2008). [6] Zubkov, J. Chem. Phys. (2015). [7] Lee, J. Chem. Phys. (2021). [8] S.A. Willis, T. Stait-Gardner, A.M. Torres, G. Zheng, A. Gupta, W.S. Price, Expanding NMR versatility, in: A. Bunde, J. Caro, C. Chmelik, J. Kärger, G. Vogl (Eds.) Diffusive spreading in nature, technology and society, Springer International Publishing, Cham, 2023, pp. 247-277. [9] Stait-Gardner, A. Gupta, A.M. Torres, S.A. Willis, Z. Xiao, G. Zheng, M. Ishikawa, W.S. Price, Magnetic resonance studies of adaptation to freezing and injury in plants, in: W.S. Price (Ed.) Annual reports on NMR spectroscopy, Academic Press, London, 2023. [10] Ghadirian, J. Chem. Phys. (2013). [11] Pham, Sci. Rep. (2019). [12] Fillbrook, J. Am. Chem. Soc. (2021). [13] Kanai, Langmuir (2023).

Session 1 – 28AM

Biomedical I

Chair: Bernard Siow, the Francis Crick Institute

Invited Talk 1

3D MRI With CT-Like Bone Contrast – How I Do It

Le Roy CHONG
Department Of Radiology, Changi General Hospital, Singapore

Introduction: CT is the gold standard imaging modality for the assessment of 3D bony morphology, but incurs the cost of ionizing radiation exposure. MRI provides excellent assessment of soft tissues and medullary bone marrow without ionizing radiation, but is limited in depicting cortical (and subchondral) bone due to its very short T2 relaxation times, low proton density and organized structure. Improving the ability of 3D MRI in providing high-resolution images of cortical bone with CT-like bone contrast has been an area of recent research.

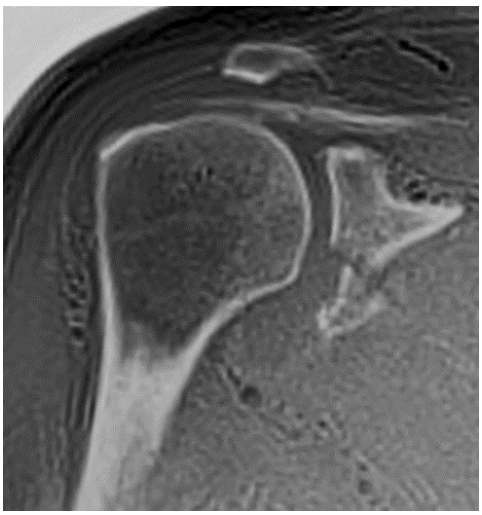

Fig. 1: Coronal 3D-Bone shoulder MRI in a patient with recurrent shoulder dislocations shows a large displaced bony Bankart fragment from the anterior glenoid rim.

3D MRI with CT-like bone contrast can deliver information on cortical bone morphology with similar diagnostic performance to CT, and may provide an alternative to CT for certain clinical indications to facilitate complete evaluation of cortical bony morphological, soft tissue structures and bony marrow with a single MRI examination. This potentially simplifies imaging evaluation, obviates radiation exposure from additional CT studies and lowers patient costs.

This talk discusses the clinical implementation, advantages and disadvantages of an optimized stack-of-stars 3D gradient recalled echo pulse sequence (3D-Bone) on commercially available MRI scanners for rendering 3D MRI with CT-like bone contrast in our institutional practice, as well as providing an illustrative review of the utility of 3D-Bone in the clinical assessment of common musculoskeletal conditions.

References: [1] Chong, Eur. J Radiol (2021).

Anatomy-guided and point-cloud-based deep learning framework for superficial white matter tractography parcellation

Di Zhang[1], *Fangrong Zong*[1,*]
[1]School of Artificial Intelligence, Beijing University of Posts and Telecommunications, Beijing, China; *Corresponding author

Introduction: Diffusion magnetic resonance imaging (dMRI) tractography is an advanced imaging post-processing technique that enables three-dimensional reconstruction of white matters [1]. However, it is challenging when using dMRI to parcellate superficial white matter (SWM), which are short-range association u-fibers connecting adjacent and nearby gyri [2]. Combining both white matter fiber geometry and gray matter anatomical information may aid the SWM segmentation. Herein, a new anatomy-guided and point-cloud-based deep learning framework is proposed to classify SWM into different small clusters automatically.

Methods: A new framework with anatomy-guided and point-cloud-based deep learning method is proposed to parcellate the SWM into 198 clusters from coarse to fine (Fig. 1). In brief, we calculate the number of points on each subject's parcellation atlas at an individual level, then add them and cluster into 8 large clusters from the group level. Finally, we fuse these features with the PointNet encoder and divide into 198 small clusters through a decoder. Additionally, we applied the proprsed method to Alzheimer's disease (AD) and mild cognitive impairment (MCI) disease dataset to parcellate SWM fibers, then calculated fractional anisotropy (FA), axial diffusivity (AxD) , radial diffusivity (RD) and mean diffusivity (MD) of each fiber bundles.

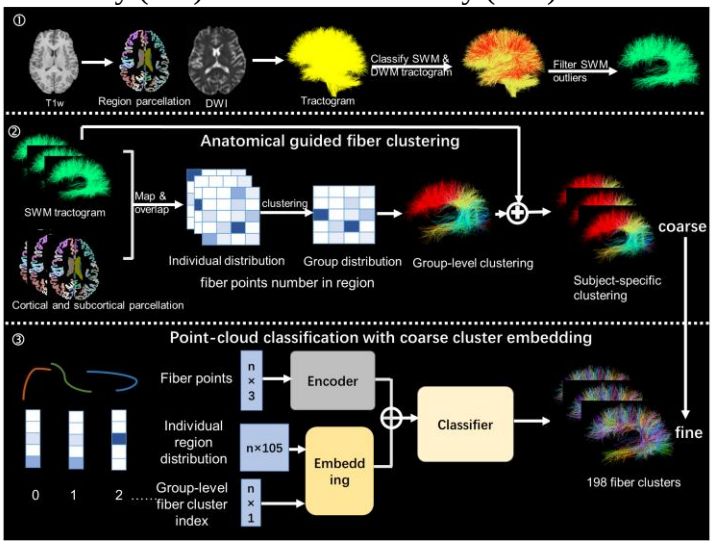

Fig.1 SWM tractography parcellation framework.

Table.1 Comparison with different methods.

Network	SWM	
	accuracy(SD)	F1-score(SD)
DeepWMA	93.097(4.583)	93.056(4.735)
SupWMA	95.497(3.807)	95.486(3.800)
Proposed	97.968(1.302)	97.951(1.307)

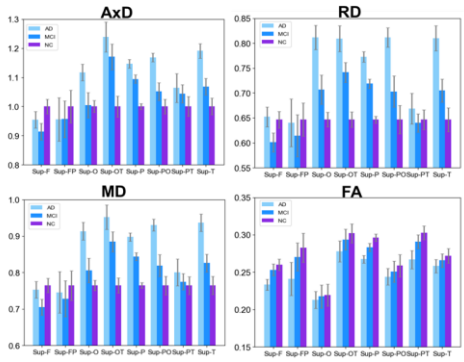

Fig.2 Comparison of AxD, RD, MD and FA.

Results:
The SWM tractography parcellation framework obtains 97.968% accuracy averagely. The comparison with other current methods is shown in Table.1. The 8 coarse clusters' metrics of AD, MCI and healthy adults are shown in Fig. 2 here for simplicity. AxD, RD and MD values are generally higher in patients than healthy subjects while FA values are reversed.

Conclusion:
We propose an anatomy-guided and point-cloud-based deep learning framework for superficial white matter tractography parcellation, which obtains high accuracy on training data. The segmented SWM fibers could be used to diagnose AD and MCI in clinical applications.

References: [1] Basser, Magn. Reson. Med. (2000). [2] Guevara, NeuroImage. (2020).
Acknowledgement: This work was supported by the National Natural Science Foundation of China (No. 61901465).

Attention-based q-space Deep Learning: Fast Diffusion Magnetic Resonance Imaging with Varied Sampling Strategies

Zaimin Zhu [a], *Yong Liu* [a], *Fangrong Zong* [a]
[a]School of Artificial Intelligence, Beijing University of Posts and Telecommunications, Beijing, China.

Introduction: Diffusion MRI (dMRI) provides abundant tissue microstructure information with large number of scans that carry high time costs [1,2]. A q-DL model was proposed to accelerate dMRI by using deep learning (DL) methods [3]. However, there is currently no effective DL model proposed for highly undersampled datasets with varying diffusion gradient sampling strategies. To mitigate this problem, we propose a new model called attention-based q-space deep learning (aqDL). By introducing the attention mechanism, we successfully achieve diffusion parameters reconstruction on variable undersampled diffusion gradient directions.

Methods: To perceive variations in the sampling strategy, the model take the diffusion gradient value and directions as the inputs. The architecture of the aqDL model consists of an embedding block, a transformer block, and a multilayer perceptron (MLP) serving as the decoder (Figure 1).

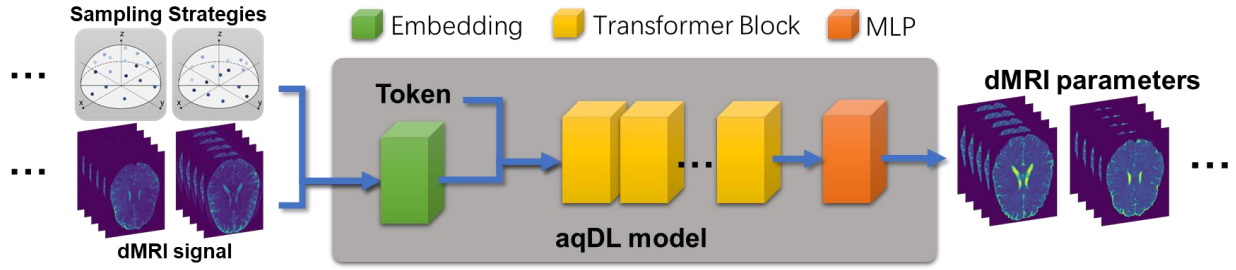

Fig. 1. The main architecture of the aqDL model

The data used to train and test the models is derived from the 7T dataset of the Human Connectome Project (HCP). This dataset comprises 146 subjects, with each subject's data including a total of 143 diffusion weighted (DW) images. From the fully sampled HCP datasets, we simulated two types of undersampled datasets: one with a fixed sampling strategy and the other with a random sampling strategy. Each voxel in both datasets contained 17 DW images. In the fixed sampling strategy, all voxels adopt a set of fixed and uniform gradient directions. In contrast, in the random sampling strategy dataset, the gradient direction of each voxel was randomly assigned.

Results and discussion: Table I presents the peak signal-to-noise ratio (PSNR) and structural similarity (SSIM) of the diffusion parameter maps reconstructed by the two models. In the dataset with a fixed sampling strategy, the aqDL model demonstrates significant improvements in PSNR and SSIM for MD, AD, RD, FA, and KFA when compared to aDL. Since qDL is not applicable to randomly sampled datasets, we exclusively evaluated the performance of aqDL on this dataset. The results reveal that variations in the sampling strategy do not significantly diminish the reconstruction accuracy of aqDL and in fact improve accuracies of certain diffusion parameters.

Table I. PSNR and SSIM of Reconstructed Result of qDL and aqDL models

		MD	AD	RD	FA	MK	AK	RK	KFA
PSNR	qDL-fixed	21.95	19.85	22.11	16.83	17.94	18.71	16.08	16.07
	aqDL-fixed	24.54	22.05	24.67	18.50	17.98	18.81	16.35	17.09
	aqDL-random	24.52	21.68	24.78	17.80	18.00	18.94	16.11	17.18
SSIM	qDL-fixed	0.8417	0.7957	0.8418	0.5986	0.5861	0.6404	0.4782	0.5644
	aqDL-fixed	0.9330	0.9075	0.9297	0.7620	0.6550	0.6957	0.5930	0.6927
	aqDL-random	0.9310	0.8979	0.9298	0.7145	0.6514	0.7022	0.5595	0.6913

Conclusion: This paper presents a new dMRI parameter reconstruction model that could accept undersampled data with varying sampling strategies and achieves more accurate reconstructed results compared to existing models.

References:[1] Jensen, J. H., NMR Biomed(2010);[2] Raab, Peter, Radiology(2010);[3] Golkov, V., Trans Med Imaging (2016).

Acknowledgement: This work was supported by the National Natural Science Foundation of China (No. 61901465).

NMR-based traits: The Next Generation of Precision Medicine

Weng Kung PENG, *Xiaomin Lin, Peishan Deng, Shijin Yuan*
Songshan Lake Materials Laboratory, Dongguan, China

Introduction

Genetic contribution to different diseases were found to be varies, with non-genetic factors (e.g., environmental hazards) having much greater attributable risks, producing a large phenotypic variation. As a result, the current one-size-fits-all medical practices are sub-optimal, leaving much room for improvement. Our research focuses on addressing the challenges by introducing a novel class of multiparametric time-domain NMR-based 'molecular signature' of biological fluids (e.g., blood) with respect to its´ various pathophysiological states and deep phenotyping of food science (e.g., edible oils).

Methods

In this work, we demonstrate that using the technological innovations (e.g., (low-cost) traditional imaging techniques, spectroscopy-based point-of-care) and advanced data analysis (e.g., manifold-learning) to access the internal and external phenotypes of a single peanut pod. We studied over 6500 complex geometries of peanut pods (*A. hypogaea L*) cultivated in various regions in China and demonstrated high-throughput multi-omics platform (e.g., time-domain NMR, UV-Visible analysis) and biophysical traits (e.g., complex geometry). We argued that such platform integrating the internal-external phenotype space, will be the key solutions to speed up the understanding of genetic doldrum (e.g., complicated molecular pathway).

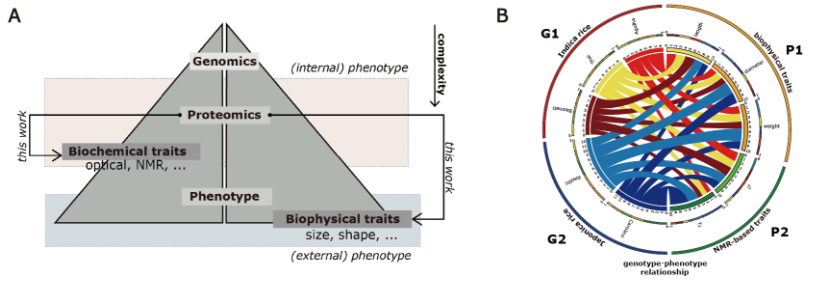

Fig. 1: (A) The pyramid of biological scales as opposed to its complexity. The correlation between biochemical traits (e.g., time-domain NMR, optical) and biophysical traits (e.g., length, diameter) were established in this work. (B) The complex network of Genotypic-Phenotypic (GP) relationship modulated by environmental factors producing unique and specific complex geometry of large biodiversity of phenotype.

Results and discussion

In this initiative, we propose an entire new framework dealing with the complexity of genotype-phenotype correlogram as a result of complicated with its' environmental (GE interactions), a complex mixing between sheer numbers of environmental cocktails, and this inherent complexity of (probabilistic) genetics. The process of digitization of information allows reconstruction (or reconstitute) them into their unique and yet specific 'molecular signature' by exploiting the advent of technological innovations (e.g., multidimensional NMR, high-throughput UV-Vis analysis, optical microscopy) and the advent of big-data analysis (e.g., t-SNE, UMAP).

Conclusion

Reversing genetic research (e.g., multiparametric high-throughput phenotyping based on NMR in non-destructive manner) is one of the keys to speed up the understanding of genetic research in agricultural and human health/diseases.

References

[1] Peng, npj Sci. Food. (2022). [2] Peng, npj Aging Mech. Dis. (2020). [3] Peng, Commun. Biol. (2020). [4] Peng, Nat. Med. (2014). [5] Peng, Rev. Sci. (2012).

Session 2 – 28NOON

Diffusion in biology & medical applications

Chair: Siegfried Stapf, TU Ilmenau

The First Study of Biomaterials by Nuclear Magnetic Resonance

Y. Xia
Oakland University, Rochester, Michigan, USA

Introduction

To find out who actually achieved a *first* in science and technology is not an easy task; sometimes, the conclusion can be controversial. Even more difficult is, many years after the events, ascertaining the background and journey that led those pioneers to carry out those first studies. The topic of this historical account is the study of biomaterials by nuclear magnetic resonance, by Erik Odeblad and Gunnar Lindström, who published a paper in 1955 in the journal *Acta Radiologica*, titled "Some preliminary observations on the proton magnetic resonance in biologic samples" [1].

Methods

The 1955 Odeblad and Lindström paper came to be known to the author in an unrelated communication in 2015. Internet research unearthed several pieces of related information, which were interesting but did not provide a full story. A few months later, Peter Stilbs (Royal Institute of Technology, Stockholm, Sweden) searched the Internet in Swedish, which unearthed several additional pieces of useful information. Gradually, the story of the first cartilage study by NMR became complete and credible [2]. A moral to be learnt from this Internet digging experience is that the Internet searches in English would most likely just discover information in English; for information of foreign origins, you must search in the native language.

Results and discussion

Studies of a number of biological tissues were reported in the 1955 Odeblad and Lindström paper, including liver, muscle, fat, corpus vitreum, fibrous tissue, tendon, and cartilage. One reached a conclusion by comparing the signal of pure-water with the signal of a non-water sample. A number of differences can be found between the water signal and the tissue signal. For example, the authors wrote that "The proton signals in yeast were lower and somewhat broader than in pure water." The authors stated "In cartilage and fibrous tissue, in which the proton signals probably arise from highly viscous water with short spin-lattice relaxation time, the signals were also larger than would correspond to the water content." The authors speculated that the signal differences between water and biological tissues could be attributed to the absorption and organization of the water molecules to the proteins in the tissue, which was remarkably accurate.

Conclusion

It is quite certain that Odeblad and Lindström published the first biomedical study involving the use of NMR. In their 1955 paper, cartilage and a number of other biological tissues were examined for the first time using nuclear magnetic resonance.

Acknowledgement: An NIH R01 grant (AR 069047).

References

[1] Odeblad E, Lindström G. "Some preliminary observations on the proton magnetic resonance in biologic samples." Acta Radiol 1955; 43(6): 469-76.
[2] Xia Y. and Stilbs P. "The First Study of Cartilage by Magnetic Resonance: A Historical Account." Cartilage 2016; **7**(4): 293-297.

The correlation between healthy aging and DTI metrics of the brain regions

Z. Schneider[1], *A. Słowik*[2], *A. Krzyżak*[1]
[1] AGH University of Science and Technology, 30-059 Krakow, Poland
[2] Neurology Clinical Department, University Hospital, 30-688 Krakow, Poland

Introduction: Diffusion tensor imaging (DTI) can be described as a marker of the integrity and organisation of brain tissue and is therefore useful for the analysis of brain structure changes and degeneration with age. In the literature on this topic, the main focus has been on the relationship between age and diffusion parameters of white matter pathways, and such correlations have been reported [1]. However, other regions of the brain are not sufficiently examined in this respect. In this study, we carried out a correlation analysis between age and 25 diffusion parameters in multiple brain structures. In addition, the analysis was performed on a DT calculated using the b-matrices provided by the vendor and one that had been calculated using b-matrix spatial distribution (BSD), a calibration method that reduces systematic errors in MRI diffusion images [2,3].

Methods:

Participants: Data of 62 healthy subjects (44 females, 18 males) – aged 21 to 50 years (mean age ± standard deviation: 34.7 ± 7.8) were analyzed in the study.

MRI acquisition: All study participants underwent brain MRI using a 3T Siemens Magnetom scanner in the University Hospital in Krakow, Poland. The imaging protocol included a T1-weighted MPRAGE sequence and a spin-echo echo-planar imaging (EPI) sequence with diffusion gradients applied in 20 directions; *b* factor of 0 s/mm^2, 1000 s/mm^2 and 2000 s/mm^2; repetition time, 3900 ms; echo time, 88 ms; field of view, 191 x 191 mm^2 ; voxel size, 2.5 x 2.5 x 2.5 mm^2; number of slices, 50.

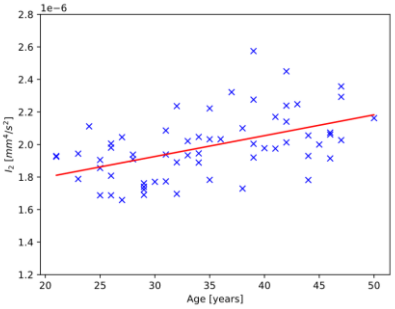

Fig. 1: The relationship between age and RH posterior cingulate cortex I_2 (r = 0.5, p < 0.001).

Data processing: For regional diffusion analysis, we used Fast Surfer (FS) software [4] to generate segmentation of 95 anatomical structures of the brain. The FS classes were grouped into 7 larger regions of interest (ROI) and such 2 sets of masks (95 and 7 ROIs) were used for further analysis. DTI was calculated using the original b-matrices (STD-DTI) and those corrected by applying BSD (BSD-DTI). The study included 25 DTI metrics such as mean diffusivity (MD), axial (AD) and radial diffusivity (RD), fractional anisotropy (FA), DT eigenvalues, ultimate anisotropy indices, diffusion tensor elements, rotational invariants (I) and lattice index [5]. The correlation analysis was performed by calculating the Pearson coefficient r using Python 3.9.13.

Results and discussion: A statistically significant correlation with age was found for all analyzed diffusion parameters in at least one ROI. For BSD-DTI 95-ROI analysis, we found 140 pairs of the age-ROI diffusion parameter with an absolute value of r greater than 0.3, and 57 pairs with $|r| > 0.4$. For STD-DTI the numbers are 130 and 53. Correlations with the highest number of metrics were found in some cortical areas such as the right hemisphere (RH) cuneus ($|r| > 0.2$ for 23 metrics) and lingual gyrus ($|r| > 0.2$ for 15 metrics). The strongest correlation was for the RH posterior cingulate cortex I_2 (r = 0.5, p < 0.001) and I_3 (r = 0.5, p < 0.001). Significant correlations were also observed for the 7-ROI analysis, but the strength of these relationships was slightly lower (max $|r|$ = 0.37).

Conclusion: The relationships that were found may contribute to a better understanding of age-related changes of brain tissue structure and neurodegeneration. Moreover, we observed the influence of systematic errors on the DTI quantitative parameters.

Acknowledgements: The work was financed by Medical Research Agency contract no: 2020/ABM/01/00006-00.

References: [1] Cox S. et al. Nat. Commun. (2016). [2] Krzyżak A. et al., Magn. Reson. Imag. (2015). [3] Borkowski K. et al., J. Magn. Reson. (2018). [4] Henschel L. et al. NeuroImage (2020). [5] Kingsley P. Concepts in Magnetic Resonance Part A (2006).

Double-rotation gradient waveforms and nonparametric distributions of frequency-dependent diffusion tensors

Omar Narvaez[1], Maxime Yon[1,2], Hong Jiang[2], Alejandra Sierra[1], D. Topgaard[2]
[1]A.I. Virtanen Institute for Molecular Sciences, University of Eastern Finland, Kuopio, Finland ,
[2]Department of Chemistry, Lund University, Lund, Sweden

MRI is the method of choice for noninvasive studies of micrometer-scale structures in biological tissues via their effects on the time/frequency-dependent ("restricted) and anisotropic self-diffusion of water. Traditional diffusion MRI relies on pulsed magnetic field gradients to encode the signal with information about translational motion in the direction of the gradient, which convolves fundamentally different aspects—such as bulk diffusivity, restriction, anisotropy, and flow—into a single effective observable lacking specificity to distinguish between biologically plausible microstructural scenarios [1]. To overcome this limitation, we introduce a formal analogy between measuring rotational correlation functions and interaction tensor anisotropies in NMR spectroscopy and investigating translational motion in MRI [2], which we utilize to convert data acquisition and analysis strategies from NMR of rotational dynamics in macromolecules [3] to MRI of diffusion in biological tissues, yielding model-independent quantitative metrics reporting on relevant microstructural properties with unprecedented specificity. In particular, we use "double-rotation" gradient waveforms [4] to explore both the frequency and anisotropy dimensions of the tensor-valued encoding spectrum (see Fig. 1) in addition to the *b*-value and direction of conventional diffusion tensor imaging, Monte Carlo data inversion [5] to convert the detected signal into nonparametric distributions of frequency-dependent diffusion tensors, and insights from "dynamics detectors" [6] to convert the noise-sensitive primary distributions into more robust projections and quantitative metrics reporting on diffusivity, anisotropy, orientation, and restriction. The approach is demonstrated on liquid crystals, yeast cells, and *ex vivo* rat brain as shown in Fig. 1.

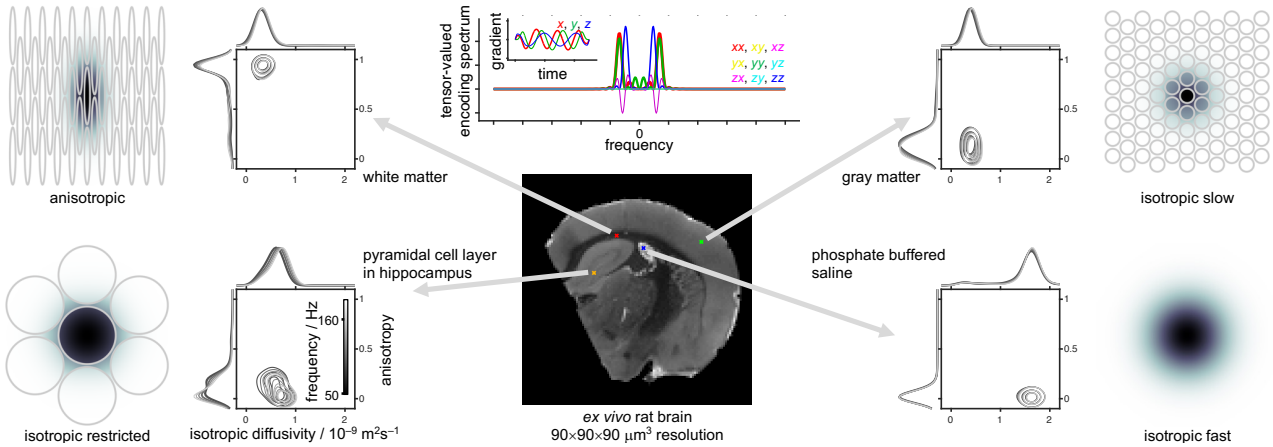

Fig. 1. Diffusion encoding by double-rotation gradient waveform (top center) and frequency-dependent diffusion tensor distributions for selected voxels of an *ex vivo* rat brain. The multidimensional distributions are visualized as projections onto the 2D plane of isotropic diffusivity and normalized anisotropy for a series of frequencies (gray scale of contour lines), where restriction results in a shift of the distribution with frequency (bottom left). For each voxel, the underlying tissue structure is shown schematically with gray lines representing partially permeable cell membranes and "ink stains" illustrating water diffusion during the 10 ms timescale of diffusion encoding.

References: [1] Topgaard, *J. Magn. Reson. 306*, 150 (2019). doi: 10.1016/j.jmr.2019.07.024; [2] Narvaez, *arXiv:2111.07827* (2021). doi: 10.48550/arXiv.2111.07827; [3] Lipari, *J. Am. Chem. Soc. 104*, 4546 (1982). doi: 10.1021/ja00381a009; [4] Jiang, *Magn. Reson. 4*, 73 (2023). doi: 10.5194/mr-4-73-2023; [5] Prange, *J. Magn. Reson. 196*, 54 (2009). doi: 10.1016/j.jmr.2008.10.008 [6] Smith, *Angew. Chem. Int. Ed. Engl. 56*, 13590 (2017). doi: 10.1002/anie.201707316.

Fast Diffusion Exchange Spectroscopic Imaging (fDExSI) MRI - fast quantification diffusion exchange for cell permeability imaging.

Arabella Cox[1], Bernard Siow[1,2]
[1] UCL Centre for Advanced Biomedical Imaging, U.K., [2] The Francis Crick Institute, U.K.

Introduction: Here, we develop a fast technique to quantify diffusion exchange and validate it *in silico*. Quantifying diffusion exchange is of great importance within both clinic and biomedical research for example, abnormal cell membrane permeability in cancers, infectious diseases, and neurodegenerative disorders [1]. The spectroscopic DExSy method [2] has long scan durations as double diffusion encoding is used (n^2 measurements). Recently, faster methods have been utilised for biomedical imaging applications [3-5]. The fDExSI approach, described here, measures only the points at which the diffusion weightings are the same for both encoding blocks (b_1=b_2), meaning only n measurements are needed. The 1D fDExSI spectra should produce 3 peaks at $2D_a$, $2D_b$, and (D_a + D_b) in a two-compartment system (see Table 1).

Method: DExSy and fDExSI signals were simulated using MATLAB using the equations in [2] for a two-compartment model. The simulated signals were processed using ILTs [6]. Diffusion Exchange Index (DEI) [7] was calculated for fDExSI (DEI_{fast}), using $DEI = \frac{2P_2}{P_1+P_3}$ and compared to the ground truth DEI calculated from the forward model (DEI_{gt}). We also compared DEI calculated for DEXSY using (DEI_{full}).

Results: We see the predicted three peaks in the fDExSI spectra (e.g. Figure 1), and, in the presence of noise, DEI_{fast} has a 1-1 good correlation with DEI_{gt}, comparable to DEI_{full} (e.g. Figure 2). At low n, peaks may merge, however the DEI can still be calculated if volume fractions are known, e.g. by preforming another n measurements with the second set of diffusion encoding gradients set to zero.

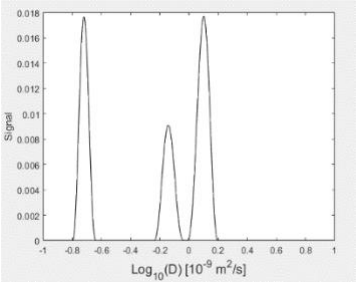

*Figure 1- Representative 1D fDExSI spectrum, n=256. Noise free. DEI = 0.5, $V_f = 0.5$ **

Discussion and Conclusion: We demonstrate that quantification of DEI using fDExSI is feasible and retains a high level of accuracy at SNR=15. We show that DEI can still be calculated even if some peaks merge. fDExSI still requires the ILTs, however, 1D-ILTs are more tractable and faster than 2D ILTs, reducing time needed for data analysis over the 10^5-10^6 voxels in an imaging scan. Future work includes replacing ILTs with machine learning techniques, for which we have promising preliminary results for 2D DExSy scans (presented elsewhere). fDExSI can easily be extended to more than two compartments and we will be investigating this in the future, as well as exploring the viability over a wider range of parameters and signal models.

The fDExSI technique could reduce the need for invasive tissue biopsies, enable earlier diagnosis and better monitoring of disease progression through quantitative cell membrane permeability imaging.

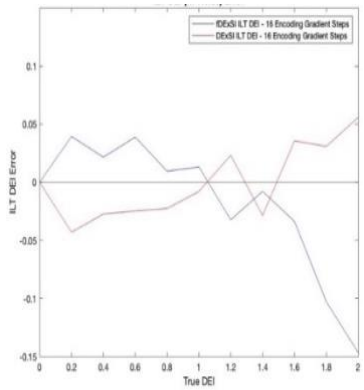

Figure 2 – Bland-Altman plot of DEI_{fast} (blue, n=16) and DEI_{full} (red, n=256) vs DEI_{gt}. SNR = 15.*

**Range of parameters used in testing: $\delta = 1 - 10ms$, $\Delta = 10 - 100ms$, $q = 0 - 10^6 m^{-1}$, $V_f = 0 - 1$, $DEI = 0 - 2$, $D_{a,b} = 10^{-9} - 10^{-12} m^2/s$*

Compartment		Signal		Total Signal
PGSE 1	PGSE 2	PGSE 1	PGSE 2	
A	A	$S_{1,a} \sim e^{-bD_a}$	$S_{2,a} \sim e^{-bD_a}$	$S_{a,a} \sim e^{-bD_a} e^{-bD_a} = e^{-2bD_a}$
A	B	$S_{1,a} \sim e^{-bD_a}$	$S_{2,b} \sim e^{-bD_b}$	$S_{a,b} \sim e^{-bD_a} e^{-bD_b} = e^{-b(D_a+D_b)}$
B	A	$S_{1,b} \sim e^{-bD_b}$	$S_{2,a} \sim e^{-bD_a}$	$S_{b,a} \sim e^{-bD_b} e^{-bD_a} = e^{-b(D_b+D_a)}$
B	B	$S_{1,b} \sim e^{-bD_b}$	$S_{2,b} \sim e^{-bD_b}$	$S_{b,b} \sim e^{-bD_b} e^{-bD_b} = e^{-2bD_b}$

Table 1: Signal equations for individual PGSEs and total signal

References: **[1]** Azad AK et al, Front Genet, 12:654865, 2021. **[2]** Callaghan PT and Furo I, J Chem Phys, 120(8):4032-8, 2004. **[3]** Nilsson M et al, Magn Reson Med 69(6):1572-80, 2013. **[4]** Benjamini D and Basser P, J Magn Reson, 271:40-45, 2016. **[5]** Williamson NH et al, J Magn Reson, 317:106782, 2020 **[6]** Godefroy S, Ryland B, and Callaghan PT, 2D Laplace Inversion software, Victoria University of Wellington, NZ. **[7]** Breen-Norris J et al, Magn Reson Med,84(3): 1543-1551,2020.

Full Diffusion Tensor Distribution to Characterize Tissue Microstructure and Types in Brain Tumors

Y. Song[1,2], *I. Ly*[2], *Q. Fan*[2,3], *A. Nummenmaa*[2], *M. Martinez-Lage*[2], *W.T. Curry*[2], *J. Dietrich*[2], *D. A. Forst*[2], *B. R. Rosen*[2], *S. Y. Huang*[2] *and E. R. Gerstner*[2]

[1]Harvard University, Cambridge, MA, USA, [2]Massachusetts General Hospital, Charlestown, MA, USA, [3]Tianjin University, Tianjin, China

Introduction: Diffusion MRI is widely used for the clinical examination of a variety of diseases of the nervous system. However, clinical MRI scanners are mostly capable of only low magnetic field gradients and are thus limited to obtaining average diffusion properties. The availability of high gradient systems such as the Connectome MRI scanner with gradient strengths up to 300 mT/m enables quantification of a broader range of diffusion coefficients which is important to characterize tissue microstructure and heterogeneity. This paper outlines a framework for obtaining a Full Diffusion Tensor Distribution (FDTD) with a wide variety of diffusion tensor structures (Fig. 1) and without prior assumption of the form of the distribution [1].

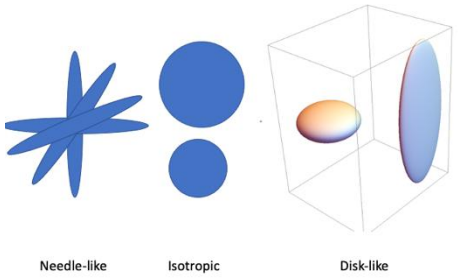

Fig. 1: Examples of the wide range of diffusion tensors included in FDTD.

Methods: To obtain a comprehensive description of tissues, we expand the definition of diffusion tensor (**D**) components to include those with and without axial symmetry and with a wide range of diffusion coefficients. The signal from a voxel includes the contribution from all **D**s: $\boldsymbol{D}$). Here **b** is the tensor form of the diffusion weighting factor and f(**D**) is the FDTD. This equation was solved to obtain f(**D**) using the Fast Laplace Inversion algorithm [2]. The resulting f(**D**) is further analyzed by the K-means method to obtain tissue classification.

Results: We demonstrated our FDTD method by numerical simulation, and dMRI data from healthy subjects and brain tumor patients. A wide range of diffusion tensor symmetry has been observed in all subjects indicating their importance in all diffusion interpretation models. Furthermore, the FDTD analysis showed significantly different FDTDs along the tumor periphery from the center region suggesting that this feature can be a new biomarker for tumor heterogeneity. Additional experimental results and analysis will be presented at the conference.

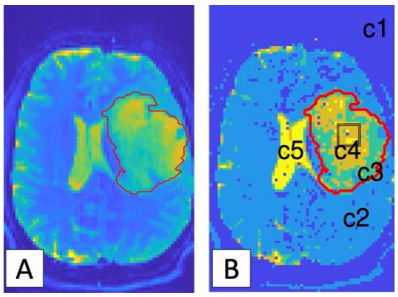

Fig. 2: (A) MRI image without diffusion weighting. (B) Classification of normal and tumor tissues (c1-c5) using the FDTD-K-means method. The red lines mark the tumor area in both images.

Conclusion: This work suggests the importance of diffusion tensors beyond those commonly considered in many diffusion models of the brain to understand the tissue microstructure. Our method of combining high-gradient dMRI and the data-centric analysis is a potential non-biased biomarker for tumor heterogeneity for clinical cancer care.

References:

[1] Y. Song, et al. Measurement of Full Diffusion Tensor Distribution Using High-Gradient Diffusion MRI and Applications in Diffuse Gliomas. Frontiers in Physics 10, 813475 (2022).

[2]. Y. Song, *et al.* T1–T2 Correlation Spectra Obtained Using a Fast Two-Dimensional Laplace Inversion. *J Magn Reson* **154**, 261–268 (2002).

Rapid monitoring of cleaning efficiency of fouled hollow fiber membrane module via non-invasive NMR diffraction technique.

B. Yan[1], S.J. Vogt[1], B. Blankert[2], J. Vrouwenvelder[2,3], M.L. Johns[1], E.O. Fridjonsson[1]
[1]University of Western Australia, Crawley, Australia, [2]KAUST, Thuwal, Saudi Arabia, [3]Delft University, Delft, The Netherlands.

Early fouling warning is important for the economical operation of membrane separation systems. In parallel multi-channel flow systems, flow re-distribution between channels due to fouling is often associated with maloperation. In the current research we use low magnetic field NMR to monitor multi-fiber hollow fiber membrane modules undergoing a fouling-cleaning cycle and show that rapid detection of fouling is possible by detecting the loss of signal coherence [1] associated with flow re-distribution within the 401 hollow fiber membrane module. This effect is demonstrated to be both reproducible, and reversible via membrane cleaning. The results demonstrate a strong correlation between the coherence signal magnitude and the number of fibers fouled. This may be used in practice for sensitivity early warning, and to monitor the efficiency of cleaning. This approach may also be particularly useful in the case of detecting residual fouling after cleaning, evidenced in this research (see Fig 1) by significant flow re-distribution between the before fouling and after cleaning signal coherence [2, 3].

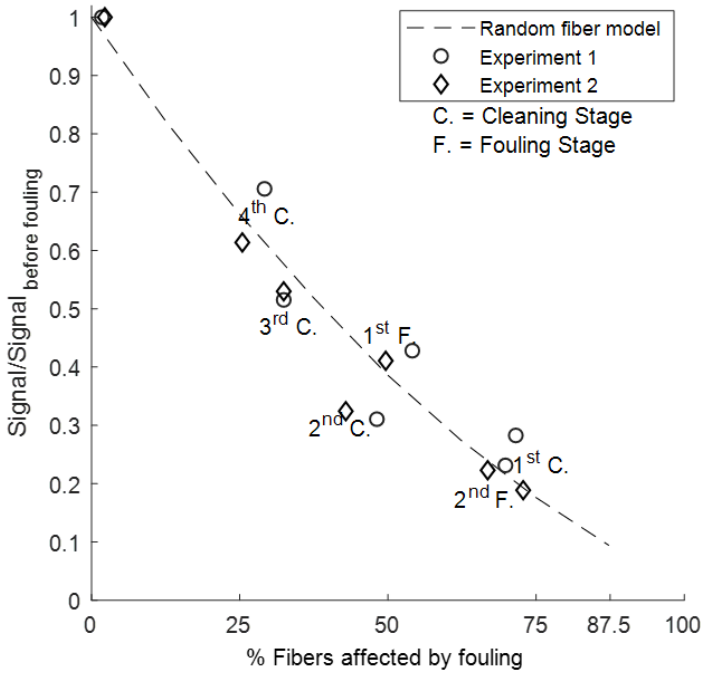

Fig. 1. Shows the correlation between the signal obtained for the $|\boldsymbol{S}(\boldsymbol{k})|^2$ coherence peak from the centre-line of **k**-space plotted against the % of fibers with greater than 5% reduction in volumetric flow which is fibers assessed from velocity images (see [3] for reference). For comparison the same correlation for the Monte Carlo model (n = 50) is shown for random fiber fouling (black dash line). It can be seen that there is a strong correlation between % fibers affected by fouling and the magnitude of the coherence peak.

References: [1] Barrall et al. Science (1992). [2] Yan et al. Journal of Membrane Science (2021). [3] Yan et al. Water Research (2023).

Session 3 – 28NOON

Hardware & Methods I

Chair: Evan Mccarney, inMR Measure Ltd

Magnetic Particle Imaging – when negative contrast becomes positive

Volker C. Behr[a]
[a]Experimental Physics 5, University of Würzburg, Würzburg, Germany

Introduction: Magnetic Particle Imaging (MPI) is a promising imaging technique. Firstly introduced in 2005 [1] it uses magnetic nanoparticles (MNPs) as tracers detecting their spatial distribution as well as relaxation properties of their inherent magnetisation. While the former enables imaging the latter grants access to functional parameters of the MNPs' environment. This makes MPI a very promising method for biomedical imaging with preclinical application already shown [2,3], and the transition to human application in progress [4,5].

Methods: The fundamental principle of signal generation is the non-linear response of MNPs to time varying magnetic fields. Fig.1 (left) shows the example of a sinusoidally alternating magnetic field applied to an ensemble of MNPs that will in turn generate a signal response containing higher harmonics to this basic frequency. The amplitudes of the higher harmonics are characteristic for the used MNPs as well as its environmental conditions. Fig.1 (right) shows the same experiment in the presence of an additional offset field keeping the MNPs saturated and therefore unable to generate signal. In this way, a spatially dependent offset field enables localisation by generating a field free region and moving it over the sample, restricting signal generation to this small region.

To make MNPs biocompatible they are coated (e.g., by dextrane or citrate) and can be further functionalised by adding groups to the coating that will exhibit specific bindings (e.g., to antibodies) giving access to diagnostic imaging by localizing the bound MNPs.

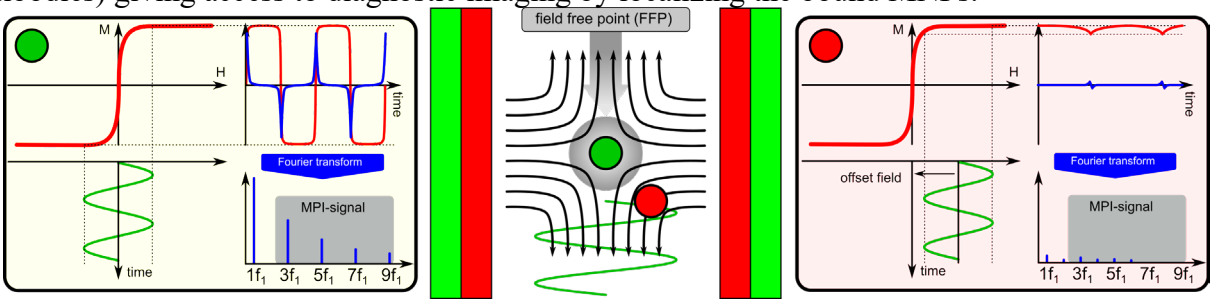

Fig. 1: Fundamental principle of MPI. *Left*: Signal without offset field, *center*: exemplary magnet configuration generating a field free point, *right*: signal with offset field.

Results and discussion: A variety of MPI scanners have been implemented employing differently shaped field free regions (mostly points or lines) for spatial encoding and ranging from large stationary to small handheld and devices [6]. Even multimodal scanners have been presented [7,8]. With these scanners a wide range of applications could be evaluated: with pre-clinical tests visualizing first-pass blood flow in the murine heart [3] or agglomeration of particles in specific binding sites [9] to the translation to human application showcasing a head scanner to be used in stroke units [4] or a leg scanner for use in interventions like a percutaneous transluminal angioplasty [5]. An approach based primarily on the spectroscopic information uses MPI for determining the presence of an analyte (e.g., SARS-CoV2) with highest sensitivity and specificity comparable to the gold-standard of ELISA tests but with results available within seconds [10]. Besides biomedical applications other fields are explored like iron-distribution in rock [11].

Conclusion: Magnetic Particle Imaging is a versatile tool that has the potential to complement or even substitute established techniques especially in diagnostic and interventional medicine. This allows the reduction of radiation exposure connected with current modalities such as CT or PET.

References: [1] Gleich et al., Nature (2005). [2] Han et al., diagnostics (2020). [3] Vogel et al., Phys. Med. Biol. (2016). [4] Graeser et al., Nat. Commun. (2019). [5] Vogel et al., Sci. Rep. (2023). [6] Neumann et al., J. Magn. Magn. Mat. (2022). [7] Vogel et al., Trans. Med. Imag. (2014). [8] Vogel et al., Sci. Rep. (2019). [9] Yu et al., Nano Lett. (2017). [10] Vogel et al., Nat. Commun. (2022). [11] Vogel et al. diffusion-fundamental.org (2014).

CFD-grade MRV measurements of the mean velocity vector and the Reynolds stress tensor in turbulent fluid flows

M. Bruschewski[1], *K. John*[1], *S. Grundmann*[1]
[1]University of Rostock, Rostock, Germany

Introduction: The purpose of this study is to provide highly accurate mean velocity and Reynolds stress data as a basis for the validation and calibration of Computational Fluid Dynamics (CFD) techniques. The Nuclear Energy Agency (NEA) recently introduced a new standard describing "CFD-grade experiments" to ensure the reliability of experimental data [1]. The present study follows these guidelines and describes an experimental campaign using magnetic resonance velocimetry (MRV). The cases examined are single-phase isothermal flows with a Reynolds number of up to 50,000.

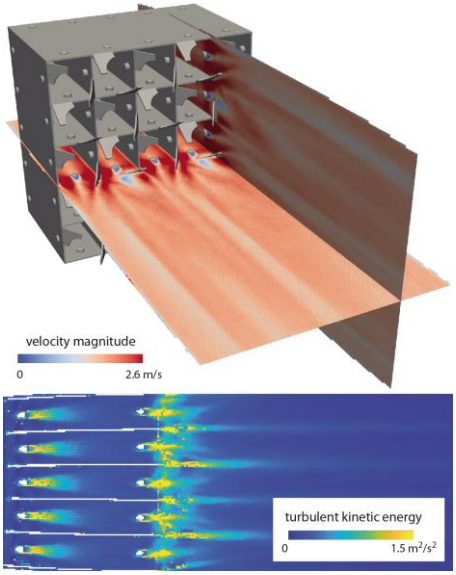

Fig. 1: 3D mean velocity vector and 2D turbulent kinetic energy measured in a replica of a nuclear fuel bundle

Methods: MRV places a number of requirements on the experimental setup, which is why the experiments are usually carried out in a replica system. One of the most important sources of error is the effect of flow displacement. Due to the fluid movement, the measured signal changes its position during encoding, which can lead to distorted data sets. In addition, the velocity encoding time scale is limited by the MRI machine, which can lead to biased results in the Reynolds stress data. The flow system must be scaled such that the maximum flow velocity is sufficiently low and the minimum integral turbulent time scale is sufficiently large. The similarity to the real system is ensured by dimensionless numbers such as the Reynolds number.

Results and Discussion: Based on the results of a previous study [2], velocity-encoded pulse sequences were developed to minimize random and systematic measurement errors in the velocity and Reynolds stress data. Laser Doppler velocimetry measurements served as ground truth. After validation, measurements were performed in a replica of a nuclear fuel bundle shown in Fig. 1. The six-component Reynolds stress tensor was measured at several longitudinal and cross-sections in the channel. Each 2D acquisition took approximately four hours, including ten velocity encode values, six velocity encode directions, and 200 averages each. The large number of signal averages is necessary because all turbulent time scales greater than the repetition time result in signal ghosts. Mean velocity measurements are less sensitive to ghosting and require far fewer averages. With nine averages and four hours total acquisition time, a velocity uncertainty of 1.3% of the bulk flow velocity was achieved in the 3D mean velocity data.

Conclusions: Carefully designed MRV experiments can serve as a basis for the validation and calibration of CFD simulations. High measurement accuracy can be achieved if the system is scaled according to the capabilities of the MRI machine used. The maximum flow velocities and the minimum integral turbulent time scales are of particular importance.

References: [1] NEA (2022), Requirements for CFD-Grade Experiments for Nuclear Reactor Thermal Hydraulics, OECD Publishing, Paris, [2] Schmidt et al. (2021). Reynolds stress tensor measurements using magnetic resonance velocimetry: expansion of the dynamic measurement range and analysis of systematic measurement errors. Experiments in Fluids, 62(6), 121.

Bound and movable fluid microdistribution characterization in porous rocks based on nuclear magnetic resonance

Guowen Jin[1], *Ranhong Xie*[1*], *Jianwei Fu*[1], *Bochuan Jin*[1]
[1]State Key Laboratory of Petroleum Resources and Prospecting, China University of Petroleum (Beijing), Beijing 102249, China

Introduction: Bound and movable fluid microdistribution characterization is important for reservoir evaluation, productivity prediction, and petroleum recovery. However, due to the complexity of the fluid microdistribution in porous rocks, there is currently no effective method to achieve the continuous and quantitative characterization of the downhole or subsurface bound and movable fluid microdistribution[1,2]. In this study, a new method is proposed for bound and movable fluid microdistribution characterization in porous rocks based on nuclear magnetic resonance (NMR) measurements[3].

Methods: The functions describing the distributions of the proportion coefficients of the bound fluid $P_b(T_2)$ and movable fluid $P_m(T_2)$ are expressed as follows:

$$P_m(T_2,\alpha)=e^{-\alpha/T_2} \quad \text{Eq. 1;} \qquad P_b(T_2,\alpha)=1-e^{-\alpha/T_2} \quad \text{Eq. 2}$$

where α is a shape factor that controls the function shapes of $P_b(T_2, \alpha)$ and $P_m(T_2, \alpha)$. Figure 1 shows the $P_b(T_2, \alpha)$ and $P_m(T_2, \alpha)$ with different α. The optimal α (α_{opt}) can be obtained by core experiments. Then the bound fluid distribution $f_b(T_2)$ and movable fluid distribution $f_m(T_2)$ can be obtained using the following equations：:

$$f_b(T_2,\alpha)=\left(1-e^{-\alpha_{opt}/T_2}\right)f_s(T_2) \quad \text{Eq. 3;} \quad f_m(T_2,\alpha)=e^{-\alpha_{opt}/T_2}f_s(T_2) \quad \text{Eq. 4}$$

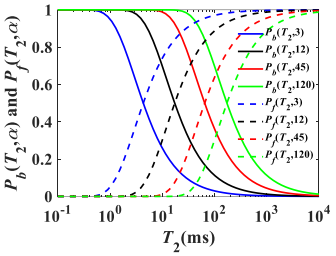

Fig. 1: $P_b(T_2, \alpha)$ and $P_m(T_2, \alpha)$ with different α.

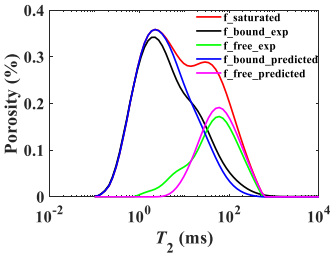

Fig. 2: The predicted bound and movable fluid distributions of a tight sandstone sample.

Results and discussion: Figure 2 shows the prediction results of a tight sandstone sample. It indicates that the predicted T_2 distributions of the bound and movable water agree well with the measured results. Figure 3 shows continuous and quantitative characterization of the bound (the fifth track) and movable fluid distribution (the sixth track) in a tight sandstone reservoir based on downhole NMR logging data.

Conclusion: (1) The exponential functions were used to quantitatively characterize the proportional coefficient distribution of the bound and movable fluid in pores of different sizes, from which the corresponding T_2 distributions of the bound and movable fluid were obtained. (2) The prediction results are intuitive display of the bound and movable fluid microdistribution in pores of different sizes.

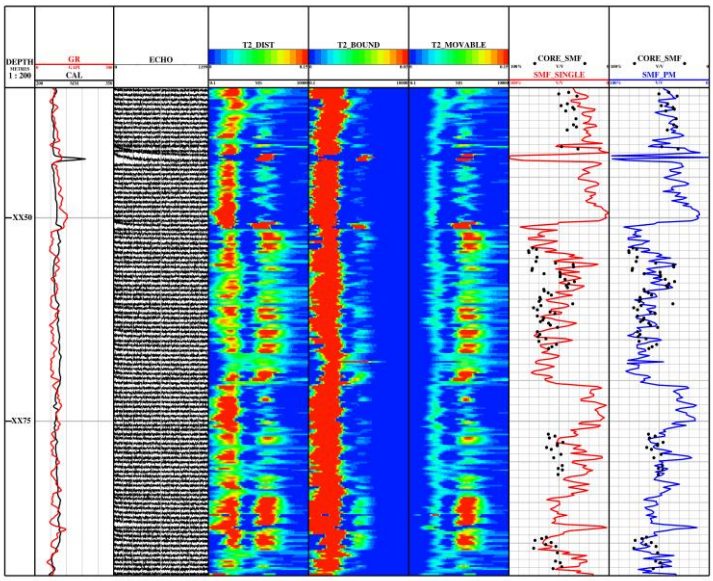

Fig. 3: Continuous and quantitative characterization of the bound and movable fluid distribution in a tight sandstone reservoir based on downhole NMR logging data[3].

Acknowledgements: The work was funded by the National Natural Science Foundation of China (42204107) and Science Foundation of China University of Petroleum, Beijing (2462022XKBH003).

References: [1] Y Q Song, Prog. Nucl. Mag. Res. Sp. (2019). [2] Gruber, J. Magn. Reson. (2013). [3] Guowen Jin, J. Petrol. Sci. Eng. (2021).

Improving the SNR of Unilateral Magnetic Resonance Sensor using LC Resonator

Jiali He[1], *Zheng Xu*[1]
[1] Chongqing University, Chongqing, China, xuzheng@cqu.edu.cn

Introduction: Unilateral or single-sided magnetic resonance (UMR) is constrained by its poor signal-to-noise ratio (SNR). This paper presented method of using LC resonator (Inductor-capacitor series resonant circuit) to increase the SNR of UMR by changing the local RF field distribution. It does not need extra magnets or circuit, experiments show that the SNR of the UMR can be enhanced by up to three times after the LC resonator is loaded.

Methods: Fig. 1 depicts the UMR sensor with a 2D LC resonant coil, and the static magnetic field is 28.18mT. In our work, a method for analyzing the signal strength of UMR sensors with LC resonator has been proposed, which can be divided into 4 steps: Step1, a method of calculating the current in the RF coil including LC resonator is derived according to the equivalent circuit of the coil system. Step2, the equivalent AC resistance of the coil is calculated using the partial-element equivalent-circuit (PEEC) method [1] and Neumann's formula was used to solve the mutual inductance between the coils. Step3, the currents flowed in the RF coil and LC resonantor can be determined. The spread of the spatial magnetic field can be calculated using the Biot–Savart law method. Step4, according to Song's study [2], we got the signal sensitivity of the UMR sensor with and without the LC resonator and analyzed the feasibility of LC resonators, as shown in Fig. 2

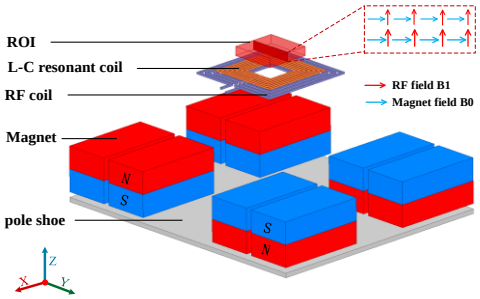

Fig. 1: Diagram of the NMR sensor.

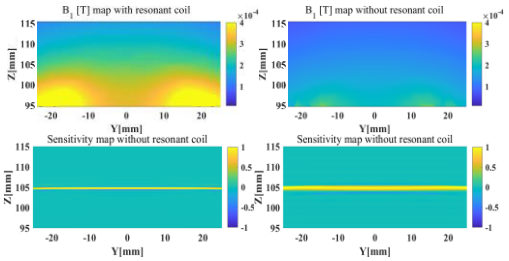

Fig. 2: YOZ planar RF magnetic field distribution and signal sensitivity diagram

Results and discussion: The same test sample (copper sulfate solution) is evaluated using a sensor with and without a resonant coil to confirm the function of the resonant coil. We measured the T2 decay curve of copper sulfate solution, results show that the CPMG echo strength of the UMR sensor can be enhanced from 0.05uV to 0.175uV after the LC resonator is loaded, as shown in Fig. 3. The SNR improves within 30 mm of the coil surface, and this beneficial effect steadily diminishes as the distance increases.

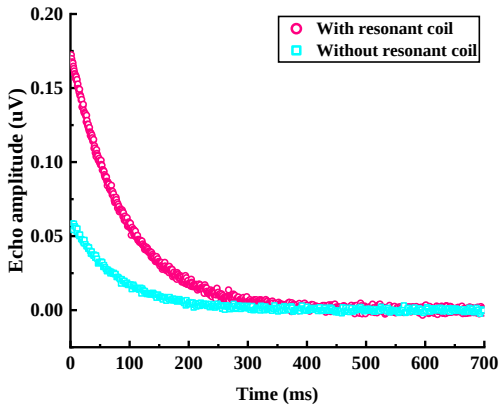

Fig. 3: CPMG echo curve

Conclusion: The LC resonator suggested in this work can significantly boost the signal strength of UMR sensor. The benefits of this approach include a straightforward production procedure, minimal cost, and high viability without modifying the remaining hardware components of the sensor. The facility can be used with sensors for borehole logging and soil moisture measurement, which will greatly enhance the signal strength of the sensors and advance the UMR technology.

References: [1] Xiaohan Kong. Chongqing University, MA thesis (2020). [2] Song et al. Journal of Magnetic Resonance 333(2021): 107082.

Emerging progress of portable NMR instrumentation in industrial application

Huabing Liu[a]

[a] Beijing Limecho Technology Co., Ltd

With a huge diversity of studies performed in nuclear magnetic resonance (NMR) community, permanent magnet technology has been well-developed for portable NMR measurements at laboratory conditions, offering quantitative fluid presence and fluid transport information [1-3]. While operating NMR instruments in the industrial scenarios, it is more challenging in terms of measurement efficiency, safety issues and robustness such as the magnet thermal stabilization and ambient electromagnetic noise shielding. In this abstract, two NMR instruments were designed and applied to the petroleum industry, with great promise for expansion into other subjects.

The first instrument, **F**ield **S**canner using **MA**gnetic **R**esonance (**FSMAR**), is utilized to investigate the fresh rock cores from underground in close proximity to drilling operations. By scanning the obtained rock cores along their cylindrical axis consecutively, this instrument offers the geoscientists with first-hand and high-resolution formation messages regarding pore morphology, permeability and hydrocarbon saturation at different drilling depths. Moreover, FSMAR could be vehicularly deployed close to the drilling platform and therefore minimize the risk of the hydrocarbon escape during the NMR measurement and analysis compared to the routine process, which requires sample transportation to the laboratories.

In the underground sources exploitation, online multiphase flow measurement is crucial for managing and optimizing the production. Since its unique sensitivity to the fluid quantities and types, NMR has been proven as a proper candidate in this topic [4, 5]. Here, the **M**agnetic **R**esonance **M**ultiphase **F**luid analyzer (**MRMF**) was developed to continuously obtain individual phase proportion and phase flow mass of multiphase fluids in the pipelines. Relying on the real-time parameter optimization and data transmission, MRMF has been successfully implemented without sophisticated maintenance. Special hardware designs and software implementations for both aforementioned NMR instruments will be provided at the conference.

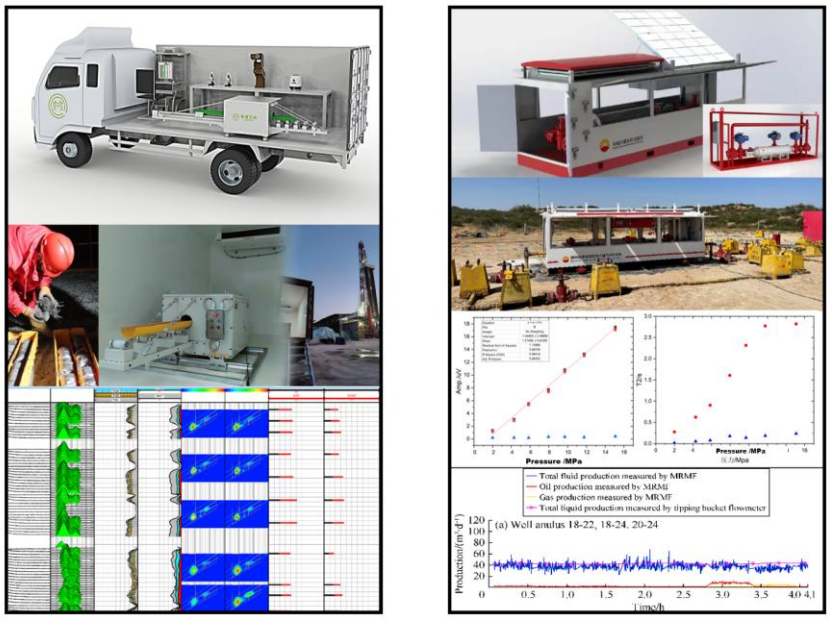

Fig. 1: (left column) The prototypes, operating environment and the scanned results of FSMAR operating in a shale-oil reservoir drilling platform. (Right column) The prototype, operating layout and the recording flow mass of MRMF operating on a high-pressure gas-well pipeline.

References: [1] Blumich B., *JMR*, 2019. [2] Mitchell, J., et al. *PNMRS*, 2014. [3] Luo, S., et al. *MRL*, 2022. [4] Appel, M., et al. *SPE*, 2011. [5] Zargar, M., et al., *SPE*, 2021.

Adaptive Pulse Sequence Design using Neural Networks

T. Parasram[1], *D. Xiao*[1]
[1]University of Windsor, Windsor, Canada

Introduction: In magnetic resonance imaging subjects with different properties can benefit from different pulse sequences or different parameters. Recently there have been developments in optimizing acquisition protocols using machine learning for quantitative chemical exchange saturation transfer (CEST) [1], optimizing gradient and sequence parameters during imaging [2] as well as real-time optimization for quantitative relaxometry [3]. There is potential for machine learning to adaptively update a pulse sequence. In this preliminary work, we trained neural networks (NN) to complete a 1D imaging experiment based on partially acquired k-space data.

Methods: The central 16 points of k-space (64-point image) were used as the acquired signal and input for the network. A NN was trained to generate the k values to be sampled in a 1D imaging experiment as well as reconstruct an image from the acquired data. Random uniform noise and smooth Perlin noise were used to generate the training set of real images, and the k-space signals were obtained using a Bloch simulation. In this work, the relaxation effects were ignored. The network contained three parts. (1) The k value generation network determines a set of 32 values at which to acquire the next 32 datapoints, based on the known 16 complex signals. (2) The k values are then fed directly to a differentiable Bloch simulation which performs an RF excitation and applies the appropriate phase evolution before signal acquisition. (3) The resulting signal and the k values are interpreted by a series of fully connected layers to produce the resulting image. The three parts are connected and trained simultaneously using the Adam [4] optimizer.

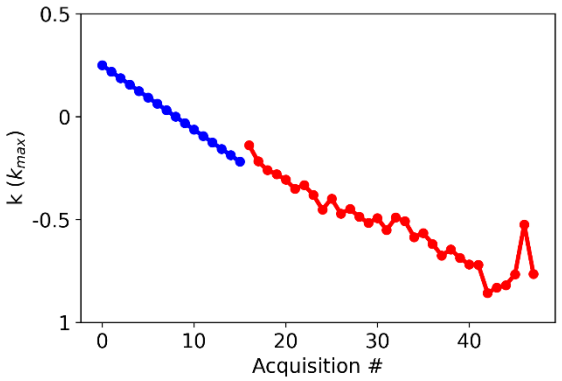

Fig. 1: An example of the NN part (1) output k values is shown in red. The 16 k-space points in blue were provided as input. The output k values by the NN are not fixed to the conventional grid.

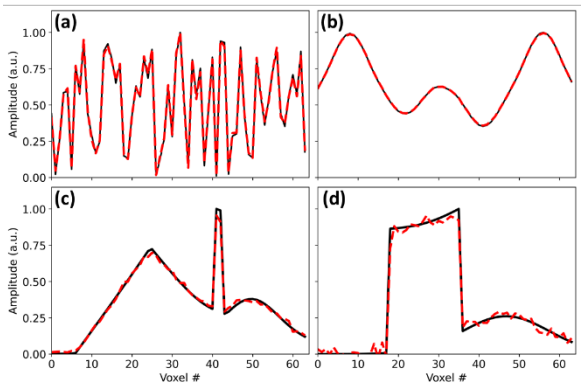

Fig. 2: Four examples of images reconstructed by following the NN protocol (red) compared to the true image (black). (a, b) Examples that share the similar features as the training set, but were not available to the network during training. (c, d) Test images that have different characteristics from the training data.

Results and Discussion: The NN was able to complete a partial Fourier encoding experiment given the central 16 points of k-space. The network in part (1) output the required k values as shown in Fig. 1 in red, with the known k-space data points in blue. The k values varied slightly based on the input image but followed the same trend to cover the lower half of k-space. The reconstruction network in part (3) was able to recover images from the 32 k-space data points acquired at the k values from part (1). This was consistent with the partial Fourier encoding that a real image can be defined by half of the k-space data. Images that share similar features to the training data (Fig. 2a & 2b) as well as images with different characteristics than the training set (Fig. 2c & 2d) can be accurately reconstructed.

Conclusion: In this preliminary work, we have demonstrated that a neural network can learn to complete a pulse sequence based on input signal data. In future work additional constraints and complexities can be included to create adaptive pulse sequences.

References: [1] Perlman, Magn. Reson. Med. (2022). [2] Loktyushin, Magn. Reson. Med. (2021). [3] Tang, Sci. Reports (2021). [4] Kingma, Int. Confe. on Learn. Repre. (2015)

Magnetic Resonance Fingerprinting applied on a 50mT Ultra-low field MRI scanner

Liang Xuan, Yuxiang Zhang, Zheng Xu
School of Electrical Engineering, Chongqing University, Chongqing, China

Introduction: Ultra-low-field magnetic resonance imaging (ULF-MRI) has broad application prospects due to the portable hardware system with low cost. However, compared to commercial high-field MRI, low magnetic field intensity results in a lower signal-to-noise ratio (SNR) in qualitative weighted images. In our work, a magnetic resonance fingerprinting (MRF) approach is applied to an independently developed 50mT ULF-MRI scanner [1] to achieve efficient quantitative imaging, which is an original and promising disease diagnosis approach for ULF-MRI system.

Methods: We created a dataset of 1000 frames with pseudo-random repetition times (TRs) and flip angles, then used the extended phase graph (EPG) [2] to simulate the MR signals of an inversion recovery prepared fast imaging with steady-state precession (IR-FISP) sequence [3], fulfilling an MRF dictionary. The range of values for the parameters T_1 and T_2 is 20~3000ms, resulting in a total of 9708 entries in the dictionary. A phantom of 7 cylindrical tubes with $MnCl_2$ solutions of 0.60mM, 0.50 mM, 0.25 mM, 0.125 mM, 0.08 mM, and 0.04 mM concentrations, as well as distilled water is prepared for ULF-MRF experiment (see Fig. 1). Meanwhile, we used conventional quantitative methods based on standard spin echo sequences to measure the T_1 and T_2 values of each tube, and compared the results with those obtained from MRF data to verify its accuracy.

Fig. 1: Ultra-low-field MRF experimental platform.

Results and discussion: The T_1 and T_2 quantitative maps obtained by ULF-MRF experiment are shown in Fig. 2, where the quantitative value distribution of different tubes is clearly shown. The average quantitative values are compared with the conventional quantitative results using the linear parameter fitting method, shown in Fig 3. Both T_1 and T_2 values from ULF-MRF are consistent with the gold standard methods and exhibit high linearity.

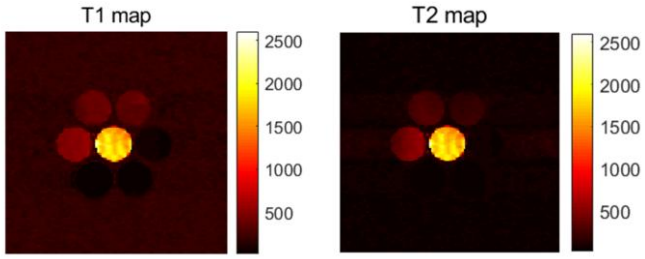

Fig. 2: T_1 and T_2 quantitative maps of the phantom with varied concentration of $MnCl_2$ solutions and distilled water.

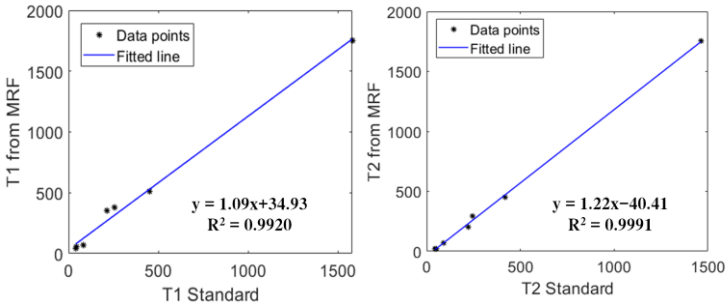

Fig. 3: Gold standard and MRF-based T_1 and T_2 quantitative values comparison and linear fitting results.

Conclusion: From the phantom study, it is concluded that proposed ULF-MRF method can accurately quantify T_1 and T_2 relaxation parameters. In future work, we will extend the method to human brain quantitative imaging.

References: [1] He, et al. J. Magn. Reson. (2020). [2] Weigel, et al. J. Magn. Reson. (2010). [3] Yun, et al. Magn. Reson. Med. (2015).

Acknowledgement: National Natural Science Foundation of China under Grant 52077023, National Natural Science Foundation of Chongqing under Grant cstc2020jcyj-msxmX0340.

Session 4 – 29AM

Hardware & Methods II

Chair: Martin Bruschewski, University of Rostock

Single-sided NMR Technology to Measure Biomarkers of Liver Disease

P. Prado and S. Bussandri
Livivos Inc, San Diego, California, USA

Introduction: An innovative compact Magnetic Resonance (MR) device, capable of accurately diagnosing liver diseases, holds substantial promise for transforming global healthcare. The escalating prevalence of liver disease, impacting more than 20% of the global population, is linked to cardiovascular complications, diabetes, cirrhosis, and cancer. The current available diagnostic modalities present critical shortcomings. While MRI remains the gold standard, its cost and limited accessibility pose challenges. Biopsies are invasive and expensive and Ultrasound-based approaches lack accuracy in assessing steatosis severity.

Fig. 1: MR liver disease diagnostic device (LiverScope®) using a single-sided MR probe mounted on a clinical bed. The LiverScope® is not FDA cleared.

Methods: The LiverScope® introduces a point-of-care diagnostic approach for liver disease, using an open MR probe (12" x 10") to generate a nominal 0.2T field strength (Fig. 2). Custom low-noise radio-frequency electronic components power the bed-mounted probe, while an intuitive graphical user interface controls the clinical tests. The patented open magnet array, combined with advanced data acquisition and signal processing techniques, enables the differentiation of signals from water and fat molecules based on molecular diffusion encoding. Details of the novel method were recently published [1]. Leveraging the strong magnetic field gradient of the open magnet design, the Livivos method offers a robust framework for computing liver disease biomarkers, including Proton Density Fat Fraction (PDFF), alongside T1 and T2 water and fat components.

Results and Discussion: A clinical evaluation of the LiverScope® was conducted at the University of California, San Diego [1]. Fig. 2 shows a comparative analysis with MRI, utilizing certified phantoms and in-vivo liver fat content. Initial PDFF testing substantiated a robust correlation between the MR and MRI results.

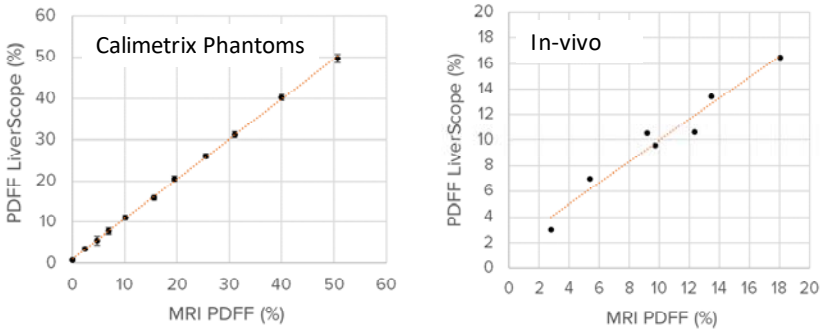

Fig. 2: PDFF measured by the LiverScope® and a commercial MRI scanner. Results from a set of phantoms (Calimetrix) (left) and a clinical study with volunteer patients [1] (right).

Conclusions: Initial findings display promising potential. Further investigations will assess the clinical effectiveness of the LiverScope®. Evaluations of optimized algorithms, backed by funding from pharmaceutical entities and the National Institute of Health (NIH), are currently underway. The successful implementation of this point-of-care liver disease diagnostic solution paves the way for preventive screening and widespread, precise treatment monitoring possibilities.

References: [1] Barahman, MRM (2022) 88 (4) 1794.

Miniaturized Magnetic Resonance Systems and their Applications

D. Kruger[1], A. Zhang[1], G. Yang[1], B. Aghelnejad[1], H. Hinton[1], V.M. Arnal[1], Y. Song[1,2], Y. Tang[3], K. Lei[4], J. Anders[5], and D. Ham[1]

[1]Harvard University, Cambridge MA USA, [2]Massachusets General Hospital, Charlestown, MA, USA, [3]Schlumberger-Doll Research, Cambridge, MA, USA, [4]University of Macau, Macao, China, [5]University of Stuttgart, Stuttgart, Germany

Introduction: Nuclear magnetic resonance (NMR) is a powerful tool for material studies. Recent years have seen a wealth of efforts to miniaturize NMR systems by combining permanent magnets and application-specific integrated circuits (ASICs) for radio-frequency (RF) electronics, in order to bring NMR applications beyond dedicated labs. Here we review integrated NMR electronics and several generations of silicon ASICs capable of producing complex RF pulse sequences for a range of NMR modalities. As a highlight of the review, we will present our latest miniaturized NMR platform capable of high spectral resolution multi-dimensional spectroscopy, multi-dimensional relaxometry, and high spatial resolution magnetic resonance imaging (MRI), the work we recently published in Ref. [1].

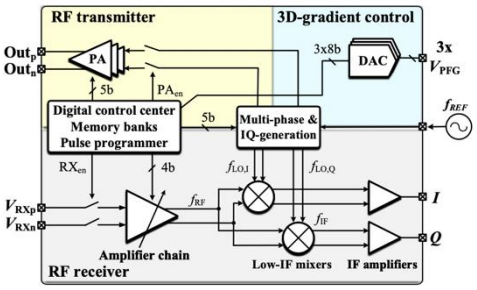

Fig. 1: Block-diagram of the NMR ASIC from Ref. [1].

NMR ASIC and System: Our NMR ASIC from Ref. [1] comprises an RF receiver, an RF transmitter, 3-channel gradient control electronics, and a digital control center (Fig. 1). The RF receiver includes a low-noise amplifier and a variable-gain amplifier, followed by quadrature mixers for frequency down-conversion. The RF transmitter employs a class-E power amplifier with 31 identical parallel branches for output current tuning. The 3-channel gradient control electronics is built around three digital-to-analog converters (DACs) and is engaged when the platform is used for MRI. The heart of the digital control center is an RF pulse sequencer, which comprises a digital logic and a shift-register memory array to store the RF pulse sequence information, such as pulse width, RF phase, and RF amplitude. The sequencer has 3 independent loops to support long and repetitive RF pulse sequences. The digital control center not only produces RF pulse sequences but also operates all different building blocks of the chip in time harmony for complex execution of multi-dimensional spectroscopy and relaxometry, as well as MRI.

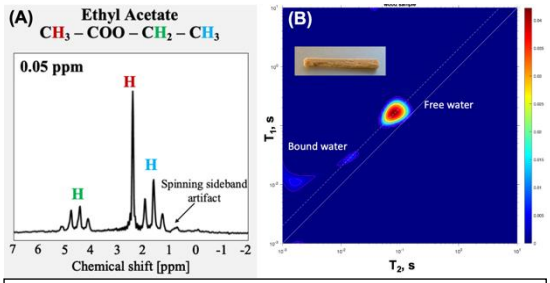

Fig. 2: (A) 1D spectrum demonstrating 0.05 ppm resolution. (B) T_1-T_2 map of a hydrated wood showing free and bound water.

Results: Our system can perform all of spectroscopy, relaxometry, and MRI [1]. Figure 2A shows a 1D spectrum of ethyl acetate, demonstrating a 0.05 ppm spectral resolution. Figure 2B shows a T_1-T_2 map of a poplar wood demonstrating the presence of both free and bound water. For bound water, $T_1 > T_2$, which indicates the water interaction with pore walls. Additional experimental results will be presented at the conference.

Conclusion: Miniature NMR systems can perform a wide range of experiments useful for material studies at molecular scales.

References: [1] D. Krüger *et al*., "A portable CMOS-based spin resonance system for high-resolution spectroscopy and imaging. *IEEE J. Solid-State Circuits* (2023). DOI: 10.1109/JSSC.2023.3274043.

Two-dimensional magnetic resonance data denoising via EMD-SVD

Jiangfeng Guo[a], *Yongjie Zhao*[a], *Ranhong Xie*[a], *Bruce J. Balcom*[b]

[a] State Key Laboratory of Petroleum Resources and Prospecting, China University of Petroleum (Beijing), Beijing 102249, China

[b] UNB MRI Research Centre, Physics Department, University of New Brunswick, Fredericton, NB E3B 5A3, Canada

Introduction: Magnetic resonance (MR) relaxometry, a noninvasive and nondestructive method, is a key technique for the characterizations of physical property and chemical structure. Two-dimensional (2D) MR relaxometry, with two types of relaxation information, is superior to one-dimensional (1D) T_2 relaxometry for the evaluation of the tested sample. The detected 2D MR data, a kind of weak signal, however, is characterized by a low signal-to-noise ratio (SNR), which is adverse to MR spectrum inversion with a high precision. It is therefore necessary to denoise MR data before inversion [1, 2].

Methodology: An empirical mode decomposition-singular value decomposition (EMD-SVD) method was proposed to denoise 2D T_1-T_2 data. The signal is firstly decomposed by the EMD method, and the residual component and the intrinsic mode function (IMF) components at a low frequency part are extracted. The SVD is performed for the high frequency IMF components. Finally, the denoised high frequency IMF components, the residual component, and the low frequency IMF components are summed to obtain the denoised signal.

Simulations and Results: 2D T_1-T_2 spectrum with bound water, movable water, and oil was constructed, as shown in Fig. 1(a), and then T_1-T_2 data were calculated. Gaussian white noise was added to the data with an SNR of 10, as shown in Fig. 1(b). The different denoising method were used to process the noisy data, and the inverted T_1-T_2 spectra using the BRD method were shown in Fig. 1(c)-(f). From Fig. 1, we can see that the inverted T_1-T_2 spectrum with the EMD-SVD denoising is closest to the model, which indicates the EMD-SVD method is superior to the EMD method and the SVD method for MR data denoising. In conclusion, the EMD-SVD method can not only effectively extract the trend component and avoid removing the useful signal in the high frequency signal, but also adaptively select the singular value for signal reconstruction through the singular value difference spectrum, which contains the advantages of the EMD and SVD methods.

Acknowledgments: This work is supported by Young Elite Scientist Sponsorship Program by Bast (No. BYESS2023027) and Science Foundation of China University of Petroleum, Beijing (No. 2462022QNXZ001).

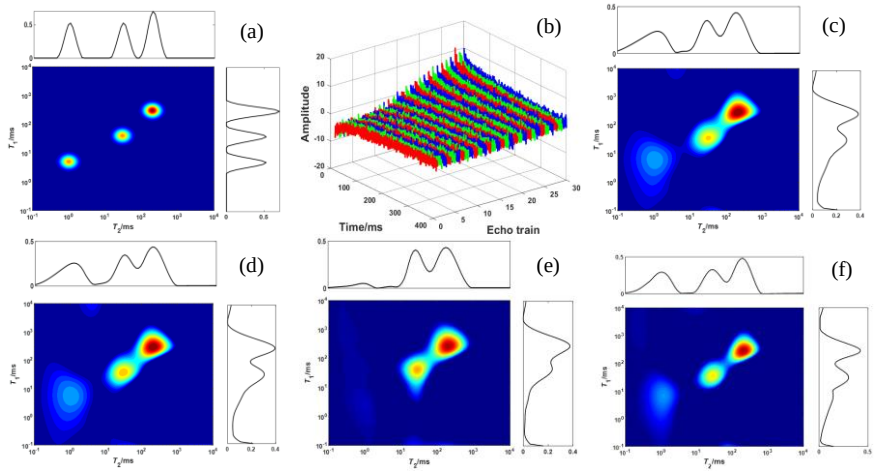

Fig. 1: T_1-T_2 spectrum model (a), the calculated T_1-T_2 data with an SNR of 10 (b), the inverted T_1-T_2 spectrum without denoising (c), and the inverted T_1-T_2 spectra with denoising via EMD (d), SVD (e), and EMD-SVD (f).

References:

[1] Luo S., Xiao L., Jin Y., et al., Petrol. Sci., 2022, 19(2): 581–593.

[2] Guo J., Xie R., Wang Y., et al., IEEE Trans. Geosci. Remote Sens., 2023, 61: 5902014.

Application of artificial intelligence on 2D NMR to identify shale components

Zijian Jia[1], *Can Liang*[2]

[1]University of Shanghai for Science and Technology, 516 Jungong Rd.Shanghai 200093, P.R.China. [2]Changzhou Institute of Technology, No.666 Liaohe Road, Changzhou, Jiangsu Province, China

In recent years, with the emergence of artificial intelligence, especially the entrance of the era of big data and deep learning, machine learning, as the main way of experimental artificial intelligence, may create algorithms to allow computers to learn certain rules from a vast quantity of data The domains of mining and image recognition show exceptional performance. The 2D NMR picture provides information on various components such as organic matter, organic matter pores, oil, gas, water, etc. The NMR response mechanism of each component is distinct, and the response outcomes are varied. With the changing of shale organic matter maturity, organic matter concentration and other component information, the NMR spectrum may change substantially, and the information cannot be quantitatively recognized manually. The adoption of machine learning algorithms can increase the efficiency of NMR data processing. The test findings and nuclear magnetic resonance data are put into the pre-convolutional neural network model, which may increase the accuracy of interpretation and analysis of shale components.

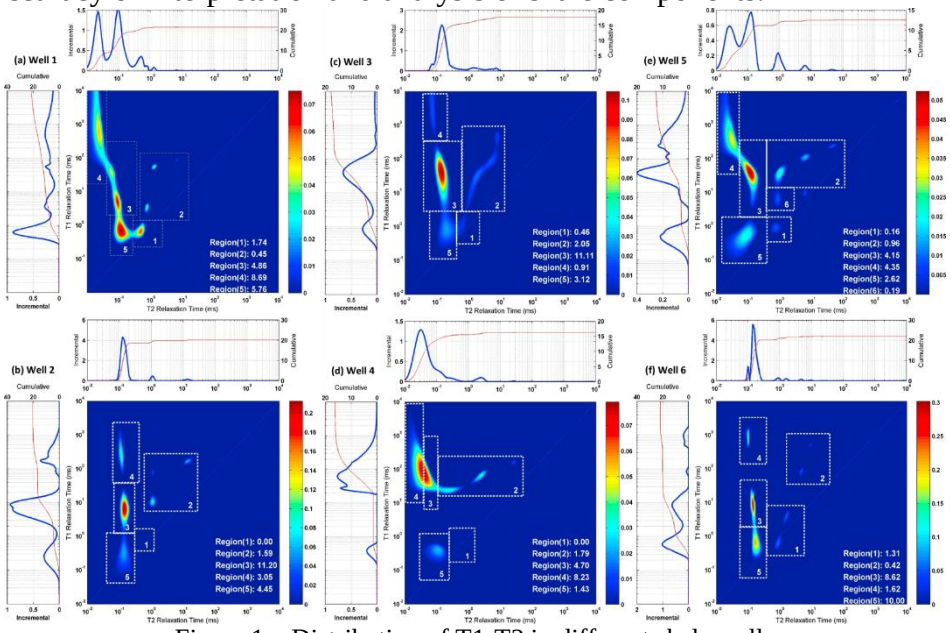

Figure 1 – Distribution of T1-T2 in different shale wells

It has been shown that the ratio of T_1/T_2 and the signal morphology are related to the maturity of kerogen. By carefully evaluating the distribution features of T_1-T_2, as well as the organic matter content, vitrinite reflectance and S1, S2 peaks acquired from pyrolysis, the signals in various sections of the T_1-T_2 map may be separated. solution outcomes (Figure 1). The inclusion of machine learning methods is intended to solve the challenge of identification of shale organic matter and pore characteristics faster and more precisely. Taking the kerogen maturity of shale organic matter as an example, when kerogen matures, it loses aliphatic chains (the component with high hydrogen concentration), aromatic rings form clusters, solid organic matter is tougher, and its T_1 relaxation time gets longer. The T_2 relaxation time of solid organics is virtually constant. Therefore, when the kerogen maturity grows, the T_1/T_2 ratio steadily lowers, and NMR may disclose the maturity stage of the organic matter. Convolutional neural network is utilized to evaluate and model the data of T_1-T_2 spectrum recorded by solid echo pulse sequence. The weighted T_1-T_2 distribution, geochemical parameters, and organic porosity acquired by FEB-SEM are utilized as samples and data labels to create a plausible convolutional neural network (Figure 2) and train it to produce predictions based on different T_1-T_2 maps. The network of organic matter maturity and organic matter porosity; finally, based on the trained convolutional network, the organic matter weighted and organic pore

weighted T_1-T_2 map of shale is applied to realize fast and accurate identification and evaluation of organic matter maturity and organic matter porosity.

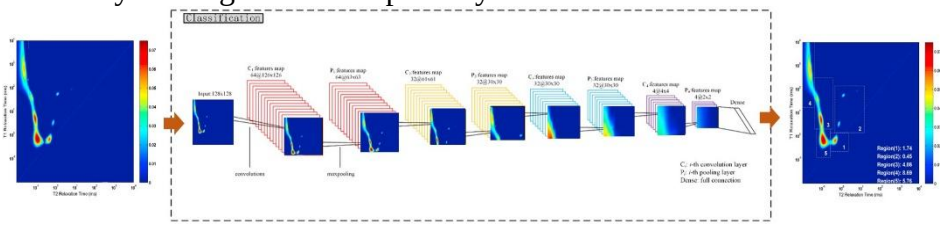

Figure 2 –Schematic diagram of convolutional neural network architecture

References:

[1] Zhou, G. , Gu, Z. , Hu, Z. , Chang, J.， Zhan, H. Characterization and interpretation of organic matter, clay minerals, and gas shale rocks with low-field nmr. Journal of Petroleum Science and Engineering, 2020. 195, 107926.

[2] Seyedalireza Khatibi, Mehdi Ostadhassan; Z. Harry Xie; Thomas Gentzis; Bailey Bubach; Zheng Gan; Humberto Carvajal Ortiz. NMR relaxometry a new approach to detect geochemical properties of organic matter in tight shales. Fuel, 2019, 235 : 167-177.

A Comparative Study of GSP Prediction Utilizing T_2 Relaxation and T_1-T_2 Correlated Relaxation based on Convolutional Neural Network

Yuchen Wu[a], *Xiaowen Jiang*[a], *Zhonghua Ni*[a], *Rongsheng Lu*[a]
[a]School of Mechanical Engineering, Southeast University, Nanjing, P. R. China

Introduction: Glycosylated serum protein (GSP) indicates the average blood glucose level in two or three weeks, and is usually used for glycemic control in diabetes. Previous research indicated that there is a high correlation between low-field nuclear magnetic resonance (LF-NMR) T_2 and T_1 relaxometry and GSP level. In this article, the feasibility of utilizing relaxation signals for predicting GSP level has been studied.

Methodology: T_2 relaxation signals and T_1-T_2 correlated relaxation signals are measured by a LF-NMR analyzer. T_2 relaxation measurement is accomplished by the Carr-Purcell-Meiboom-Gill (CPMG) pulse sequence, and T_1-T_2 correlated relaxation is measured by conventional T_1-T_2 method (IR combined CPMG pulse sequence). Based on convolutional neural network (CNN), prediction models utilizing both T_2 relaxation signals and T_1-T_2 correlated relaxation signals are studied in this research. The models are optimized and well-trained.

Results and discussion: The experimental results are shown in **Table. 1**. The accuracy of prediction model based on T_1-T_2 correlated relaxation is 89.20%, which is a little bit higher than the prediction model based on T_2 relaxation (88.90%). It is indicated that the information provided by T_1 relaxation contributes but not much to the prediction of GSP level. Considering that the time required to measure the T_1-T_2 correlated relaxation signal is much longer than that of the T_2 relaxation signal, it is properly to build prediction model based on T_2 relaxation signal as a trade-off between time consumption and accuracy. Additionally, the prediction of each samples and the corresponding ground truth is presented in **Figure 1.** Since GSP is one but not only type of proteins in serum, the samples that have similar GSP levels but differ in other relaxation components may result in errors. Therefore, a more balanced and comprehensive dataset may help to improve the performance of prediction, which will be further studied in the future.

	T_2	T_1-T_2
RMSE	0.139	0.130
MAE	0.274	0.267
1-MAPE	88.90%	89.20%

Table. 1: The comparison of prediction models based on T2 relaxation and T1-T2 correlated relaxation.

Conclusion: Both models based on T2 relaxation and T1-T2 correlated relaxation achieves a promising result. Considering the longer time consumption of T1-T2 measurement, prediction model based on T2 relaxation signal is more suitable for the prediction of GSP level in human serum. As combining LF-NMR and deep learning technique, it provides a new feasible method for screening and monitoring diabetes.

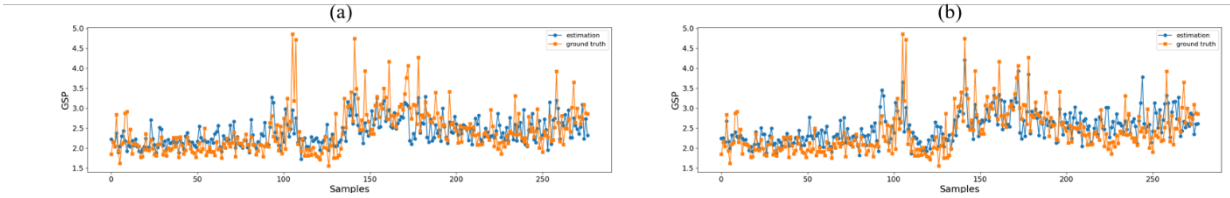

Figure. 1: The prediction of CNN model based on (a) T_2 relaxation, and (b) T_1-T_2 correlated relaxation. The predicted value is drawn in blue circle and the corresponding ground truth is drawn in orange block.

Trajectory design for Spatial Encoding Magnetic Fields

Ying Feng JIANG[1], Jun Qi YANG[1], Ting Ou LIANG[2], Jose GOMEZ TAMES[1], Shao Ying HUANG[2], Wen Wei YU[1]

[1] Chiba University, Chiba, Japan, [2]Singapore University of Technology and Design, Singapore

Introduction: Spatial encoding magnetic fields (SEM) with non-linear gradients relies on mechanical movements of the magnet with respect to the field of view (FoV) for encoding [1, 2]. In an in-situ magnet array, trajectory of the FoV can only be designed when it is much smaller than the bore of the array. For an ex-situ magnet array, e.g., a single sided magnet, the flexibility of designing the trajectory is higher. In this abstract, we demonstrated that trajectory can be designed for a SEM from a single sided permanent magnet array (PMA) for better spatial encoding.

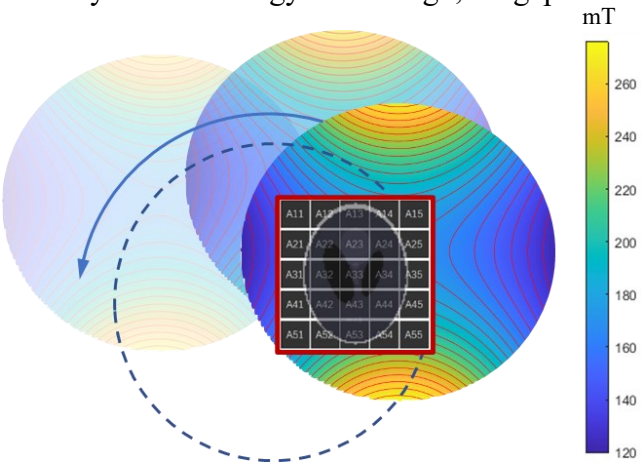

Fig.1 Illustration of magnetic field moving trajectory.

Methods: Figure 1 shows a magnetic field pattern generated by a PMA structure we designed for single-sided MRI [3] moves with respect to a phantom on a regular circular trajectory for spatial encoding. We specifically targeted a quadrupolar distribution in the magnetic field pattern to benefit from the imaging advantages offered by the second-order field. However, the field pattern obtained from the magnet array we designed has a higher gradient strength in longitude direction compared with the ideal quadrupolar field, which results in an irregular k-space pattern, as shown in Figure 2(c-2). To compensate for the deviation, we adapted the trajectory accordingly. More specifically, we reduced the longitudinal span of the circle trajectory to ensure the equality of the gradient field strength in both the latitudinal and longitudinal directions.

Results & Discussions: Figure 2(c-3) and (d-3) shows the local k-space [4] and the reconstructed image with the proposed trajectory. From the comparison of local k-space, we found that the proposed trajectory indeed compensated for the deviation and made the local k-space more uniform. The reconstructed Shepp-Logan phantom using the proposed trajectory exhibited significantly fewer alignment errors and distortions compared to the one reconstructed using a regular circle trajectory. This finding shows the effectiveness of the proposed trajectory for image reconstruction.

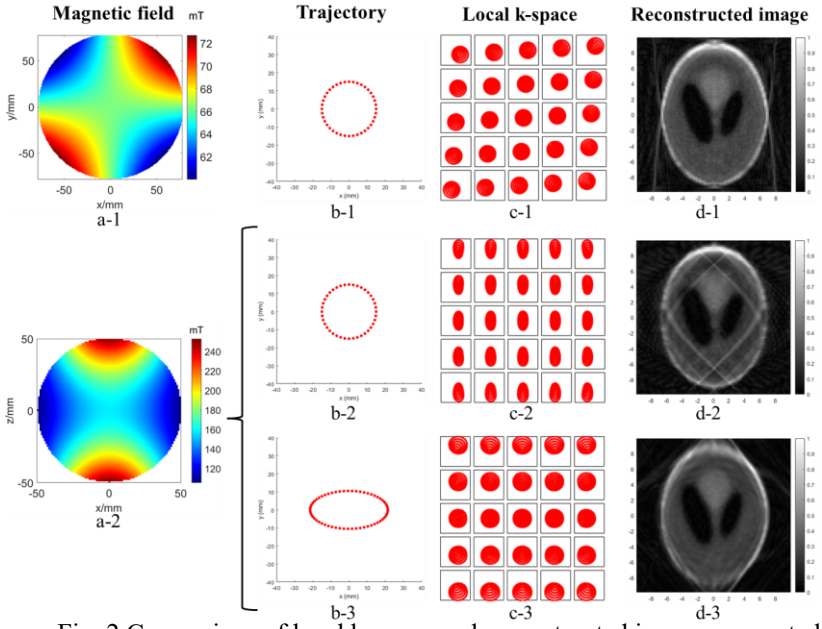

Fig. 2 Comparison of local k-space and reconstructed images generated by ideal and nonideal quadrupolar with different trajectories.

Conclusion: This abstract demonstrated that a well-designed trajectory could compensate for the field pattern deviation, leading to improved imaging outcomes. In future work, emphasis will be placed on further trajectory optimization, based on this work.

References: [1] J. P. Stockmann, et al., Magn. Reson. Med., (2010) [2] C. Z. Cooley, et al., Magn. Reson. Med., (2015) [3] Liang Tingou, et al., J. Magn. Reason., (2023) [4] Gallichan D et al., Magn Reson Med., (2011)

Automated eating quality measurements on lamb carcases in a processing plant using unilateral NMR

E. McCarney[a], *R. Dykstra*[a], *and C. Dykstra*[b]
[a]inMR Measure Ltd, Wellington, New Zealand, [b]Resonint Ltd, Wellington, New Zealand

Abstract: Grading systems within the beef industry have created value along the entire product chain from the farm to the consumer. Carcases in the meat industry are typically graded into separate value brackets based on carcase specific data. However, most of these data are either subjective, unreliable, or not practical to employ on the processing line. One of the main drivers of carcase value is intramuscular fat (IMF), also know as marbling in beef. NMR is a proven tool for measuring the fat and oil content within foods, but the meat industry provides particular challenges such as: large sample, fast cycle time >10/min, specific measurement location, limited footprint for the equipment, harsh environment, use only food safe materials, autonomous due to lack of labor, and integrated into data system. While fat in meat has been measured previously, we have developed the technology to meet the above challenges. Drawing from NMR well logging [1], previous unilateral NMR work [2], and industry experts, we designed, built, and tested a prototype automated carcase grading system that was located at the end of the slaughter floor.

The unilateral NMR magnet and RF coil were designed using finite element analysis and Biot-Savart calculations and then fabricated inhouse. The complete carcase handling and sensor system was assembled with our engineering partner Advanced Engineering Solutions (Feilding, NZ) and then briefly tested in New Zealand at Ovation (Feilding) before shipping to the test site at JBS Bordertown, South Australia. The system was incorporated into a rail in an under utilized chiller next to the end of the slaughter floor. Freshly killed, “hot” carcases, were diverted through our system in batches of 10-30 and automated measurement protocols were used to collect CPMG data for each carcase. The measurement cycle involved advancing the carcase to be in front of the sensor, pushing the carcase against the unilateral sensor, autotuning the probe, collecting NMR data, releasing the carcase, and advance the carcase out of the measurement rig, while at the same time advancing the next carcase into position.

The CPMG fit amplitudes were converted to intramuscular fat. Reference samples were collected the following morning from the fabrication room and sent to the University of New England for gold standard IMF reference measurements. The system was capable of measuring intramuscular fat at the industry standard accuracy of +/- 1% IMF. We were able to measure at a rate of 4.2 carcases per minute.

References: [1] Kleinberg, Sezginer, Griffin, & Fukuhara, J. of Magn. Res. (1992). [2] Casanova, Perlo, & Blümich. Single-Sided NMR. (2011).

Session 5 – 29NOON

MR Microscopy I

Chair: Daniel Clarke, Victoria University of Wellington

Invited Talk 5

5 T Human MRI: RF system and initial in-vivo imaging

Ye Li

Shenzhen Institute of Advanced Technology, Chinese Academy of Sciences

Abstract: Ultra-high field magnetic resonance imaging (MRI) for high resolution images has been increasingly used for clinical and research applications. However, clinical use of ultra-high field MRI were limited due to a number of radio frequency (RF) related challenges. 5 T MRI can provide significant signal-to-noise ratio improvement with less RF interference. In this work, multi-channel RF systems were developed, including a quadrature birdcage transmit/48 channel receiver array for brain imaging, an 8-channel body transmit array / 24channel receiver array for body imaging, a dedicated knee array and 8 channel RF power amplifiers. Global and local SAR analysis was carried out for the RF safety verification. The human brain, cardiac and abdominal images of the world's first 5 T MRI were reported. In vivo human brain and body images were acquired using the 5 T MRI scanner, and were compared with those acquired on a 3 T commercial MRI scanner. The high quality in vivo human brain and body images acquired using the 5 T MRI prototype scanner demonstrated great significance in clinical and scientific research applications.

Iterative Point Spread Function Correction for Fast Spin Echo T_2 Mapping

T. Parasram, M. Armstrong, J. MacNeil, D. Xiao
University of Windsor, Windsor, Canada

Introduction: Spatially resolved T_2 measurement with the multi echo spin echo sequence requires long scan times. Alternatively, multiple T_2 weighted images can be acquired with fast spin echo (FSE) for T_2 mapping with reduced scan time. The point spread function (PSF) in FSE images depends on the image echo time, *k*-space sampling trajectory, and the voxel T_2 value, leading to artifacts in the T_2 map such as blurring and edge enhancement. A simple PSF correction based on an average T_2 can be applied to FSE T_2 mapping [1], but it can be ineffective when a large range of T_2 values are present and can amplify noise. We propose an iterative PSF correction algorithm for accurate FSE T_2 mapping with minimal noise amplification.

Methods: The T_2 and proton density (ρ) maps are iteratively updated to minimize the difference between predicted various T_2 weighting images and the acquired data. The minimization is performed line by line using the Bound Optimization BY Quadratic Approximation method [2] with the following cost function,

$$cost = \sum_i \left\| \boldsymbol{X_i} - \sum_j \rho_j \hat{\mathcal{T}}(j)\mathbf{PSF}(T_{2j}, i) \right\|_2^2, \quad \text{Eq. 1}$$

where $\{\boldsymbol{X_i}\}$ is the set of images with i different echo times, and $\hat{\mathcal{T}}(j)$ is the translation operator. ρ_j and T_{2j} are the proton density and transverse relaxation time at position j, respectively. $\mathbf{PSF}(T_{2j}, i)$ is the PSF for a given T_2 for the ith image.

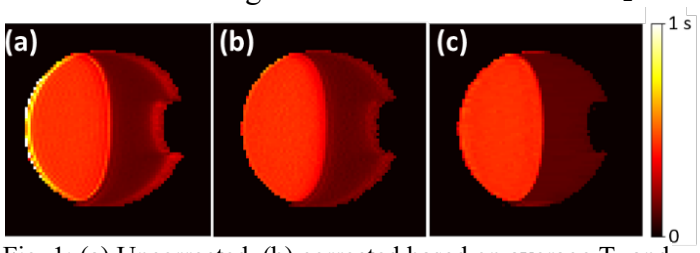

Fig. 1: (a) Uncorrected, (b) corrected based on average T_2 and (c) iteratively optimized T_2 maps for an oil and water phantom. Artifacts were significant at the edges in the uncorrected map and partially removed in the average corrected map with increased noise and blurred boundary. The iterative T_2 map had minimal noise amplification and sharper edges.

Results and Discussion: The method was applied to a simulation (not shown), phantom and tomato measurements.

T_2 maps from an FSE experiment on an oil and water phantom are shown in Fig. 1. The phantom is expected to have sharp interfaces at the edges and between the water and oil phases. The iterative method (Fig. 1c) produced the most accurate T_2 map.

The resulting T_2 and ρ maps for a tomato are shown in Fig. 2. The uncorrected T_2 map had severe edge enhancement where discontinuities in either T_2 or ρ occurred, such as on the tomato surface, around the core and around the seeds. The solid seeds have very short T_2 and therefore did not contribute to the FSE signal. These voxels should have T_2 values equal to the surrounding locular gel and low intensity ρ map due to partial volume effect. The iterative method produced more reasonable T_2 and ρ maps with the highest spatial resolution. The edge enhancement in T_2 map and blurring in ρ map visible in the 1st column were largely reduced.

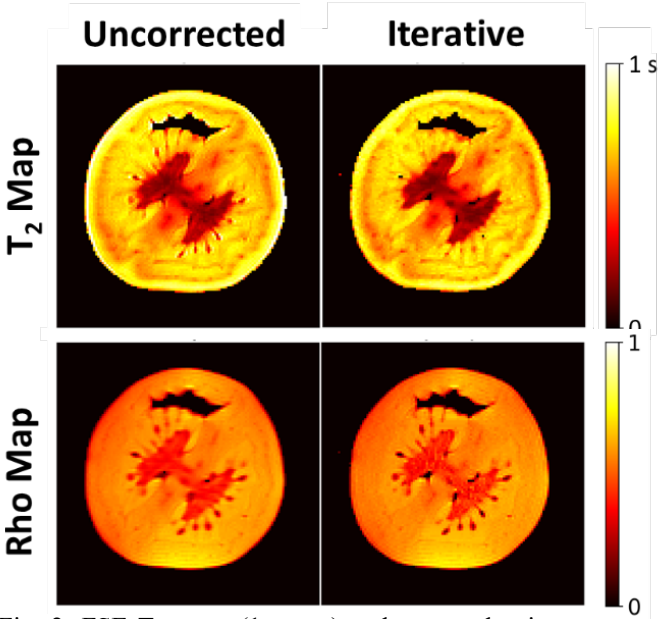

Fig. 2: FSE T_2 maps (1st row) and proton density maps (2nd row) of a tomato without any PSF correction (1st column) and with the proposed iterative correction (2nd column). Matrix size 120x120; processing time 24 min.

Conclusion: An iterative method for PSF correction with FSE T_2 mapping has been demonstrated. Blurring and edge enhancement in the T_2 map and ρ map have been effectively reduced in simulation and MRI experiments. These improvements could enable fast and accurate FSE based T_2 mapping.

References: [1] Zhou et al. JMRI (1993) [2] Powell, DAMTP 2009/NA06 (2009)

MRI methodologies to follow water ingress in pulp-based packaging materials

M. Gunnarsson[a], N. Venkatesh[b], S. Hobson[b], E. Andreasson[c], M. Alexandersson[c], F. Baena-Moreno[b], E. Leventaki[b], D. Bernin[b]

[a]Yangi, Varberg, Sweden, [b]Tetrapak, Lund, Sweden, [c]Chalmers University of Technology, Gothenburg, Sweden

Introduction: Plastic-based food packages have a huge environmental impact. The recent European Union directive on "single use plastics" pushed forward bio-based solutions for straws and food packages. Cellulose pulp e.g. tissue paper is inherently hydrophilic. Sizing is a common procedure to produce hydrophobized pulp by adding chemicals and thermal activation (see inset in Fig.). Cellulose pulp-based packaging materials for e.g. milk are layered composites not suitable for straws or single use food packages. Food packages are produced using dry-forming or a wet-forming processes; the latter being very energy-consuming. These food packages should withstand water and/or oil for at least a couple of hours. Once the material is wet, it becomes soft and looses its mechanical strength. Optimizing these opaque materials—often only 1 mm thick—demands knowledge about the underlying mechanism of fluid transport through the plane e.g. within the fibers or through pores.

Thin materials require high spatial resolution—tens of microns—which is a challenge for MRI when the fluid ingress occurs within minutes. Drying of ink on paper was studied using a spatial and temporal resolution of 10 µm and 1.3 s[1]. Here we developed a 3D printed rig (see Fig. a) to follow the fluid transport in various sized industrially available pulp-based materials through the plane.

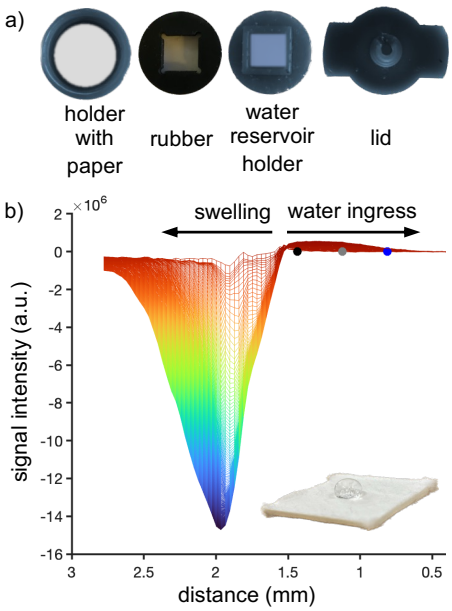

Fig.: Rig setup (a) and normalized ^{1}H profiles stacked with time (b). An example of a sized packaging material in the inset.

Methods: Experiments were performed on a Bruker Avance III 300 MHz with a ^{1}H probe (40 mm diameter). ^{1}H profiles in slices spanning the whole paper area were recorded to follow water entering through the plane using a 1D multi-slice multi-echo sequence. The spatial and temporal resolution was adjusted dependent on the material—various sized dry-formed packing material, straw paper, and sized and coated cardboards.

Results: In the paper or packaging-making process, pulp fibers align in a preferred orientation impacting the fluid transport mechanism. Hence the rig needed to be designed to avoid any fluid getting in contact with the edges. Our first setup revealed—not surprisingly—that the pulp-based material buckles complicating the measurement over a larger area. This was mitigated through implementing a rubber with an open square into which the water was added (see Fig a). Avoiding water to move between the rubber and the paper, a water reservoir holder fitting into the square of the rubber was added. The lid is then screwed until its edges and the reservoir holder exert pressure on the rubber.

Fig b shows that both swelling and water ingress occurred the experiments for a sized packaging material (see inset). Swelling indicates transport within the fibres. It takes 80 min for the water to reach the blue point at distance 1 mm (see Fig b). The fluid ingress depends not only on the sizing but also on the forming process as well as the properties of the fluid. Food containing surface-active fluids, break the hydrophobic barrier.

Conclusions: Following the fluid ingress through the plane into packaging materials using MRI paves the way for a better understanding of the underlying transport mechanisms. The gained knowledge is of importance for modelling of fluid transport.

References: [1] Perrin et al. Chem. Eng. Sci. (2022).

DTI-measured diffusion directionality captures fluctuation in renal water reabsorption induced by water diuresis

Chang Ni[1], Xin Mu[1], Yanbin Li[2], Mingyan Wu[2], Jeff L. Zhang[1]

[1]BME, Shanghaitech University, Shanghai, China, [2]Central Research Institute, United Imaging Healthcare Group, Shanghai, China

Introduction: Water reabsorption is an important aspect of renal function [1]. In water diuresis, increasing water intake would increase tubular water flow and reduce water reabsorption. Diffusion tensor imaging (DTI) technique is capable of capturing directions of water diffusion in tissues [2], so may potentially detect the above-mentioned diuretic changes. In this study, we tested the value of DTI in assessing water reabsorption of kidneys, specifically how primary diffusion direction and fractional anisotropy (FA) change with water diuresis.

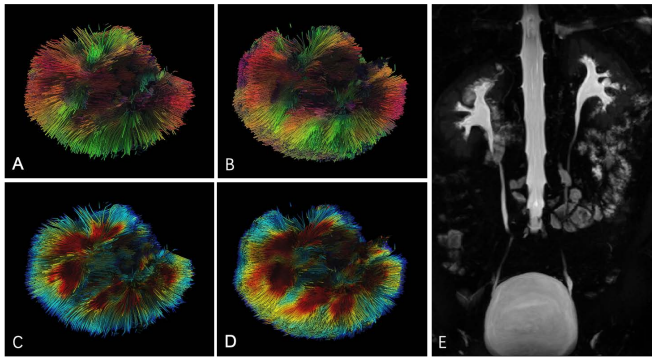

Fig. 1: A and B: Pre- and post-water fiber tractography with conventional color-coding. C and D: Tractography with color-coding based on AD of local origin. E: MRU acquired 1 hour afterwards.

Methods: We included 4 healthy subjects (3 males, 24.0±2.3 years) in this study, and all signed written consent forms before the experiment. The subjects were asked fast from food and water 10 hours before their visit. Scans were performed on a 3T MR scanner (uMR890, United Imaging Health). DTI (one axial slice, b = 0, 500 sec/mm^2, 24 directions) was first performed as baseline, subjects drank 10 ml/kg water within 10 minutes, and DTI scan was repeated every 10 minutes for an hour. At the end, MR urography was performed for estimating urine volume. With the DTI images, three eigenvalues and their corresponding eigenvectors were obtained [3]. FA was computed as normalized RMSD of the eigenvalues. Regions of interest (ROIs) were placed on renal pyramids (5~7 per subject). For every voxel in a pyramid, we computed the angular difference (termed as "AD") between its first eigenvector's direction (primary diffusion direction) and the tubules' direction. The latter direction was estimated by a line from the voxel to an origin point manually placed at the apex of a pyramid. Both FA and AD were averaged over ROI of each pyramid.

Results and discussion: Compared to conventional color-coding, the new tractography with angular difference coding shows changes of water diffusion direction before and after water intake in a clearer way (Fig. 1). FA increased by 0.11±0.08 at 10 min after water intake and returned to baseline within 30 minutes. AD increased by 0.08±0.04 at 20 min and returned to baseline at about 50 min after water intake. The slight increase of AD at 60 minutes was presumably due to pressure from the filling bladder.

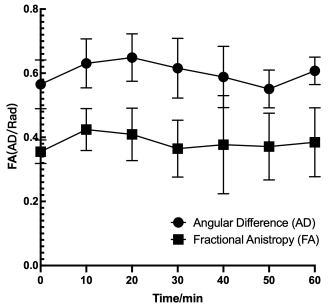

Fig. 2: The average FA and AD measured in 4 subjects.

Conclusion: Changes in tubular flow vs water reabsorption as induced by water intake were successfully detected by fractional anisotropy and angular difference measured with DTI images. Using angular difference for direction color-coding, the tractography visualizes the water-diuretic changes more clearly. These findings suggest that diffusion tensor imaging may be a valuable tool for assessing water reabsorption and tubular function.

References: [1] Feraille, Eur J Physiol. (2022). [2] Sigmund, Radiology. (2012). [3] Ljimani, Magn Reson Mater Phy. (2020).

Massively multidimensional diffusion MRI: from concepts to restriction sensitive and sparsely-sampled acquisition

Maxime Yon[1,2], *Omar Narvaez*[2], *Alejandra Sierra*[2] *and Daniel Topgaard*[1]

[1]Lund University, Lund, Sweden
[2]A.I. Virtanen Institute for Molecular Sciences, University of Eastern Finland, Kuopio, Finland

Introduction: Diffusion MRI indirectly depicts the tissue's microstructure at a few micrometers scale through the water diffusion and characterizes it with quantitative metrics such as fractional anisotropy, mean diffusivity, or diffusion tensor. However, its limited spatial resolution, superior by 1 to 3 orders of magnitude to the diffusion extent, leads to voxel-averaged parameters and ambiguities in their interpretations. This length scale gap can be bridged by using non-parametric diffusion tensor distributions (DTDs) to describe the heterogeneity of the microstructure at a sub-voxel level. The specificity required to disentangle the DTDs is obtained by the acquisition of numerous images, weighted by b-tensor gradient waveforms leading to specific signal attenuations for different microstructures. This approach can also be combined with variable TR and TE acquisition providing a better separation and quantification of the DTDs via T1 and T2 correlations. Recently, our group also introduce the use of frequency-dependent diffusion encoding to separate the effect of restriction and diffusion enabling the depiction of the cellular density of biological tissues and leading to the 7D Massively Multidimensional diffusion (MMD) approach [1,2].

Aim: In this presentation, I intend to exemplify the possibilities offered by MMD to provide a specific description of the contribution of cell types, local chemical composition, axonal density, restriction, and orientations at a sub-voxel level in ex vivo brain allowing MRI to compete with histology. I will also discuss the various strategies for rapid and sparsely sampled acquisitions of such a massively multidimensional dataset.

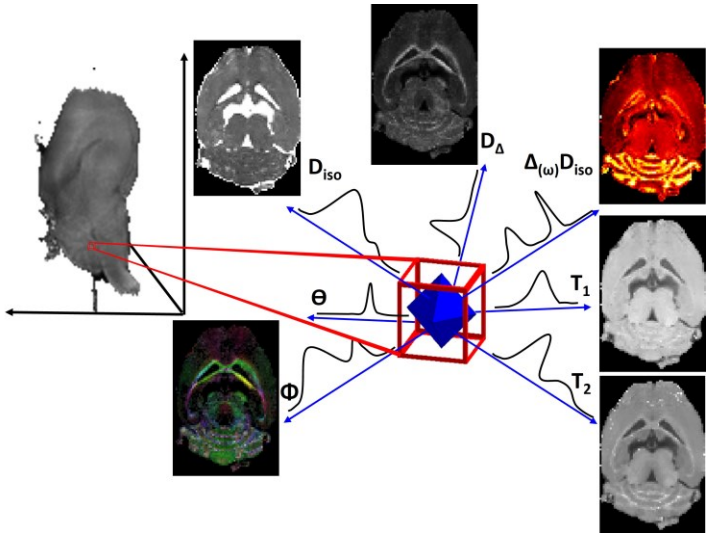

Figure 1: MMD parameters maps of an ex vivo mouse brain. Diffusion's restriction map ($\Delta_{(\omega)}D_{iso}$) on the top right

Material & methods: MMD MRI data were acquired at 11.7 T on an ex vivo mouse brain with a variable flip angle RARE sequence and sparse k-space sampling. Image reconstruction was performed with BART's compressed sensing and locally low-rank algorithms.

Results: The combined use of ultrafast sequences with sparse sampling allows for reducing the acquisition time of 3D MMD datasets by more than 100. The MMD maps allow a unique depiction of the tissue microstructure such as the cell cytoplasm density evidenced by the diffusion's restriction in the cerebellum of the mouse brain.

Conclusion:
Massively multidimensional diffusion increases diffusion's specificity by describing the contribution of cell types, local chemical composition, axonal density, restriction, and orientations at a sub-voxel level, allowing MRI to compete with histology. The fast acquisitions allowed by ultrafast sequence and sparse acquisition are now the key to broaden its applications and usability.

References: [1] Narvaez, Frontiers in Physics (2022). [2] Narvaez, AchivX (2021).

Effects of geometry and relaxation on diffusion exchange measurements

Alfredo Ordinola [1], *Magnus Herberthson* [2], *Ruiliang Bai* [3], *Evren Özarslan* [1]
[1] Department of Biomedical Engineering, Linköping University, Linköping, Sweden
[2] Department of Mathematics, Linköping University, Linköping, Sweden
[3] School of Medicine, Zhejiang University, Hangzhou, P.R. China

Introduction: Water exchange in complex media has been modeled through different frameworks using diffusion magnetic resonance (dMR) data, such as the filter exchange imaging (FEXI) framework [1]. However, geometry and relaxation effects are often disregarded or simplified in such methods, which can lead to deviations in parameter estimates. The aim of this work is to explore such effects on the signal, and estimated exchange parameters obtained via FEXI.

Methods: The Bloch-Torrey equation [2] can be written as follows:

$$m_t(\boldsymbol{r},t) = \nabla[D(\boldsymbol{r})\nabla m(\boldsymbol{r},t)] - i\gamma g(t)\boldsymbol{r}m(\boldsymbol{r},t) - \mathrm{R}(\boldsymbol{r},t)m(\boldsymbol{r},t) \quad \text{Eq.1}$$

where $m(\boldsymbol{r},t)$ denotes the magnetization, $D(\boldsymbol{r})$ the diffusivity, γ the gyromagnetic ratio, $g(t)$ the gradient waveform, and $\mathrm{R}(\boldsymbol{r},t)$ the relaxation rate. The latter accounts for T_1 relaxation only in-between the second and third 90° RF pulses in the sequence shown in Fig. 1a. By introducing spatial periodicity conditions and solving Eq. 1, we obtain the magnetization and signal value for general gradient waveforms using a multiple correlation function (MCF) approach [3,4]. The one-dimensional model employed in this study is presented in Fig. 1b. Six different combinations of lengths, diffusion coefficients and relaxation rates were studied. Signals for a single $b_1 = 3ms/\mu m^2$, 13 b_2's with $b_{2_{max}} = 3ms/\mu m^2$, and 15 t_m's with $t_{m_{max}} = 400\,ms$ were computed, as well as the apparent diffusion coefficient (ADC) for each t_m to estimate exchange parameters via FEXI.

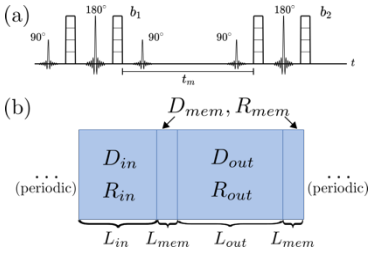

Fig. 1: (a) Double Diffusion Encoding (DDE) stimulated echo sequence. (b) One-dimensional model representing a cellular environment.

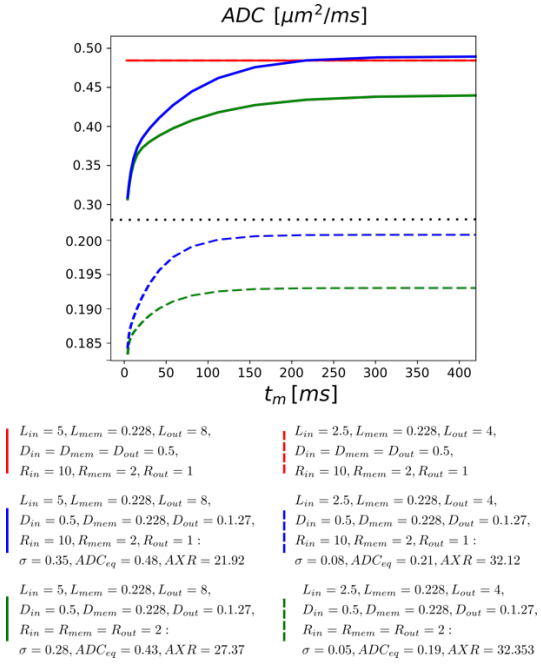

Fig. 2: ADC recovery curves and the FEXI exchange parameters (σ, ADC_{eq}, and AXR obtained for different arrangements. Dotted line indicates a change in y-axis scaling. L in μm, D and ADC_{eq} in $\mu m^2/ms$, R and AXR in s^{-1}.

Results and Discussion: The main results of this study are shown in Fig. 2. For the same diffusion properties, varying relaxation rates results in higher ADC values, while a change in geometry shows both this feature and an upward shift of the same curve. These changes directly affect the estimated exchange parameters in the FEXI analysis, even if the fractional population in both compartments, as well as the membrane permeability (defined as D_{mem}/L_{mem}) are kept constant.

Conclusion: In conclusion, we presented a one-dimensional periodic model and simulation framework capable of providing signal values for general gradient waveforms. Furthermore, we showed the impact of not accounting for geometry and relaxation effects in stimulated echo DDE measurements, and how the parameter estimates are affected by ignoring such effects.

References:

[1] Lasič, Nilsson, Lätt, Ståhlberg, Topgaard, Magn. Reson. Med. (2011)
[2] Torrey, Phys. Rev. (1956)
[3] Grebenkov, Rev. Mod. Phys. (2007)
[4] Grebenkov, J. Magn. Reson. (2010)

Session 6 – 29PM

MR Microscopy II

Chair: Diana Bernin, Chalmers University of Technology

Towards open-source MR software and hardware with Pulseq and CoilGen

M. Zaitsev[a]

[a]Division of Medical Physics, Department of Radiology, University Medical Center Freiburg, Faculty of Medicine, University of Freiburg, Freiburg, Germany

Introduction: MRI is a mature non-invasive medical imaging technology, which is evidenced by the fact that the human MRI machines from all major manufacturers have very similar technical specifications. Nonetheless, the development and dissemination of novel MR acquisition techniques is hampered by the notoriously difficult and time-consuming task of implementing (i.e., programming) new methods on a particular MR vendor's platform since it must be done using that vendor's low-level and proprietary programming environment. Furthermore, distributing a new pulse sequence to another vendor's platform is generally not possible since each vendor's software ecosystem is different and tightly sealed. This discourages scientific and clinical collaboration by introducing artificial boundaries, leading to fragmentation within the research community and slowing down validation and adoption of the new imaging methods. The vast majority of the human MRI research labs, which actively contribute to the methodological research are "bound" to a specific vendor, and in this way do not directly benefit from technical developments from other parts of the MR research community.

Whereas for image reconstruction and image post-processing a great variety of open source software tools exist, little can be found for the MR pulse sequence design and even less so for the MR hardware. With our recent tools Pulseq[1,2] and CoilGen[3,4] we are attempting to change the established predominantly proprietary landscape by contributing towards the open source and open science culture[5].

Our **CoilGen Project** is a community-based tool for the generation of gradient and shim coil layouts intended for the use in MRI/NMR environments. It is based on the boundary element method and generates electrically interconnected non-overlapping wire tracks on almost arbitrary 3D supporting structures. Although the tool is capable of generating the stream function of the electric current density based on the user-provided target field, the main focus of this work is the post-processing, leading to a ready-to-manufacture wire track.

With our **Pulseq Project** we have established an open source framework for the development and execution of magnetic resonance pulse sequences for imaging and spectroscopy. It allows one to program MRI sequences directly in high-level visual programming environments, such as Matlab or Python. Thereafter pulse sequences are exported to a well-documented Pulseq file format, which is a text file structured according to the Pulseq specification[1]. A Pulseq file can either be executed on the real MR hardware, such as Siemens or GE whole-body scanners or table-top MR based on a Red Pitaya board[6], or archived with the data to be shared with the manuscript as a documentation of the detailed parameters of the particular MR experiment. Pulseq has also been widely adopted as the input or exchange format in numerous generic MR simulation software packages.

Pulseq supports reproducible research by enabling researchers to publish and share the exact Pulseq sequence used to acquire the data. This contrasts with the current practice of publishing coarse pulse sequence "timing diagrams" that generally only convey the design intent and not the details required to reproduce the work. Pulseq framework is not restricted to a particular type of a sequence and can be extended in future to include further features, vendors and spectrometer types.

References: [1] http://pulseq.github.io/ [2] Layton, MRM 2017, doi:10.1002/mrm.26235; [3] https://github.com/Philipp-MR/CoilGen [4] Amrein, MRM 2022, doi: 10.1002/mrm.29294; [5] https://www.opensourceimaging.org/ [6] Negnevitsky, JMR 2023, doi: 10.1016/j.jmr.2023.107424.

Forward and Inverse Models on the 3-D MRI-Based Electrical Properties Imaging

Yuyue Zhang, Tiantian Yin, and Xudong Chen
National University of Singapore, Singapore

Magnetic resonance imaging (MRI)-based electrical properties imaging (EPT) is a quantitative imaging method that retrieves the permittivity and conductivity of biological tissues using an MRI system [1-2]. The modeling of MRI-EPT involves the 3-D interaction of biological tissues and electromagnetic fields, which presents higher requirements for accurate modeling and solving of forward and inverse problems. In this abstract, the rooftop function basis is utilized to accurately and efficiently model and solve the electric and magnetic fields under the 3-D model, which can avoid the discontinuity of the electrical current at the grid boundary. In the inversion process, the subspace-based optimization method (SOM) is used to quantitatively retrieve the permittivity and conductivity of the scatterers [3-4]. The data function and state function are reorganized based on the rooftop function basis. The numerical results validate the feasibility of the proposed method, providing a potential way to quantitatively image biological tissues.

In the forward process of 3-D electromagnetic numerical calculations, errors can occur due to current discontinuity at the grid boundary when using the point matching method. In this abstract, we use the transpose-free quasi-minimal residual (TFQMR) algorithm which is based on the roof function basis to avoid such error [5]. Additionally, the fast Fourier transform (FFT) is employed to accelerate the calculation, resulting in a more accurate and efficient calculation of the electric and magnetic fields in the domain of interest (DoI).

In the inversion process, the data function (1) and state function (2) are firstly rewritten with the rooftop function basis

$$\bar{B}_{sca}^{+} = \bar{\bar{G}}^{+} \cdot \tilde{J} \tag{1}$$

$$\tilde{J} = \bar{\bar{\chi}} \cdot \left(\bar{E}^{inc} + \bar{\bar{G}}^{EJ} \cdot \tilde{J} \right) \tag{2}$$

where $\bar{B}_{sca}^{+}$ represents the positive rotating scattered magnetic field, $\tilde{J}$ represents the induced current in the rooftop function basis, $\bar{\bar{\chi}}$ denotes the contrasts of scatters to the background. $\bar{\bar{G}}^{+}$ and $\bar{\bar{G}}^{EJ}$ are the Green's functions mapping the induced current to the positive rotating scattered magnetic field and scattered electrical field, respectively. Then, the $\bar{\bar{G}}^{+}$ is decomposed by singular value decomposition (SVD). The induced current can be divided into the major part and the minor part according to the singular value. The minor part of the induced current is then expanded using Fourier basis and reconstructed using an optimization method, resulting in the reconstruction of the electrical properties.

Compared to previous MRI-EPT methods that used pulse function basis, this abstract uses the rooftop function basis to overcome the issue of current discontinuity on the grid boundary in the 3-D model. As a result, the proposed method allows for more accurate forward calculation and inverse reconstruction.

References:

[1] R. Leijsen, W. Brink, C. van den Berg, A. Webb, and R. Remis, Diagnostics, (2021).
[2] A. J. Garcia Inda, S. Y. Huang, N. Imamoglu, and W. Yu, IEEE Trans. on Image Process., (2022).
[3] Y. Zhong, X. Chen, and K. Agarwal, IEEE Trans. Geo. Remote Sens. (2010).
[4] Xudong Chen, IEEE Trans. Geo. Remote Sens. (2010).
[5] C. F. Wang and J. M. Jin, IEEE Trans. Microw. Theory Tech. (1998).

Precise tracking of calf muscle fiber orientations during plantarflexion with diffusion tensor imaging

Xin Mu[1], *Chang Ni*[1], *Haikun Qi*[1], *Jeff L. Zhang*[1]
[1]School of Biomedical Engineering, Shanghaitech University, Shanghai, China

Introduction Exercise relies on muscle contraction, and on the microstructural level, such contraction involves changes in the orientation of all the muscle fibers of the muscles. Precise tracking of muscle fibers' orientation may reveal valuable microstructural information on muscle function or performance. For example, it may gain us insight into muscle's ability in generating tension through contraction and deformation, how muscle adapts to injury and physical therapy [1], and how muscle's micro-structural performance would impact its function [2]. In this study, we developed a DTI-based method for quantifying muscle fiber orientation and tested it on calf muscles at different degrees of plantarflexion.

Methods With IRB approval, we recruited 4 healthy subjects. On a 3T MRI scanner (uMR890, UIH), the right lower leg of the subject was scanned with a 24-channel knee coil, using a gradient echo sequence: b values 0 and 400 s/mm^2, TE/TR 60/4000 ms, 12 directions, FOV 200×200mm. The scan was repeated with the ankle positioned at various angles relative to its neutral position: -15° (dorsiflexion), 0°, 15°, 30°, and 45°. Voxel-wise exponential fitting was implemented for each set of DTI data to obtain the principal eigenvector map. For each voxel, we computed the angle between its principal eigenvector and the unit vector [1,1,1] as the voxel's fiber angle (denoted as θ). To evaluate potential changes of fiber angle for each muscle group, we manually drew regions of interest (ROI) for medial gastrocnemius (MG), soleus (SOL), and tibial anterior (TA).

Results and discussion As the ankle angle changed from dorsiflexion to plantarflexion, the average angle in the MG gradually increased from 0.87±0.03° to 1.09±0.04°, while the average angle in the TA gradually decreased from 1.09±0.03° to 0.93±0.04°(Fig.1). Compared to the neutral position, fiber angle distribution in the 45° plantarflexion position shifted to higher θ for the MG, slightly higher θ for the SOL, and lower θ for the TA. Furthermore, the fiber direction change can be seen in the color-encoding tractography (Fig.2).

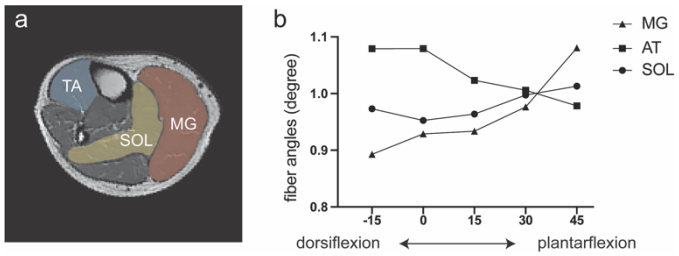

Fig. 1. a, Manual ROI muscle segmentations of the subject's axial calf image. **Fig. 1. b**, Muscle fiber angle changes at different degrees of plantarflexion.

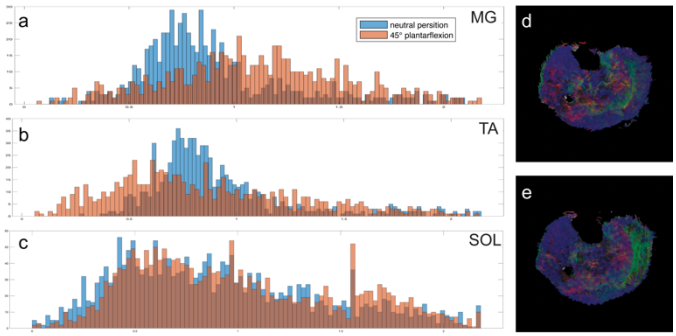

Fig. 2. a-c, The fiber angle distribution histogram of MG, TA, SOL of an axial slice of a subject's calf. The blue bin stand for the neutral position, and the red bin stands for the 45° plantarflexion. **Fig. 2. d-e**, The REB-encoding tractography of neutral position, and 45° plantarflexion position.

Conclusion With DTI, the fiber orientation of calf muscles can be measured, and its measured change between different degrees of plantar flexion agrees with muscle physiology. Future efforts will be devoted to investigations on either comparison between different subject groups or longitudinal assessment following training or treatment.

References

[1] Laura, PLOS ONE. (2022). [2] Wim, Diffusion Tensor Image, Springer. (2016).

High-resolution Quantitative Susceptibility Mapping for Beta-amyloid Pathology

Nian Wang[1,2], Surendra Maharjan[1], Abigail Wallace[1]
[1] Department of Radiology and Imaging Sciences, Indiana University, Indianapolis, Indiana, USA
[2] Stark Neurosciences Research Institute, Indiana University, Indianapolis, Indiana, USA

Synopsis
Alzheimer's disease (AD) is an age-associated neurodegenerative disease that is reaching epidemic proportions as a result of the aging of the world's population. It is likely that the most effective treatment for AD will need to be administrated before cognitive symptoms occur, necessitating a biomarker for the early stages of AD. Novel high-resolution MRI technologies with the capability to characterize the individual beta-amyloid plaque through the whole brain is highly desirable.

Purpose: To detect and quantify the beta-amyloid plaques through whole mouse brain using high-resolution Quantitative susceptibility mapping (QSM).

Introduction
Although the cause of AD is not fully understood, clinical and neuropathological studies have hypothesized that the formation of beta-amyloid (Aβ) plaques and tau neurofibrillary tangles are crucial to the pathogenesis of AD.[1,2] Quantitative susceptibility mapping (QSM) affords unique image contrasts and has gained prominence to non-destructively probe the tissue microstructure.[3] The capability of distinguishing the individual plaques by high-resolution QSM could be a sensitive imaging biomarker for detecting and monitoring Aβ pathology of AD.[4]

Methods
Animal experiments were carried out in compliance with the local IACUC Committee. The B6, 5xFAD, 5xFAD^{P522R} (P522R is a protective variant for AD), and 5xFAD^{M28L} (M28L is a risk variant for AD) mice were chosen for brain imaging. Animals were sacrificed and perfusion fixed with a 1:10 mixture of ProHance-buffered formalin to shorten T1 and reduce scan time.[5] The specimens were scanned at 9.4 T (Bruker, Billerica, MA) scanner using a modified 3D multi gradient echo (MGRE) pulse sequence at 25 μm isotropic resolution. The repetition time (TR) was 100 ms with 2 echoes. The phase data from the MGRE acquisition was used to reconstruct QSM images using STI Suite (University of California, Berkeley, CA).[3,6] The phase of the raw data was unwrapped using a Laplacian-based phase unwrapping method. The background phase was removed using the V-SHARP method. The magnetic susceptibility was then obtained from the local tissue phase by solving an inverse problem using the improved LSQR (iLSQR) method. After MRI, the brain samples were performed with conventional histology for beta-amyloid to validate MRI findings.

Results
Figure 1 shows the representative T2*-weighted image of both WT (B6) and AD (5xFAD) mice. Compared to the B6, there are numerous hypointensity signals in the cortex region and hippocampus region (red and yellow arrows). These hypointensity areas are likely the beta-amyloid plaque deposition. To validate the MRI findings, the QSM results were compared with beta-amyloid plaque staining (Figure 2). The plaques detected by QSM correlated well with the conventional histology in the cortex region. The plaque loading showed no significant difference between QSM and histology ($p = 0.087$). Figure 3 showed the beta-amyloid plaques detected by QSM and T2*. Compared to QSM, the plaques in the cortex and hippocampus (yellow and green arrows) are barely visible in the T2* map. Due to the long readout, we limited our MGRE scan with only 2 echoes in the current study. With the same limited number of echoes, QSM is better to detect the beta-amyloid plaques than T2*. To further explore the regional plaque deposition in the cortex region, we have divided the cortex area into 41 region-of-interests (ROIs). Figure 4 demonstrated the plaque loading in the whole cortex region of different mouse groups (5xFAD, 5xFAD^{M28L}, and 5xFAD^{P522R}). Compared to 5xFAD mice, the plaque loading is higher in the cortex region of 5xFAD^{M28L} (white arrows). The M28L is a risk variant of AD, which may increase the plaque loading. Compared to 5xFAD mice, the plaque loading is slightly lower in the cortex region of 5xFAD^{P522R}, probably because the P522R is a protective variant of AD.

Discussion and Conclusion
Although the cause of AD is not fully understood, clinical and neuropathological studies have hypothesized that the formation of beta-amyloid (Aβ) plaques and tau neurofibrillary tangles are crucial to the pathogenesis of AD. It has been reported that Amyloid plaque is one of the earliest hallmarks of AD and can occur up to 20 years before clinical diagnosis. In this study, we demonstrated that high-resolution QSM can be used to detect the individual beta-amyloid plaque through the whole mouse brain. We also showed that plaque loading is different in AD risk variant (M28L) mice and AD protective variant (P522R), which suggested that QSM may be a sensitive imaging-based biomarker to detect and monitor AD progression and understand the complicated mechanism of AD.

Acknowledgements

This work was supported by NIH R01NS125020, Indiana Center for Diabetes and Metabolic Diseases Pilot and Feasibility Grant, and Roberts Drug Discovery Fund, Stark Neurosciences Research Institute, and the TREAT-AD Center. The authors thank the support from Dr. Yu-Chien Wu, Dr. Adrian Oblak, Dr. Gary Landreth, and Erin Jarvis.

References

1. Hardy JA, Higgins GA. Alzheimer's disease: the amyloid cascade hypothesis. *Science.* 1992;256(5054):184-185.
2. Weimer DL, Sager MA. Early identification and treatment of Alzheimer's disease: social and fiscal outcomes. *Alzheimers Dement.* 2009;5(3):215-226.
3. Li W, Wang N, Yu F, et al. A method for estimating and removing streaking artifacts in quantitative susceptibility mapping. *Neuroimage.* 2015;108:111-122.
4. Gong NJ, Dibb R, Bulk M, van der Weerd L, Liu CL. Imaging beta amyloid aggregation and iron accumulation in Alzheimer's disease using quantitative susceptibility mapping MRI. *Neuroimage.* 2019;191:176-185.
5. Maharjan S, Tsai AP, Lin PB, et al. Age-dependent microstructure alterations in 5xFAD mice by high-resolution diffusion tensor imaging. *Front Neurosci.* 2022;16:964654.
6. Wang N, Zhuang J, Wei HJ, Dibb R, Qi Y, Liu CL. Probing demyelination and remyelination of the cuprizone mouse model using multimodality MRI. *Journal of Magnetic Resonance Imaging.* 2019;50(6):1852-1865.

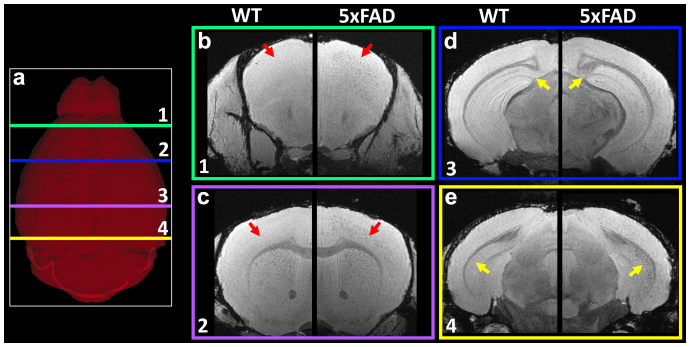

Figure 1. The representative T2*-weighted images of both WT (B6) and AD (5xFAD) mice. Compared to B6, there are hyperintensities areas in 5xFAD mice (red and yellow arrows).

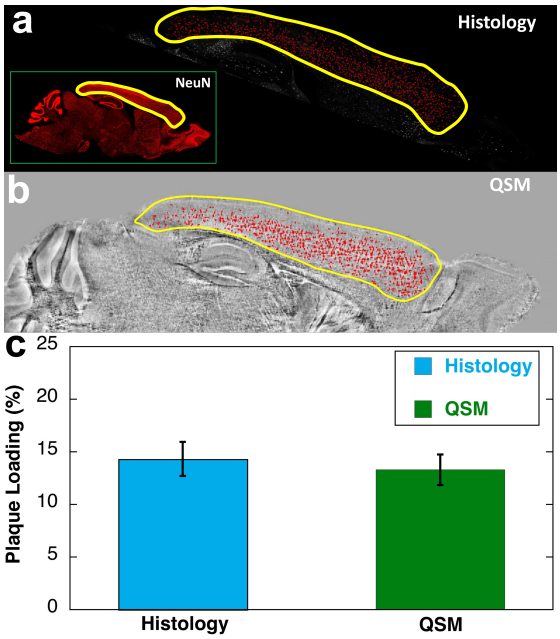

Figure 2. The plaque loading is comparable between QSM and conventional histology.

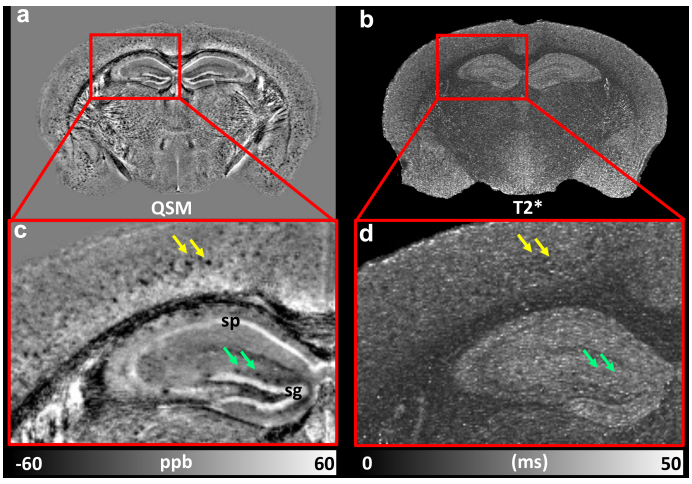

Figure 3. The QSM and T2* map of the 5xFAD mice. The beta-amyloid plaques are better resolved with QSM than T2* in both cortex and hippocampus regions (yellow and green arrows).

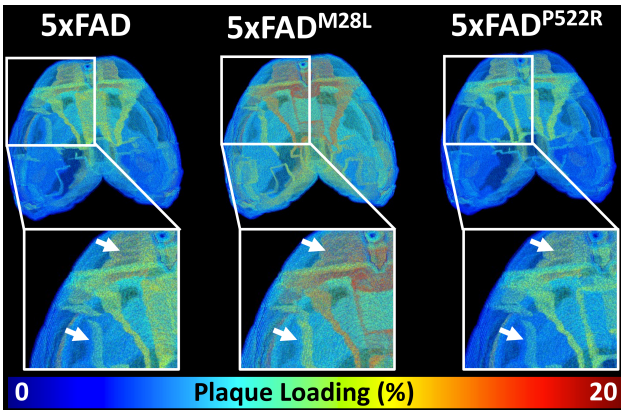

Figure 4. The plaque loading in 5xFAD, 5xFAD^{M28L} (risk variant for AD), and 5xFAD^{P522R} (protective variant for AD). Compared to 5xFAD, the plaque loading is higher in 5xFAD^{M28L} mice; the plaque loading is lower in 5xFAD^{P522R} mice (white arrows).

Direct mass transfer measurement in packed beds via NMR relaxation exchange

S.V. Elgersma[a], *M. D. Mantle*[a], *L. F. Gladden*[a] *A.J. Sederman*[a]
[a]Magnetic Resonance Research Centre, University of Cambridge, UK,

Abstract: We have recently reported a novel method for the direct measurement of the liquid-solid mass transfer coefficient in packed beds using T_2-T_2 relaxation exchange NMR (Elgersma et al. *Chem. Eng. Sci.* 248B **2022**). This method directly probes molecular exchange between intra- and inter-pellet fluid, rather than requiring a net flux between phases as in conventional methods. To extract the mass transfer coefficient from the T_2-T_2 data, a model describing the transport of magnetization in the packed bed during the NMR experiment was developed. Since the NMR method directly probes molecular exchange, this approach enables the quantification of mass transfer in the limit of, and at, zero flow without requiring the use of corrections to account for dispersion or convection effects that complicate measurements of mass transfer when using conventional methods. Mass transfer coefficients measured using the NMR method are compared with literature values and two widely used correlations. As shown in Figure 1, for $Re > 0.2$, the mass transfer coefficients measured using NMR show excellent agreement with the correlations over the flow conditions they were each respectively developed for. At $Re = 0$, the dimensionless mass transfer coefficient determined by NMR is found to approach $Sh = 9$, in good agreement with previously reported numerical, but far greater than that predicted by extrapolating well-known correlations to $Re = 0$. This result is the first direct measurement of the limiting rate of mass transfer in packed beds, and as such aids in resolving the debate in the literature regarding its value. The physics-based transport model developed does not require any calibration or empirical/semi-empirical correction factors, in contrast to many conventional methods used to measure the mass transfer coefficient. The NMR method enables direct measurement of mass transfer coefficients using the real porous pellets employed in industrial processes rather than requiring the use of model analogues.

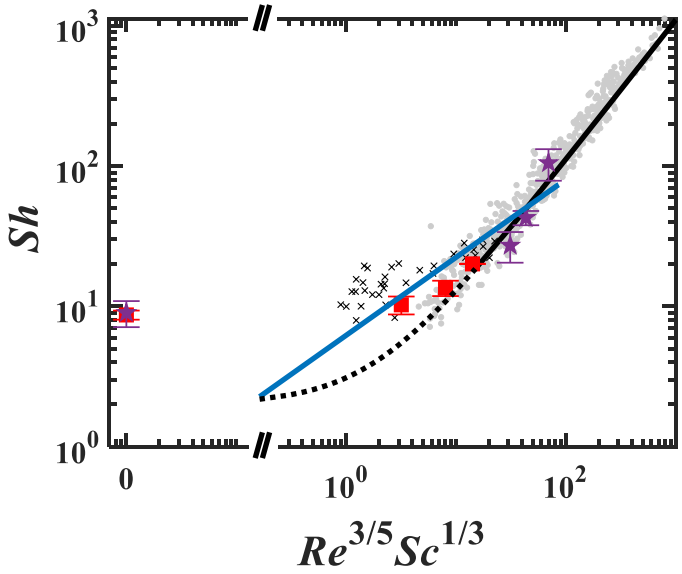

Figure 1. Dimensionless mass transfer coefficients, measured using the NMR method, compared with existing literature data and two selected correlations. Sh is plotted as a function of $Re^{3/5}Sc^{1/3}$ to enable comparison with the survey of dispersion-corrected literature data compiled by Wakao and Funazkri (Wakao and Funazkri, 1978). Data points shown are: (★) NMR 3.1 mm titania spheres, (■) NMR 1.3 mm silica spheres, (×) data from Miyauchi et al.(Miyauchi et al., 1975) , (•) mass transfer data from many sources compiled and corrected for dispersion effects by Wakao and Funazkri (Wakao and Funazkri, 1978), (—) correlation of Wakao and Funazkri, (—) correlation of Wilson and Geankoplis (Wilson and Geankoplis, 1966) evaluated at $Sc = 468$ consistent with the conditions used in the present work. The correlation of Wakao and Funazkri (Wakao and Funazkri, 1978) is shown as a dashed line where it is being extrapolated beyond the flow conditions (lower Re) for which it was developed.

Session 7 – 31AM

Mobile & Low Field

Chair: Velencia Witherspoon, National Institutes of Health

Invited Talk 7

Portable NMR for point-of-care clinical applications: *in vivo*, *ex-vivo* and phantoms

Konstantin I. Momot[1], Dean Greenslade[1], Satcha Foongkajornkiat[1], Nicholas McKay-Parry[2], Tony Blick[3], Tom Lloyd[4], Honor J. Hugo[5], Erik W. Thompson[3]

[1] *School of Chemistry and Physics, Queensland University of Technology (QUT), Brisbane*
[2] *Department of Medical Imaging, Gold Coast University Hospital, Southport, QLD 4215*
[3] *School of Biomedical Sciences, Queensland University of Technology (QUT), Brisbane*
[4] *Department of Radiology, The Princess Alexandra Hospital, Woolloongabba, QLD 4102*
[5] *School of Health and Behavioural Sciences, University of the Sunshine Coast, QLD 4556*

Recent years have seen an increasing interest in the development of biomedical applications of Portable NMR, driven by its portability, mobility and low cost compared to conventional MRI. We have recently reported [1] the results of the first-ever clinical trial of application of Portable NMR for quantification of Mammographic Density, an important breast cancer risk factor and biomarker of the success of failure of certain hormonal anticancer treatments. While this trial has further illustrated the great potential of Portable NMR as a clinical imaging modality, it has also identified the avenues of development required for transforming Portable NMR from an experimental technique into a robust and reliable clinical tool.

From the point of view of MR physics, a major difference between single-sided Portable NMR and conventional MRI is the lack of a true "90º" RF pulse in the former, which is a consequence of the strong permanent magnetic field gradient. This has significant implications for the interpretation of quantitative measurements such as spin-relaxation or diffusion. We will discuss our latest findings concerning the measurement of biological tissue samples *ex vivo* and the implications of the inherent non-ideality of Portable NMR RF pulses for compositional imaging of tissues. We will also discuss our work on the development of phantoms emulating the composition of biological tissues, where the non-ideality of Portable NMR RF pulses has similarly produced some unexpected complications. The results demonstrate that even relatively simple Portable NMR pulse sequences can work in ways that differ from conventional MR. A more detailed understanding of these complexities is a prerequisite for the development of future clinical applications of Portable NMR.

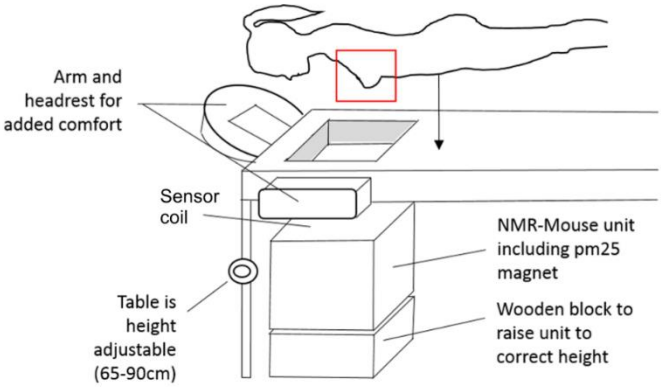

References

[1] N.D. McKay-Parry *et al*, *Magn. Reson. Imaging* **92** (2022) 212-223.

Upscaling simulation of NMR surface relaxation in porous media with Lattice Boltzmann method

C. Liang [a], Z. J. Jia[b], L. Z. Xiao[c]

[a] Changzhou Institute of Technology, Jiangsu Changzhou 213032, China; [b] University of Shanghai for Science and Technology, Shanghai 200093, China;
[c] State Key Laboratory of Petroleum Resources and Prospecting, China University of Petroleum (Beijing), Beijing 102249, China

Nuclear Magnetic Resonance (NMR) technique uses relaxation time to derive characteristic parameters for describing porous media, such as porosity, permeability, and pore size distribution, as well as to observe and analyze the dynamic behavior of fluid molecules. Recently, molecular dynamics (MD) simulation was used to characterize NMR relaxation and diffusion of bulk hydrocarbons as a powerful tool to describe the structure and molecular dynamics of proteins, polymers, crude oil and other macromolecules[1,2]. However, there is yet no available method to use MD results to characterize surface relaxation for porous media. It is crucial to resolve how to upscale MD results to the NMR measurement scale because molecular simulations typically correspond to a very small time step.

This study presents a simulation framework to upscale NMR surface relaxation obtained from MD data using lattice Boltzmann method (LBM). The schematic diagram of the upscaling simulation framework for NMR relaxation at pore surface is shown in Figure 1. Firstly, MD method is used to simulate the motion of water molecules on a silica surface in order to obtain water molecular diffusion coefficient. The surface relaxation can be calculated using Korb's model, in which surface diffusion correlation time(τ_m) and exchange time (τ_s) are defined by water diffusion coefficient[3]. The calculated relaxation time is then scaled up from nanometer-scale to the micron-scale using twice LBM simulations. The micron-scale corresponds to the laboratory measurement scale. Finally, the validity of this proposed method is verified by the analytical solution of the spin-echo decay for a synthetic spherical pores of diameter 5 μm. An application to a stacking model with grain sizes of 200 nm, 1um, 10um and 50um is shown in Figure 2. The T_2 results obtained from the sphere stacking models are in good agreement with the direct LBM simulations and random walk simulations[4]. This method has the advantages of achieving simultaneous multi-scale NMR simulations, and of being able to relate MD results to NMR macroscopic features.

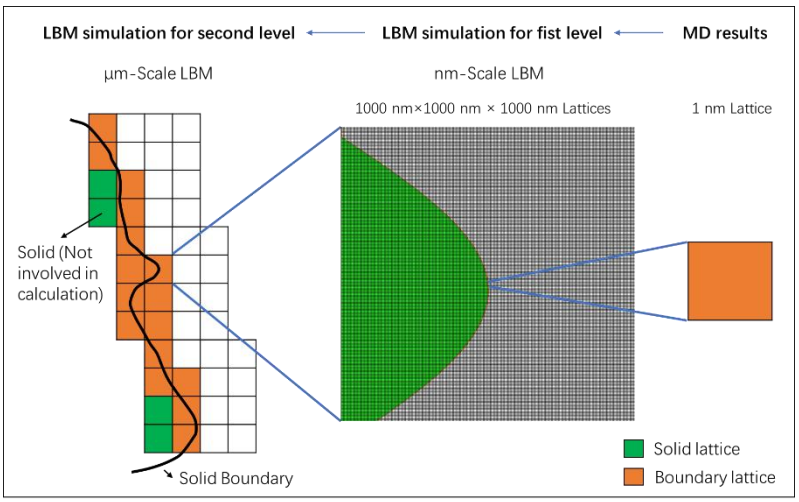

Figure 1 – Schematic diagram of upscaling simulation framework of NMR relaxation in pore surface.

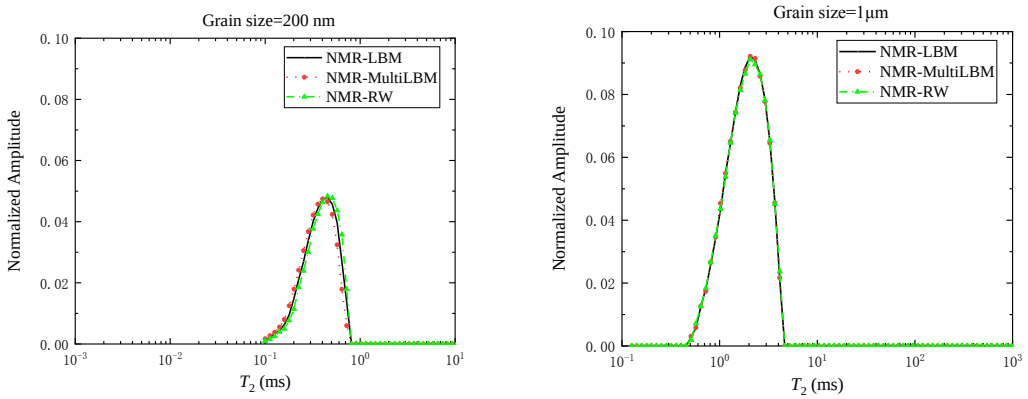

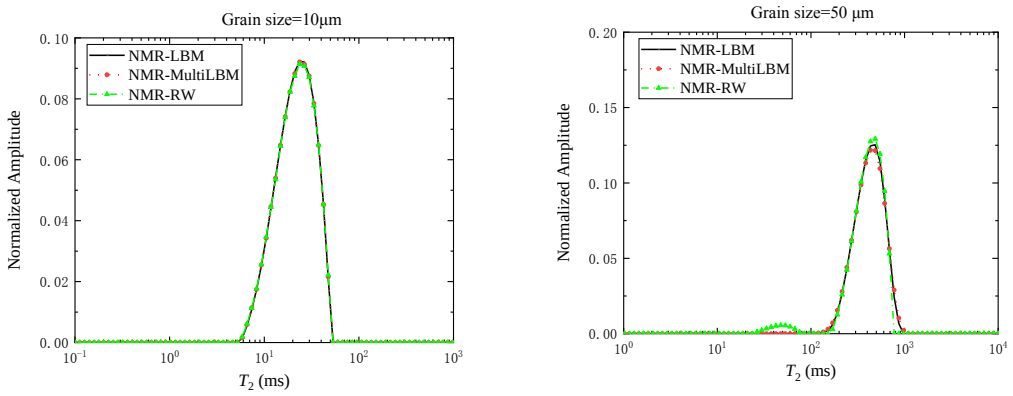

Figure 2 – Comparison of the T_2 transverse relaxation distribution at the micron scale obtained by three simulation methods in a constructed stacking model using (a) 200 nm diameter spheres; (b) 1 μm diameter spheres; (c) 10 μm diameter spheres; (d) 50 μm diameter spheres.

References

[1] Singer P M , Asthagiri D , Chapman W G , et al. Molecular dynamics simulations of NMR relaxation and diffusion of bulk hydrocarbons and water. Journal of Magnetic Resonance, 2017, 277:15-24.
[2] Valiya Parambathu A, Singer PM, Hirasaki GJ, Chapman WG, Asthagiri D. Critical Role of Confinement in the NMR Surface Relaxation and Diffusion of n-Heptane in a Polymer Matrix Revealed by MD Simulations. J Phys Chem B. 2020 May 7;124(18):3801-3810.
[3] Mcdonald P J , Korb J P , Mitchell J , et al. Surface relaxation and chemical exchange in hydrating cement pastes: A two-dimensional NMR relaxation study. Physical Review E Statistical Nonlinear & Soft Matter Physics, 2005, 72(1 Pt 1):011409.
[4] Ivan Rybin, Igor Shikhov, and Christoph H. Arns. Lattice Boltzmann framework for accurate NMR simulation in porous media. Phys. Rev. E 105, 055304.

Characterizing shear properties with portable magnetic resonance – a phase interference technique

W. Selby[1], *I. Mastikhin*[1], *P.* Garland[2]
[1]MRI Centre, Department of Physics, University of New Brunswick, Fredericton
[2]Department of Mechanical Engineering, University of New Brunswick, Fredericton

Introduction: Magnetic resonance elastography (MRE) is a sophisticated technique that uses conventional phase-contrast magnetic resonance imaging (MRI) sequences, synchronized with harmonic sample displacements, to analyze the mechanical properties of tissues and assess their dynamic properties [1]. Our approach utilizes compact and cost-effective portable MR sensors that provide a bulk characterization of dynamic properties in homogeneous regions, close to the surface of the sample. Our previous work has demonstrated that a constant gradient portable MR sensor can be used to obtain relative measurements of viscoelasticity in samples under bulk longitudinal excitation [2]. Building upon this work, we aim to achieve direct measurements of dynamic properties through MR signal modulated by phase interference due to the presence of a velocity distribution.

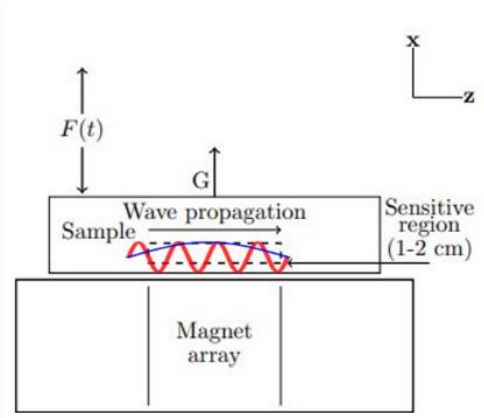

Figure 1 – Use of phase interference in the sensitive volume of a constant gradient MR sensor to encode information on the shear wavelength. A shorter wavelength (red) corresponds to greater phase interference and modulation of MR signal.

Methods: Consider a linear viscoelastic homogenous medium with a plane wave propagating through the MR sensitive region. The displacement (perpendicular to the propagation of the plane wave) is dependent on the shear wave speed and attenuation coefficient which in turn are dependent on the viscoelastic properties of the material.

If the wavelength is comparable to the size of the MR sensor, there will be significant phase interference manifest in changes to the MR signal magnitude and phase. Note that in the case where the sensor size completely covers the wavelength, the signal decay can be described by a zeroth order Bessel function of the first kind. Several parameters can be manipulated to extract information on sample dynamic properties such as echo times, vibration amplitudes, and frequencies.

The sole requirement of the MR instrumentation needed to exploit this phenomenon is a well-defined region of constant gradient in one direction. In these experiments, we employed a unilateral three-magnet array with a constant gradient of 254 G/cm perpendicular to its surface. Preliminary measurements were obtained by exciting the samples with a pneumatic actuator and synchronizing the acquisition of the first echo in a CPMG echo train with the vibration period, repeating for a range of echo times.

Results and discussion:

Several factors complicate a direct measurement of the wavelength for the time being however, an estimate is possible by observing the signal intensity at the first minimum (a complete decay corresponds to complete coverage of the wavelength). The observed frequency dependence suggests that a variable frequency measurement might be naturally suited by this method; however, alternative methods of excitation must also be explored.

Conclusion:

Our preliminary measurements demonstrate the potential of a simple measurement capable of directly measuring the shear wavelength in biological tissues and can already achieve a rough estimate that aligns with expectations. Once we have established robust procedures for characterizing shear properties, we can aim to combine them with conventional MR measurements of relaxation and diffusion, providing an additional layer of information that could potentially be useful in clinical applications.

References: [1] Muthupillai, R. et al., Science 269 (1995). [2] Selby, W. et al., JMR 339 (2022)

Depth-dependent brine transport in salt-rich topsoil monitored by the NMR-MOUSE

S. Stapf, R. Wiebold, K. Lindt, C. Mattea
Dept. of Technical Physics II, TU Ilmenau, 98684 Ilmenau, Germany

Introduction: Water transport within the vadose zone is one of many processes that are affected by anthropogenic activities. Apart from lower groundwater level and varied regional precipitation patterns, agricultural use also alters the retention and storage capacities of natural soils. In many world regions, salinization renders large areas of land unfit for agricultural purposes. Moreover, salt precipitation also affects water transport within the vadose zone and its evaporation by salt crystallization below or above the soil surface. The aim of this study is twofold: to assess the feasibility of monitoring soil drying processes over extended periods of time by means of single-sided NMR, and to provide benchmark tests for the detection of water relaxation and diffusion in iron oxide rich domains that are present on Earth as well as on Mars and other solar system bodies.

Methods: Experiments on water content and T_2 were carried out on Magritek NMR-MOUSE models PM5 and PM10 by placing soil samples of a thickness of 2 mm inside a Petri dish on top of the magnet, and by scanning the fluid properties with spatial resolutions of between 50 and 100 μm. Water and salt solution close to saturation (NaCl and perchlorates) were added to the soil samples up to a supernatant water level of 500 μm, and drying was followed for up to 100 hours or until equilibrium conditions were reached. Additional measurements with defined water contents were carried out for iron-rich Mars simulant soils, and self-diffusion coefficients were obtained by PFG experiments carried out at a Bruker 7.05 T Avance III system equipped with a Diff30 gradient unit.

Results and Discussion: Drying of soil in the presence of NaCl is noticeably slowed down compared to pure water, this can be attributed to the doubling of viscosity at saturated conditions. The dependence of ^{1}H relaxation on salt concentration follows the same trend. In the strong permanent magnetic field gradient of the NMR-MOUSE, the effective T_2 relaxation time first increases upon water evaporation due to the lower diffusion coefficient, before decreasing again as a consequence of reduced soil saturation. For a typical sandy loam soil with an iron content below 1%, paramagnetic transverse relaxation already dominates the diffusion effect [1,2]; Mars soil with up to 18% Fe oxide regularly shows sub-ms relaxation times but remains measureable with the used equipment. Even slower drying was found for $NaClO_4$ and $Mg(ClO_4)_2$, perchlorates which were identified on Mars in regions where liquid water at low temperatures was observed [3]. They are strongly hygroscopic and are soluble at weight fractions of up to 70% at room temperature. While water evaporation in perchlorate-rich soil still follows linear time dependence, dominated by capillary forces as can be expected for a thin soil layer, $NaClO_4$ showed pronounced deliquescence so that a large residual liquid water amount remained even in the presence of dry air stream.

Conclusions: Water evaporation in the presence of large amounts of salt is slowed down considerably but does not change qualitatively when a thin soil column is considered. Formation of macroscopic salt crystals could not be observed visually, suggesting a rather homogeneous distribution of microcrystals. Water bound as hydrate, as is known from perchlorates at the experimental conditions, escapes detection with the used hardware due to its short, solid-like relaxation times. Although total quantitation of water in the presence of either large amounts of salt or iron oxide remains problematic, strong magnetic field gradients of 10-20 T/m allow the direct measurement of self-diffusion coefficients even at temperatures well below 0°C.

References: [1] A. Pohlmeier *et al.*, Vadose Zone J. 8, 735 (2009). [2] S. Haber-Pohlmeier *et al.*, Appl. Magn. Reson. 45, 1099 (2014). [3] L. Ojha *et al.*, Nature Geoscience 8, 829 (2015).

Active EMI Suppression Method for a 50mT Portable MRI Scanner in NICU

Lei Yang[1], *Jiamin Wu*[2,3], *Yucheng He*[2,4], *Zheng Xu*[1]

[1]School of Electrical Engineering, Chongqing University, Chongqing China, [2]Shenzhen Academy of Aerospace Technology, Shenzhen China, [3]School of Mechatronics Engineering, Harbin Institute of Technology, Harbin, China, [4]School of Life Science, Northwestern Polytechnical University, Xi'an, China. (Corresponding author: Zheng Xu, e-mail: xuzheng@cqu.edu.cn)

Introduction: The ultra-low field portable magnetic resonance imaging (ULF pMRI) scanner is cost-effective, lightweight, and fewer safety concern compared to high-field MRI scanners. Recently, it attracted lots of research interests [1]. We proposed an active EMI suppression method [2] that eliminates the need for passive shielding, and enables the scanner to function effectively in an open-shielded complex environment. Our method does not require any additional scan time or modifications to the pulse sequence.

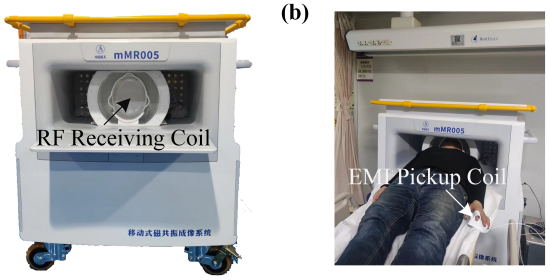

Fig. 1: (a) The home-built 50mT portable MRI scanner. (b) A head scan of healthy volunteer in the NICU of Sanxia Hospital affiliated with Chongqing University.

Methods: The proposed method utilizes EMI pickup coils to detect EMI signals. Specifically, the RF receiving coil samples the contaminated MR signal while the EMI pickup coils synchronously sample the reference EMI signal. Calibration data was obtained by selecting the periphery data of each k-space, and the transfer factors from reference EMI signal to EMI signal in the MR channel were calculated by using LSM in each frequency bands. By using the transferred reference EMI signals, EMI in the MR signal could be suppressed.

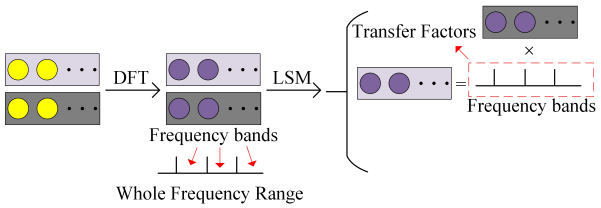

Fig. 2: Diagram of the proposed method.

Results and discussion: The active EMI suppression system was configured to a home-built 50mT portable MRI scanner. A head scan of a healthy volunteer was carried out in the NICU at Sanxia Hospital, affiliated with Chongqing University. GE3D pulse sequence was utilized to obtain T1-weighted images. By utilizing the active EMI suppression system, the signal-to-noise ratio (SNR) was enhanced by 5.4 times, increasing from the initial 2.8 of the original images to 15.3 of the denoised images.

Conclusion: The proposed active EMI suppression system enables the 50mT portable MRI scanner to function efficiently in a complex open-shielding environment. This method uses periphery data for calibration, eliminating the need for additional scan time or modifications to the pulse sequence.

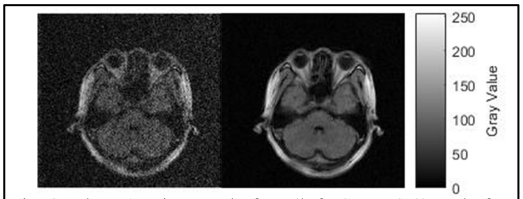

Fig. 3: The T1W images before (left, SNR=2.8) and after (right,SNR=15.3) EMI suppression acquired in the NICU.

References: [1] He et al., Use of 2.1MHz MRI Scanner for Brain Imaging and its Preliminary Results in Stroke, J. Magn. Reson. 319 (2020) 106829.

[2] Yang et al., Active EMI Suppression System for a 50mT Unshielded Portable MRI Scanner, IEEE Trans. Bio-Med. Eng. 69(11): 3415-3426, 2022.

Acknowledgement: This work is supported by NNSFC (52077023) and NNSFCQ (cstc2020jcyj-msxmX0340).

An Rx coil array design for lightweight ultra-low MRI prototype of the breast: proof-of-concept imaging implementation

Zhengxiu Wu[a,b], *SiYu Liu*[a,b], *Xiaowen Jiang*[a,b], *Zhonghua Ni*[a,b], *Hong Yi*[a,b] *Rongsheng Lu*[a,b,*]
[a]Jiangsu Key Laboratory for Design and Manufacture of Micro-Nano Biomedical Instruments, Nanjing, China, [b]School of Mechanical Engineering, Southeast University, Nanjing, China

Breast cancer is the most frequently diagnosed cancer in women. However, limited by the quantity and cost of traditional high-field magnetic resonance imaging (MRI) scanners, breast MRI is not widely available in breast cancer screening. To this end, we construct a truly lightweight ultra-low field (50 mT) and proof-of-concept MRI scanner for the breast MRI (Fig. 1). By simultaneously relaxing the magnet field homogeneity criteria and reducing the uniform area for imaging, i.e. 250 ppm over the Φ300 mm × 50 mm cylindrical volume. A low-impedance receive coil array (Fig. 2a) is designed to be suitable for the vertical B0 field and obtain a high signal-to-noise ratio (SNR), which consists of four 14-cm-diameter loops of Litz wire encircling the FOV on the surface of a 13-cm-diameter cylinder. Geometric decoupling is implemented by overlapping adjacent coils to reduce mutual inductance to only 0.232 nH, hence near zero interaction between adjacent coils. The interaction between the Tx coil and Rx coil is eliminated by adding the PIN diode detuning to the tuning matching circuit of the Rx coil. The array performance is validated with the experimental image of 2D test phantom. The preliminary axial image of the 3D printed "SEU/MRI" phantom is shown in Fig. 2b. The 3D printed resin phantom is 2.0-cm thick with a 12-cm diameter, and is filled with $CuSO_4$-doped water. Sixty-four averages of an eight spin-echo train (TR = 1000 ms, echo-spacing = 15 ms) were acquired within 8.5 min. The upper part of the "E" and the lower part of the "R" on the image are not very clear. In fact, the maximum distance between the "E" and "R" is more than 10 cm, while the average height of the breast axis is around 5.5 cm in women. Therefore, the designed Rx array coil, used with the lightweight ultra-low field MRI system, shows convincing proof of concept images, that are expected to be further improved and used in breast cancer screening in the future.

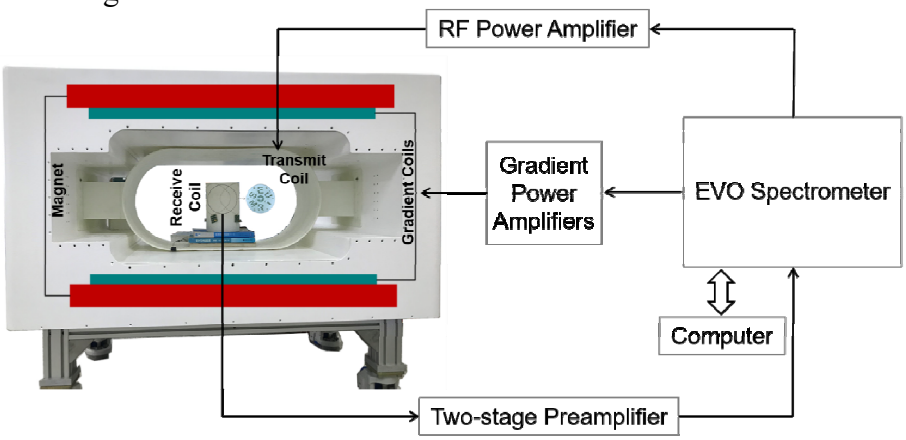

Fig. 1: The schematic diagram of lightweight ultra-low MRI prototype for the breast.

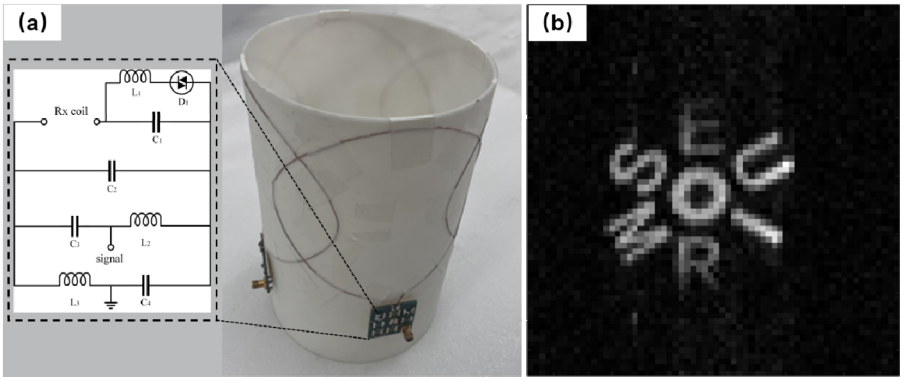

Fig. 2: (a) Photo of the four-channel receiver array coil. The tuning matching circuit with PIN diode detuning circuit is displayed enlarged. (b) Experimental 64 x 64 voxel, 20-cm FOV axial image of a 3D printed phantom with $CuSO_4$-doped water occupying the interior of the letters and resin surrounding it.

References: [1] Roemer P B, Magn. Reson. Med. (1990).

NMR Depth Profiling of Painted Walls: Ostia Antica

Matea Urbanek,[1] Jan Bader,[2] Daniel Krüger,[2] A. Yong,[3]
Jürgen Frick,[1] Jens Anders,[2] E. Del Federico,[3] P. Tomassini,[4] Bernhard Blümich[5]
[1] Materialprüfungsanstalt Stuttgart, [2] University of Stuttgart, [3] Pratt Institute Brooklyn,
[4] UC Louvain, [5] RWTH Aachen University

The mortar-layer stratigraphy of Roman wall paintings at Ostia Antica, the historic port of ancient Rome, was studied at two occasions with nuclear magnetic resonance (NMR) depth profiling [1] to explore manufacturing details in the context of the use and history of the buildings. In the first campaign in 2019 the NMR signature of covered wall paintings was studied [2,3], while in the second campaign in 2022, depth profiles were compared to answer the question if different painted walls were prepared for painting at the same time or by the same workshop [4]. The experience gained in handling the portable NMR hardware for onsite measurements has stimulated the development of an improved NMR depth-profiling instrument [5,6]. The information provided by NMR depth profiling is illustrated with experimental data, and progress in hardware development is reported.

[1] B. Blümich, Concepts and Applications of the NMR-MOUSE, in: D.M. Bastidas, E. Cano, eds., *Advanced Characterization Techniques, Diagnostic Tools and Evaluation Methods in Heritage Science*, **Springer Nature**, Cham, 2018, 61-75
[2] B. Blümich, E. Del Federico, D. Jaschtschuk, M. Küppers, K. Fallon, A. Steinfeld, P. Tomassini, *Nondestructive Analysis of Wall Paintings at Ostia Antica*, **Heritage 4** (2021) 4421–44
[3] B. Blümich, D. Jaschtschuk, C. Rehorn, *Advances and Adventures with Mobile NMR*, in: S. Haber-Pohlmeier, B. Blümich, L. Ciobanu, *Magnetic Resonance Microscopy*, **Wiley-VCH**, Weinheim, 2022, chapter 7, pp. 155-172
[4] M. Urbanek, S. Haber-Pohlmeier, D. Krüger, J. Bader, E. Del Federico, K. Fallon, A. Steinfeld, J. Zöldföldi, J. Frick, J. Anders, H. Becker, B. Blümich, P. Tomassini, *Lessons on the history of buildings from NMR depth profiles of painted walls at Ostia Antica*, manuscript in preparation
[5] B. Blümich, J. Anders, *When the MOUSE leaves the house*, **Magn. Reson. 2** (2021) 149–160
[6] Supported by DFG grant DFG AN 984/24-1 and FR 2912/2-1

Session 8 – 31PM

Engineering & Materials

Chair: Andrew Sederman, University of Cambridge

MRI for chemical engineering: Case studies in granular flow and porous media

D. Clarke[1]
[1]Victoria University of Wellington, Wellington, New Zealand,

Introduction: MRI is a useful technique for informing the design of process devices because it can non-invasively visualise opaque 3D systems and is sensitive to pertinent quantities such as velocity distribution, volume fraction, and temperature. This talk will explore the application of flow MRI to two chemical engineering applications: (1) characterising granular rheology, and (2) studying flow in novel 3D-printed triply periodic minimal surface (TPMS) porous structures.

Methods: Experiments were performed using a 9.4 T (400 MHz) Bruker magnet, Avance I spectrometer, and a micro2.5 gradient set. To study granular rheology, a rheo-NMR drive system was used to measure flow of plant seeds under annular shear [1]. TPMS columns were made using stereolithography and were incorporated into a water flow loop. Single-point imaging was used for granular packing fraction and velocity mapping turbulent TPMS flows. Spin-echo/gradient-echo were used for velocity imaging in slower-moving systems. Single-shot spiral imaging [2] was used for velocity mapping with 10 ms time resolution.

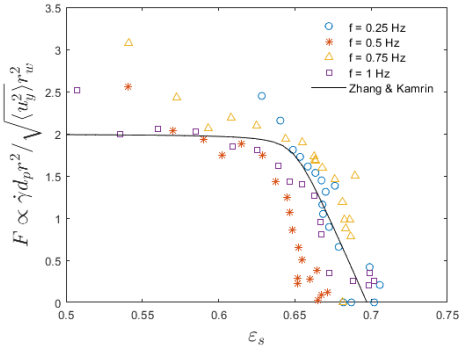

Fig. 1: Dimensionless granular fluidity, *F*, versus solid volume fraction, ε_s. Markers indicate MRI data. Solid line is empirical relation.

Results and discussion: MRI data for shear rate, variance of velocity fluctuations, and volume fraction were used to test the microscale definition for granular fluidity (Fig. 1). These data confirmed the trend predicted by discrete element simulations [3], which may improve the accuracy of continuum-scale granular flow modelling. Processing simulation outputs for appropriate comparison against MRI data was also explored [4].

3D gradient-echo flow images were used to produce a streamline plot for flow through the Schwarz Diamond TPMS (Fig. 2). Flow was distributed equally between the pores, in contrast to channelling in random porous media [5]. The flow became unsteady at a Reynolds number around 150 [6]. At higher Reynolds numbers, the *x* and *y* velocity variance were inversely correlated.

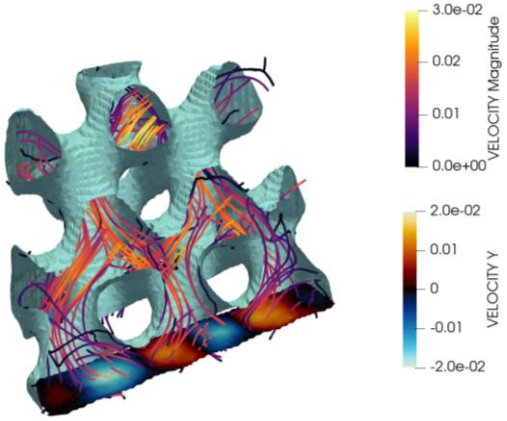

Fig. 2: Streamline plot of inertial flow (Re = 50) through a Schwarz Diamond TPMS. Velocity scales are in m s^{-1}.

Conclusion: Flow MRI provides detailed insights into systems relevant to chemical engineering. It is well-suited for probing granular rheology because it is capable of measuring many of the quantities necessary for model validation. Non-invasive 3D measurements provide unparalleled insight into the complex flow patterns within novel channel geometries that may enhance heat and mass transfer performance.

References: [1] Fabich, Phys. Rev. E (2018).
[2] Tayler, J. Magn. Reson. (2011).
[3] Zhang, Phys. Rev. Lett. (2017).
[4] Clarke, J. Magn. Reson. (2019)
[5] Clarke, Chem. Eng. Sci. (2021).
[6] Clarke, AIChE J. (2023).

MR Imaging and Kinetic Monte Carlo Simulation of Lithium Dendrite Growth

Rok Peklar[1], *Urška Mikac*[1], *Igor Serša*[1]
[1]Jožef Stefan Institute, Ljubljana, Slovenia

Introduction: Modern lithium-ion batteries have revolutionized the way we use portable electronic devices, electric vehicles, and even renewable energy storage. However, the energy density of lithium-ion batteries is still relatively low compared to lithium metal batteries. Lithium metal batteries are capable of providing much higher energy densities, making them an ideal candidate for next-generation energy storage solutions, but their development is hindered by dendrite growth. Dendrites are needle-like microstructures that form on the anode during the recharging process, leading to decreased battery capacity and potential safety hazards [1]. By controlling the dendrite growth, lithium-metal batteries could provide much higher energy densities, benefiting transportation, energy storage, and promoting a cleaner future.

Methods: A kinetic Monte Carlo model was developed to simulate microscale lithium dendrite growth, incorporating Li+ electromigration and diffusion in nonuniform electric fields that vary over time. Simulation results were compared to macroscale images obtained by magnetic resonance imaging (Fig. 1) to establish a link between dendrite structural features at various scales.

Results and Discussion: To our knowledge, there is no previous analysis examining the potential link between dendrite structural characteristics at various scales. By developing the kinetic Monte Carlo model and comparing simulation results to macroscale images, this research can help understanding a connection between micro and macroscale structural features of dendrites. Understanding the scaling of structural characteristics is critical for efficiently predicting the safety of lithium batteries and controlling dendrite growth in lithium-metal batteries. The knowledge gained from this research could be used to develop safer batteries with reduced or better predictable growth of dendrites using computationally inexpensive simulations.

Fig. 1: MRI Slice of dendritic growth in a battery cell.

Conclusion: Understanding how the mechanics of electromigration and diffusion affect dendrite growth and how nanoscale structural patterns translate into larger scales is a key step toward designing dendrite-free lithium-metal batteries. The development of a kinetic Monte Carlo model that simulates microscale lithium dendrite growth and establishes a connection between structural features at various scales could be a critical step towards mitigating dendrite growth and developing safer lithium-metal batteries.

References: [1] Grey et al., Chem. Mater. (2016).

Evaluation of mixing efficiency in bubble reactors for carbon dioxide capture using MRI

Feryal Guerroudj, Emmanouela Leventaki, Saeed Khoshhal Salestan, Francisco M. Baena-Moreno, Diana Bernin

Department of Chemistry and Chemical Engineering, Chalmers University of Technology, Gothenburg, Sweden

Introduction:

CO_2 absorption is a potential and temporary solution to hamper further climate changes. Alcohols combined with sodium hydroxide are capable of absorbing CO_2 and might be a promising alternative to amines. There are many designs of bubble reactors to capture CO_2 efficiently, which depends heavily on the mixing of the liquid and the gas. Here we evaluated the mixing efficiency of our 3D-printed bubble reactor without forced mixing over time using fast MRI techniques.

Methods:

Solutions were prepared with 96% ethanol, 4% water and NaOH at concentrations of 2-10 g/L. The gas was a mixture of 30% CO_2 and 70% N_2. The experiments were conducted in a 3D-printed bubble column reactor at ambient pressure and temperature. The reactor was placed inside an MRI (Bruker Avance III 300MHz with a ^1H transmit/receive probe of 66 mm diameter) and the gas was sparged continuously into the reactor. One-shot RARE images and flow maps were recorded throughout the reaction.

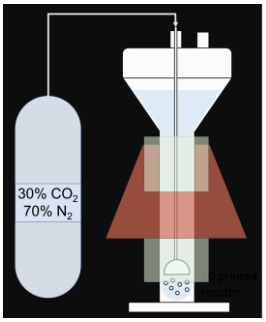

Fig. 1: Experimental setup.

Results and discussion:

During CO_2 absorption, a gel is formed containing most likely a mixture of inorganic and organic carbonates. This gelation hinders further absorption as it inhibits good mixing and further dissolution of CO_2. We found that our 3D-printed bubble reactor had a slightly lower performance on CO_2 capture absorption compared to stirred ones. One-shot multi-slice RARE images (Figure 2) enabled monitoring the increase in viscosity of the whole reactor. High signal intensity (bright yellow) corresponds to the liquid, while low intensity corresponds to regions where the gas is creating turbulence. Good mixing regions could be identified based on the intensity of the signal. For the 2 g/L NaOH solution, better mixing was observed due to less gel formation. We also found that the positioning of the sparger is crucial to minimize regions with bad mixing.

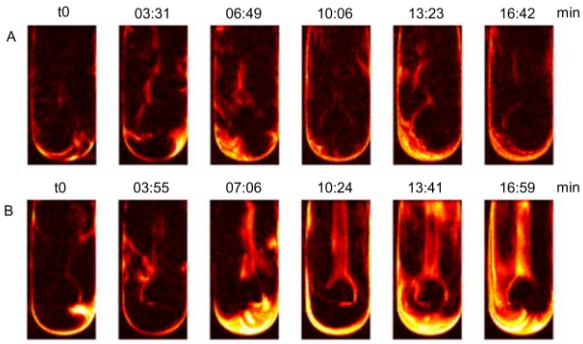

Fig. 2: Examples of sagittal one-shot RARE images over time during sparging gas into a solution of (A) 2 g/L of NaOH in ethanol and (B) 10 g/L of NaOH in ethanol.

Conclusion:

MRI provided an understanding of the fluid dynamics inside a bubble column. In cases where the liquid phase is opaque, or physicochemical changes affect the process, conventional methods like high-speed cameras tend to fail. Fast MRI combined with a solution forming a gel upon reaction enables to optimize bubble reactor designs. Next steps are to evaluate stirred bubble reactors with MRI.

References: [1] Tayler, Doctoral thesis (2011). [2] Baena-Moreno, Heliyon (2023)

Toroidal and Poloidal Vortex Rotation of Halbach Rings for Determining the Spatial Distribution of Magnetic Nanoparticles – initial results

P. Vogel [a], *L. Mirzojan* [a], *M.A. Rückert* [a], *J. Günther* [a], *T. Reichl* [a], *T. Kampf* [b], *V.C. Behr* [a]
[a] Experimental Physics 5 (Biophysics) University of Würzburg, Germany
[b] Diagnostic and Interventional Neuroradiology, University Hospital Würzburg, Germany

Introduction: Magnetic Particle Imaging (MPI) directly visualize the distribution of magnetic nanoparticles (MNPs) in 3D [1]. The nonlinear magnetization response of MNPs to time-varying magnetic fields and strong magnetic field gradients exhibiting a field free point (FFP) or a field free line (FFL) allows scanning a desired field of view voxel-by-voxel. Most MPI scanner use electrical coils to generate of fast-moving gradient fields [2], which causes high power dissipation. Permanent magnet configurations like Halbach rings [3] can be used to generate strong and homogeneous magnetic fields without the need for electrical power [6]. Furthermore, asynchronous axial rotation of nested Halbach rings with different configurations (Fig. 1) is possible without strong magnetic forces between the magnets [7]. The required field gradients of MPI scanners cause difficulties when using Halbach rings [4,5]. In this work we demonstrate an experimental proof-of-concept MPI scanner using mechanically rotating Halbach rings [8].

Methods: The assembling of two *k*=0 and two *k*=1 Halbach rings where the *k*=0 rings can be rotated poloidally (about the local x-axis of each magnet) and the *k*=1 can be rotated toroidally (about the rings z-axis), two FFPs can be generated and moved through the desired FOV (Fig. 1). Halbach arrays are known for strong magnetic interactions between the composing magnets making it difficult to build such systems, even more so for rotatable arrays. This issue was investigated by simulating the forces and torques occurring in the system using a home-built software [9].

Results and discussion: Fig. 1 show the first fully 3D printed mechanical MPI prototype, which is driven by 4 stepper motors generating an FFP with a gradient strength of 0.4 T/m. The acquisition time for a full image depends on the number of voxels and is in the range of several minutes.

Conclusion: A fully mechanically driven Traveling Wave MPI scanner approach covering a full 3D volume is presented. Building the MPI systems strong spatial encoding gradients from permanent magnets reduces the power consumption drastically paving the way for portable MPI systems.

References: [1] Gleich, Nature (2005), [2] Knopp, Phys Med Biol (2017), [3] Halbach, Nucl Instr Meth Phys (1980), [4] Bagheri, Appl Phys Lett (2018), [5] Vogel, Sci Rep (2019), [6] Raich & Blümler, Conc Magn Reson B (2004), [7] Vitor, Rheologica Acta (2011), [8] Mirzojan, IJMPI (2022), [9] Vogel, arXiv (2022)

Funding: This work was partially funded by the DFG (BE 5293/1-2, VO 2288/1-1, VO 2288/3-1)

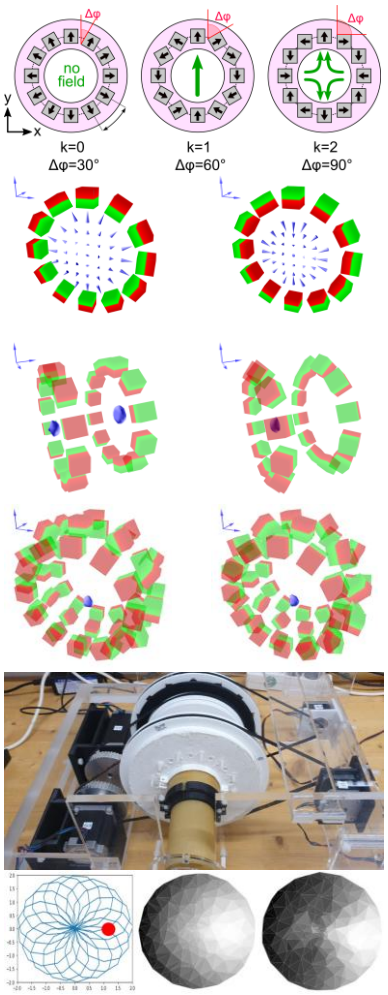

Fig. 1: 1st row: Halbach rings consist of permanent magnets assembled as a ring with a specific angle generating different magnetic field configurations. **2nd row:** two Halbach rings (*k*=0) with different poloidal rotation angle. **3rd row:** Both rings at a fixed distance and under continuous synchronous vortex rotation generate two field free points (blue) traveling along the symmetry axis. **4th row:** Using additional Halbach rings (*k*=1) assembled in the center and counter-rotating at different frequencies move the FFP along a rose trajectory through the FOV. **5th row:** Image of the first mechanical MPI prototype. **6th row:** simulated (middle) and measured (right) point sample.

Low field NMR probe of microstructural and mechanical strength evolution of cemented paste backfill prepared using varying salinity water

Razyq Nasharuddin[1], Neil Robinson[1], Andy Fourie[2], Michael L. Johns[1], Einar O. Fridjonsson[1]
[1] Department of Chemical Engineering, The University of Western Australia, Perth, Australia,
[2]Department of Civil, Environmental and Mining Engineering, The University of Western Australia, Perth, Australia

Introduction: Annually, vast volumes of mine wastes known as tailings are generated, with tailings-to-product volume ratio of 100:1 is common and in extreme cases 1,000,000:1 [1]. Given the dwindling quality of orebodies worldwide, this ratio may be expected to gradually increase over time. Cemented paste backfill (CPB) is a technology applied globally that transforms tailings from waste into a potential resource by safely depositing these slurries into underground mine openings in the presence of binders [2,3]. However, greater understanding of how variations in water salinity affect microstructural development and mechanical properties of CPB is needed before this technology can be more widely adopted within the mining industry.

Methods: Here, we applied low-field ^{1}H nuclear magnetic resonance (NMR) relaxometry measurements (T_1 and T_2) to monitor the microstructural evolution of CPB materials hydrated over 56 days with tap or hypersaline water. Furthermore, we conducted uniaxial compressive strength (UCS) tests to develop a predictive correlation between the mechanical strength and T_1 and T_2 measurements [3]. We also used UCS measurements to observe the effects of water salinity dilution on CPB strength development as the CPB hydrates. To probe the source of mechanical strength variations, scanning electron microscopy and energy dispersive X-ray spectroscopy (SEM-EDX) were utilised to observe surface topography and identify the types of hydration products formed.

Results and discussion: Monitoring NMR relaxation times associated with water confined within capillary pores of the CPB samples provides a non-invasive route with which to quantify and compare hydration rates. We demonstrated that the use of hypersaline water delays the CPB capillary pore structure evolution rates, relative to tap water, thus resulting in comparatively weaker CPB structures when hypersaline water is used [4]. Furthermore, we report elevated strengthening of mechanical properties at significantly reduced hydration times for diluted hypersaline water compared with both hypersaline and tap water, thereby prompting further investigation of the underlying mechanisms for these observed enhancements [5]. The morphological characteristics observed *via* SEM-EDX show the importance of both calcium silicate hydrates and ettringite in enhancing the strength development of CPB.

Conclusion: This study demonstrated CPB strength development across various water formulations. It elucidated the importance of specific hydrated crystalline products (e.g. ettringite) in increasing the rate of strengthening of CPB. The results presented have important implications on the mass adoption of CPB technology using hypersaline water within the mining industry. In particular, the potential benefits of utilising diluted hypersaline water to enhance the rate of CPB material strengthening. This may result in improvements to the scheduling of mine site operations (e.g. blasting). As well as reduction in binder content due to higher observed uniaxial compressive strength of the diluted hypersaline water CPB samples compared to tap and hypersaline water CPB samples.

References: [1] Dudeney et al., International Journal of Mining, Reclamation and Environment (2013) **27**; [2] Qi and Fourie, Minerals Engineering (2019) **144**; [3] Behera et al. Construction and Building Materials (2021) **309**; [4] Nasharuddin et al. Cement and Concrete Research (2021) **147**; [5] Nasharuddin et al. Construction and Building Materials (2022) **347**.

Session 9 – 31PM

Biomedical II

Chair: Weng Kung Peng, Songshan Lake Materials Lab.

Invited Talk 9

Clinical applications of exercise stress-induced cardiac magnetic resonance imaging

Le Thu Thao
National Heart Research Institute Singapore, National Heart Centre Singapore
Cardiovascular Sciences Academic Clinical Programme, Duke-NUS Medical School

Introduction: Exercise stress test is more physiological in replicating the symptoms and haemodynamic changes compared to pharmacological stress, with less adverse events and better tolerated. The clinical applications of exercise stress cardiac magnetic resonance (ExCMR) imaging were explored.
Methods: In-scanner supine ergometer (Lode, Netherlands) ExCMR imaging protocols (1.5T Aera, Siemens Healthineers) were developed for different applications: 1) to differentiate between athlete's heart and early cardiomyopathy [1]; and 2) to diagnose significant coronary artery disease in patients with chest pain [2].
Results and discussion: Despite technical challenges due to excessive motion during exercise that affects ECG triggering and image quality, the test performances were accurate as compared with invasive coronary haemodynamic measurement (fractional flow reserve – FFR) in patients with suspected chest pain and cardiopulmonary stress test in patients with suspected athlete's heart.
Conclusion: ExCMR has shown to be an excellent stress test to be deployed to cardiac clinical services.
References:
[1] Le et al., J Cardiovasc Magn Reson (2020)
[2] Le et al., J Cardiovasc Magn Reson (2021)

Figure. Set up of CMR-compatible supine ergometer in scanner.

3D-printed micro-anisotropic, macro-isotropic, susceptibility-matched diffusion phantoms

Velencia J. Witherspoon[1], *Michal Komlosh*[1,2], *Dan Benjamini*[1,2,3], *Evren Özarslan*[4,5], *Nickolay Lavrik*[6], *Peter Basser*[1,2]

[1]Eunice Kennedy Shriver National Institutes of Child Health and Human Development, NIH, MD, USA. [2] Center for Neuroscience and Regenerative Medicine, Uniformed Services of Health Sciences, MD, USA. [3]Multiscale Imaging and Integrative Biophysics Unit, National Institute on Aging, NIH, MD, USA. [4]Department of Biomedical Engineering, Linköping University, Linköping, Sweden. [5]Spin Nord AB, Linköping, Sweden. [6]The Center for Nanophase Materials Sciences at Oak Ridge National Laboratory, TN, USA.

Introduction: Diffusion MRI methods are commonly employed to infer pathology-induced changes in tissue microstructure from quantities like the mean apparent diffusion coefficient (*mADC*), fractional anisotropy (*FA*), effective pore size, shape, and connectivity. There is a tendency to transition new methods from theory to tissue-applications without vetting due, in part, to a limited selection of MRI phantoms that offer portability, reproducibility, and result in artifact-free images. We present the design and fabrication of 3D-printed susceptibility-matched phantoms whose uniform capillary arrays provide anisotropic environments that can be aligned or randomly oriented.

Methods: The Nanoscribe, GmbH was used to finely tune the microstructure of highly reproducible solid-walled capillary array blocks (Fig1 D,E). The susceptibility was tested using echo planar imaging (EPI) and point resolved spectroscopy registered to the orientation of the individual blocks established by diffusion tensor imaging (DTI) experiments. Double pulse field gradient spin echo experiments were performed on the aligned and randomly oriented blocks.

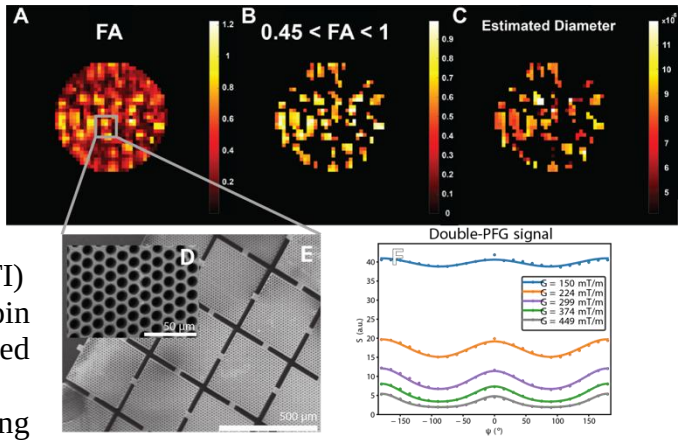

Figure 1 Heat maps of randomly oriented phantom with 100 µm^3 of FA (A), thresholded FA > 0.45 (B), and the CHARMED estimated diameter (C). Scanning electron microscopy images (D,E) showing the ground truth diameter and print uniformity. The resulting fit new semi analytical model and data.

Results and Discussion: Our phantom featuring ~11µm capillary arrays exhibited high *FA* (Fig1 A,B). The susceptibility-matched behavior of the phantom was confirmed via EPI measurements with varied number of segments. We employed two mathematical models for analyzing the diffusion MRI data: a modified composite hindered and restricted model of diffusion (CHARMED) and a newly developed analytical model for randomly-oriented fibers used to estimate the capillary diameter (Fig 1C) and angle (ψ) dependency for double PFG experiments (see Eq. 1, Fig 1F). Both models underestimated the ground truth diameter when dealing with random orientation within a single voxel, although the analytical model achieved a slightly better estimate when a bound population was considered during the fitting procedure.

Conclusion: We developed a microcapillary phantom and verified that its susceptibility matched that of water. We studied its macroscopic as well as microscopic anisotropy via single- and double-PFG measurements. A novel semi analytical framework to estimate the diameter of the capillaries was developed, which yielded high quality fits to data from randomly oriented capillaries. Our phantom enables us to vet and support the development of diffusion methods for providing a quantitative description of tissue microstructure within a voxel.

References: [1]Komlosh et al. J Magn Reson. 208(1) (2011):128-135.[2] Benjamini et al. J Magn Reson. 246 (2014):36-45 [3] Assaf Y et al. Neuroimage. 27(1) (2005) : 48-58 [4] Komlosh et al. J Magn Reson. 275 (2017):19-28.

Towards replacing 2D Inverse Laplace Transforms with Deep Neural Networks for processing Diffusion Exchange Spectroscopy data

Xiaoning Ma[1], Zicheng Zhao[1], Jiahe Qu[1], Bernard Siow[1,2]

[1] UCL Centre for Advanced Biomedical Imaging, U.K. [2] The Francis Crick Institute, London, U.K.

Introduction: Cell membrane permeability is abnormal in many pathologies such as in tumours and neurodegenerative diseases. Diffusion Exchange Spectroscopy (DEXSY) [1], has been used to detect microstructural changes of cell membrane permeability in mammalian tissue [2,3]. Imaging scans typically contain 10^5-10^6 voxels and processing each voxel with a 2D Inverse Laplace Transform (ILT) is laborious and prone to operator biases. DEXSY datasets have previously been reparametrized to avoid the use of 2D-ILTs [4]. Here, we test the feasibility of using Deep Neural Networks (DNN) to learn mapping between parameters of the forward model (volume fractions, diffusivities, permeability) and the Diffusion Exchange Index (DEI) [3], with the aim of fast and robust processing of DEXSY data, particularly in clinical scenarios.

Method: DEXSY signals were simulated, using equations in [1], over a range of biologically relevant permeabilities (1.0-1.8 µm/s) in a two-compartment model (diffusivities 0-2.5 $\mu m^2/s$, 0.5 volume fraction, SNR =10-50) over a total of 10000 simulations (7:2:1 train:test:validation ratio). A DNN was applied in order to learn the features of the simulated signal dataset, predicting the 2D diffusion spectrum. The DNN was validated using an independent set of simulations and DEI were then calculated from the predicted 2D diffusion spectrum (DEI_{DNN}). This was compared with the ground truth DEI calculated from the parameters of the simulation (DEI_{GT}). Also, ILTs [5] were used to process a subset of simulated signals and the DEI were subsequently calculated (DEI_{ILT}).

Results: Figure 1 shows Bland-Altman plots over DEI 0.1 to 1.3 with no noise and SNR=40, demonstrating a good correlation between DEI_{GT} and DEI_{DNN}. At SNR=40, the mean error of DEI_{DNN} and DEI_{ILT} were -0.01 and 0.06 respectively. For large DEXSY datasets (e.g. 100^2 measurements), DNN processing was significantly faster than using ILTs (seconds vs hours).

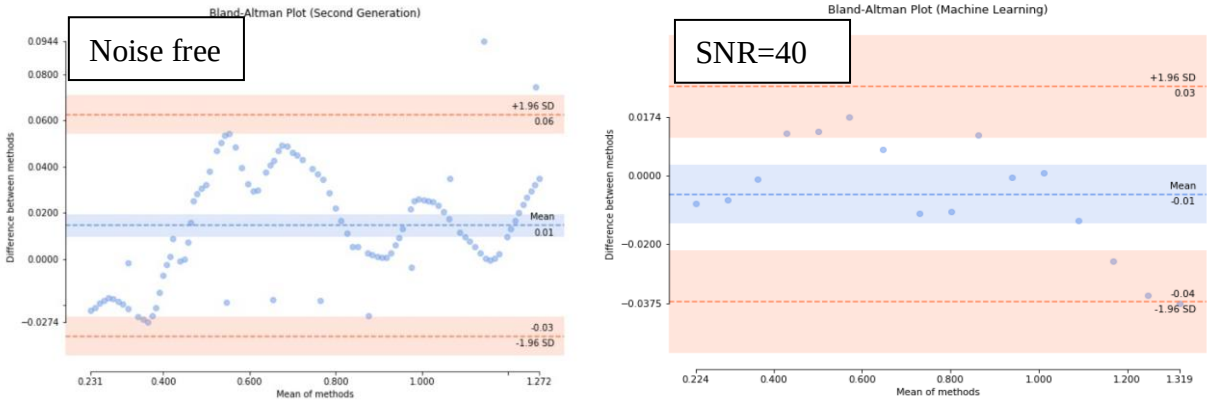

Figure 1: Bland-Altman plots comparing DEI_{DNN} with DEI_{GT} with no noise and at SNR=40

Conclusion: Our findings suggest that machine learning techniques can, in principle, be used as an alternative option to the 2D-ILT to quantify DEI for a two-compartment model. This would represent a leap in the processing speed of DEXSY signals and could lead to the practical use of DEXSY in clinical imaging scenarios to produce maps of cell membrane permeability.

References: **[1]** Galvosas P et al. (2007) *Magn Reson Imaging*, 25(4), pp.497–500 **[2]** Siow B et al. (2013) *Proc 12th ICMRM* **[3]** Breen-Norris J et al. (2020) *Magn Reson Med*, 84(3), pp.1543-1551. **[4]** Cai TX et al. (2018) *J Magn Reson*, 297, pp.17–22. **[5]** Godefroy S, Ryland B and Callaghan PT. (2008) 2D LAPLACE INVERSION, Victoria University of Wellington, NZ. Kindly provided by Petrik Galvosas.

Tract-specific Microstructural Alterations in Intermittent exotropia identified by Fiber Quantification and Effect Size Analysis

Leqing Zhou[1], *Jianlin Guo*[2], *Yun Peng*, *Fangrong Zong*[1,*]

[1] School of Artificial Intelligence, Beijing University of Posts and Telecommunications, Beijing, China; [2] Department of Radiology, Beijing Children's Hospital, Capital Medical University, National Center for Children's Health, Beijing, China; *Corresponding author

Introduction: Intermittent exotropia (IXT), a condition characterized by intermittent outward deviation of the eyes, is estimated to have a prevalence of 1% in the population [1]. Sporadic studies have examined the profile of cerebral white matter, yet their findings are inconsistent [2][3]. This inconsistency may be ascribed to partial volume effects, which often impact voxel-based Diffusion Tensor Imaging (DTI) analysis. The Automated Fiber Quantification (AFQ) method, designed to quantify microstructural properties along fiber bundles has the potential to circumvent these effects [4]. Several studies have successfully employed AFQ to analyze other brain disorders and obtain favorable results. This study aimed to investigate the characteristics of brain microstructure in IXT patients using AFQ.

Method: Twenty-five patients with IXT as well as twenty-five healthy participants matched for age and gender underwent the DTI scanning (32 diffusion gradient directions; b=1000s/mm^2) and the ophthalmic examination. AFQ analysis of 20 major fiber tracts was carried out for IXT patients and healthy subjects, respectively. The processing includes six steps as showed in Figure1. Diffusion metrics of 100 equidistant nodes resampled along each tract were measured for every subject and compared between two groups. Effect size analysis was further performed to identify the most affected fiber tracts in IXT.

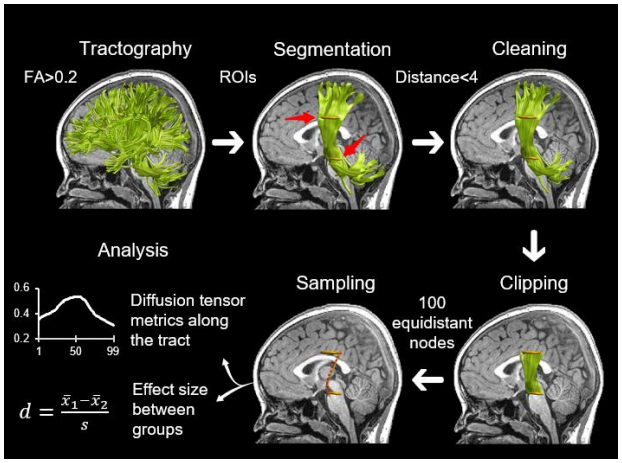

Fig. 1: Process of Fiber Quantification and Effect Size Analysis, taking the corticospinal tract as an example.

Results and discussion: Significant reduction in mean diffusivity (MD) was observed in IXT along the major tracts, particularly the bilateral thalamic radiations (Figure 2). Interference of synapse pruning and reduced axons collaterals is likely to account for these findings, and possibly results in weaken communication among neurons in IXT. Through the effect size analysis, the most affected fiber tract is found to be the left thalamic radiation, while right inferior longitudinal fasciculus in FA.

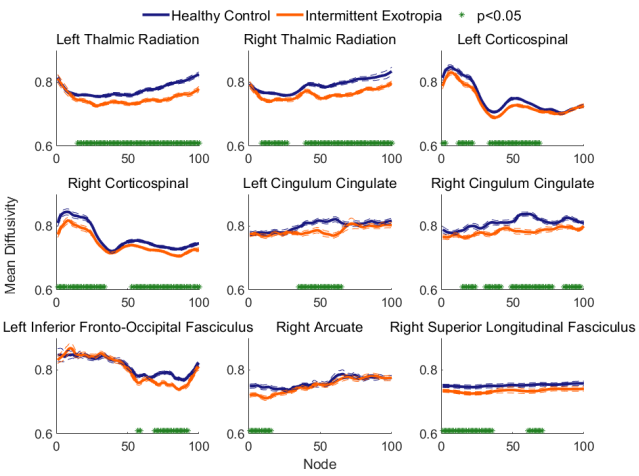

Fig. 2: Between-group differences in mean diffusivity along major fiber tracts

Conclusion: Abnormalities in microstructural properties along visual-related fiber tracts are likely to contribute to difficulties in visual information processing in IXT patients, which may help to understand the underlying pathological mechanism of IXT.

References: [1] Lavrich, Curr Opin Ophthalmol. (2015). [2] Yan, PloS one. (2010). [3] Huang, Neuropsychiatr Dis Treat. (2016). [4] Yeatman, PloS one. (2012).

Acknowledgement: This work was supported by the National Natural Science Foundation of China (No. 61901465).

Cerebral White Matter Dynamic Functional Connectivity in Patients with Brain Arteriovenous Malformations (AVM) using Multi-modal MRI

Qiji Shi[1], *Xiaofeng Deng*[2], *Fangrong Zong*[1] *

[1]School of Artificial Intelligence, Beijing University of Posts and Telecommunications, Beijing, China; [2]Department of Neurosurgery, Beijing Tiantan Hospital, Capital Medical University, China; *Corresponding author

Introduction: Brain arteriovenous Malformations (AVM) belongs to a rare congenital lesion, which may involve language areas but the patients usually have no language barriers. AVM thus becomes a unique model to study the cognitive function mechanism. The purpose of this research is to explore reorganisation patterns of AVM patients in terms of white matter functional connectivity, which is a quantitative parameter obtained from diffusion MRI and functional MRI (fMRI) datasets.

Methods: In this research, 34 left hemisphere AVM patients and 32 healthy controls (HCs) were included. Each participant underwent a 3T fMRI scanning while performing visual synonym judgment task. Functional connectivity (FC) were obtained through temporal correlations of the fMRI signals between two brain regions. In addition, the diffusion tensor imaging (DTI) images (b = 0, 1000 s/mm^2 with 64 diffusion directions) were acquired and the whole-brain tractography were calculated by constrained spherical deconvolution (CSD) [1]. Subsequently, Track-weighted dynamic functional connectivity (TW-dFC) was determined to map the functional connectivity onto corresponding white matter fasciculus. Its intensity represents the averaged FC across all tracts traversing that voxel [2] (Fig.1):

$$\text{TW} - \text{dFC}\ (v,t) = \frac{1}{N_v}\sum_{i=1}^{N_v} FC_i(t) \qquad \text{(Eq.1)}$$

where N_v is the number of tracts traversing a specific voxel v. Regional-average was calculated to estimate the TW-dFC intensity within each group and then two sample t-test was applied to detect the specific reorganization area of AVMs.

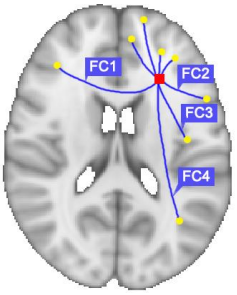

Fig. 1: The illustration of TW-dFC. Red block means a voxel v. Blue lines represents four tracts traversing that voxel and corresponding FCs were mapped onto tracts.

Results and discussion: In visual synonym judgment task, the TW-dFC intensity of AVM patients was significantly higher than that of HCs in the left anterior thalamic radiation (ATR), right inferior fronto-occipital fasciculus (IFOF) and inferior longitudinal fasciculus (ILF) (Fig.2). While in the left hemisphere fasciculus, the TW-dFC value of HCs is significantly higher than that of AVM ($p < 0.05$ FWE correction at the cluster level).

Conclusions: It is the first study to compare the TW-dFC between AVM patients and HCs. Through performing visual synonym judgment task, AVM patients were found to reorganize their language function mainly in the right hemisphere fasciculus.

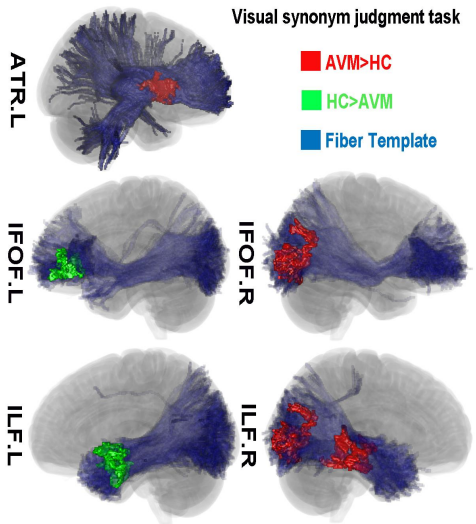

Fig. 2: Statistical differences between AVM and healthy controls (HC). AVM TW-dFC intensity is significantly higher than HC group (in red) and HC higher than AVM (in green).

References: [1] Tournier, J.D. et al, NEUROIMAGE. (2007). [2] Calamante, F. et al., Brain Struct Funct. (2017).

Acknowledgement: This work was supported by the National Natural Science Foundation of China (No. 61901465).

Paul Callaghan Young Investigator Competition I

Chair: Volker Behr, University of Würzburg

Challenging applications of low-field magnetic resonance in harsh environments

Keelan T. O'Neill[a], *Einar O. Fridjonsson*[a] *and Michael L. Johns*[a].
[a]University of Western Australia, Crawley, Australia.

Low-field nuclear magnetic resonance (NMR) is a well-established technique used for characterising porous media in laboratory and logging environments. NMR enables the determination of porosity, fluid volumes, and a qualitative estimation of permeability in complex geological environments. Recent technological advances in NMR instrumentation have allowed for the measurement of complex properties in challenging environments, such as oil and gas reservoirs and Antarctic sea ice. This work aims to extend NMR measurements to three applications with challenging operating and measurement conditions: designing an NMR logging-while-drilling (LWD) tool to operate in hard rock iron ore mining [1], performing accurate quantitative characterisation in iron ore [2], and characterising water in space exploration [3].

NMR LWD is a common service in the oil and gas industry, allowing for real-time formation evaluation. However, mineral exploration drilling is highly unfavourable for LWD due to the high shocks and vibrations experienced. To design an NMR LWD tool for such environments, detailed electromagnetic simulations are required to quantify the impact of tool motion on NMR measurements during logging. The simulations can optimize the design of the tool to be robust to tool motion. The critical design considerations for NMR tools susceptible to motion are reducing the radial magnetic field gradient and the echo spacing. These considerations have been incorporated in the design of a prototype NMR LWD tool currently under development.

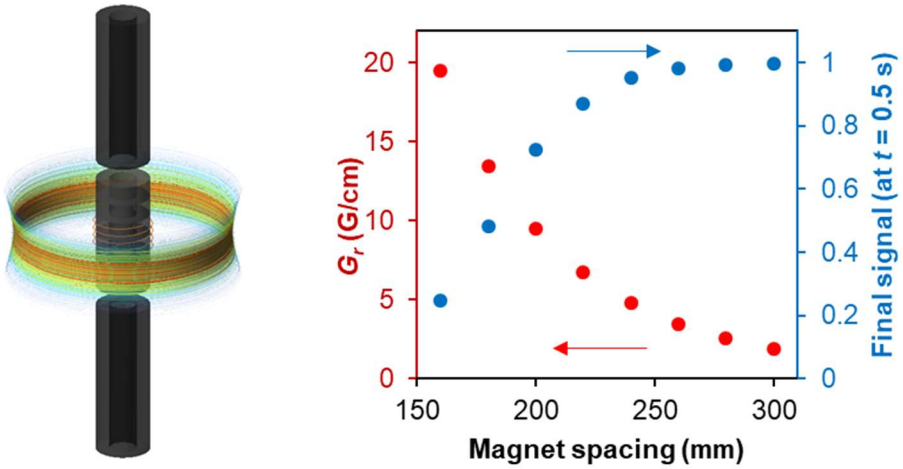

Fig. 1: Model demonstrating the excited volume of a NMR logging tool from electromagnetic simulations & a demonstration of the impact of the magnet spacing on the radial gradient and subsequently signal decay [1].

NMR measurements of water within iron ore samples are complicated by the presence of high internal magnetic field gradients due to magnetic susceptibility differences at the ore-water interface. To quantify key material properties, advanced 2D relaxometry measurements can be used. Decay due to internal fields Carr-Purcell Meiboom-Gill (DDIF-CPMG) measurements are utilized to quantify 2D l_s-T_2 (where ls is the pore length scale), which is subsequently used to quantify the surface relaxivity of samples. Multi-echo measurements can then be used to determine T_2-g_{eff} (where g_{eff} is the effective internal gradients). The multi-regime model is used to model the diffusive NMR signal attenuation in internal gradients. The multi-regime model is a key step in accurately segregating surface relaxation

and diffusive relaxation in high susceptibility materials, which is crucial in accurately estimating properties such as pore size distributions and permeability in iron ore samples.

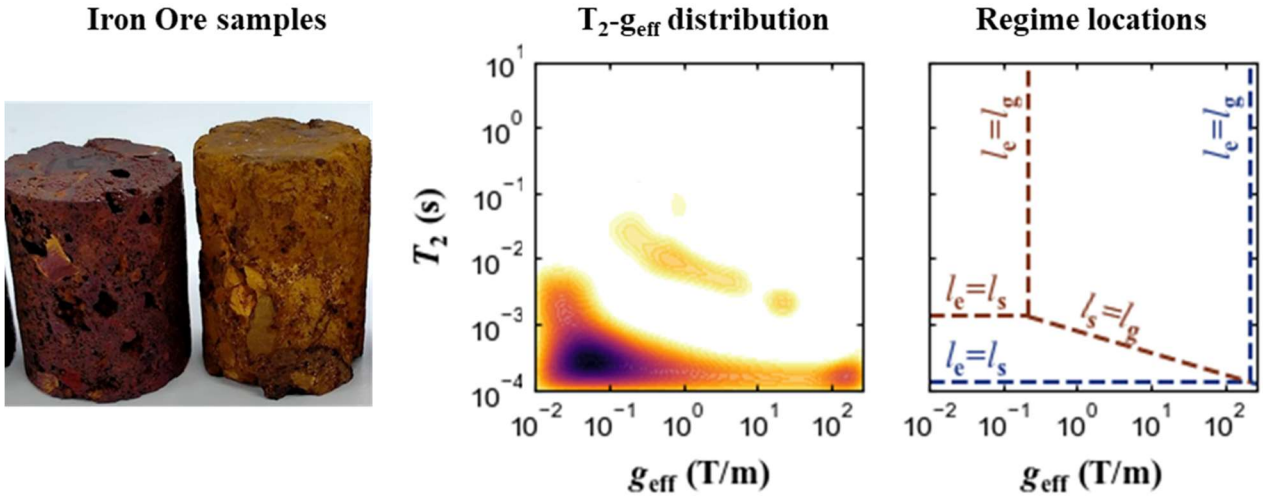

Fig. 2: Demonstrative image of multi-echo measurements conducted on iron ore core samples. The measurements are used to quantify T_2-g_{eff} distributions: where the importance of the regime transitions is paramount to the results [2].

Finally, this work considers the application of NMR to extra-terrestrial materials for space exploration. Laboratory NMR measurements are conducted on Lunar and Martian regolith simulants. DDIF-CPMG measurements are used to quantify the pore-size distributions. These measurements are translated to particle size distributions (using a simple pore-to-particle model) and validated against laser particle size analysis measurements. Multi-echo measurements are used to quantify water volumes as both clay-bound and inter-particle water. The NMR measured moisture content showed reasonably good agreement to corresponding gravimetric measurements used for validation. The implications of these measurements are discussed, and potential future developments of NMR systems for space exploration are suggested.

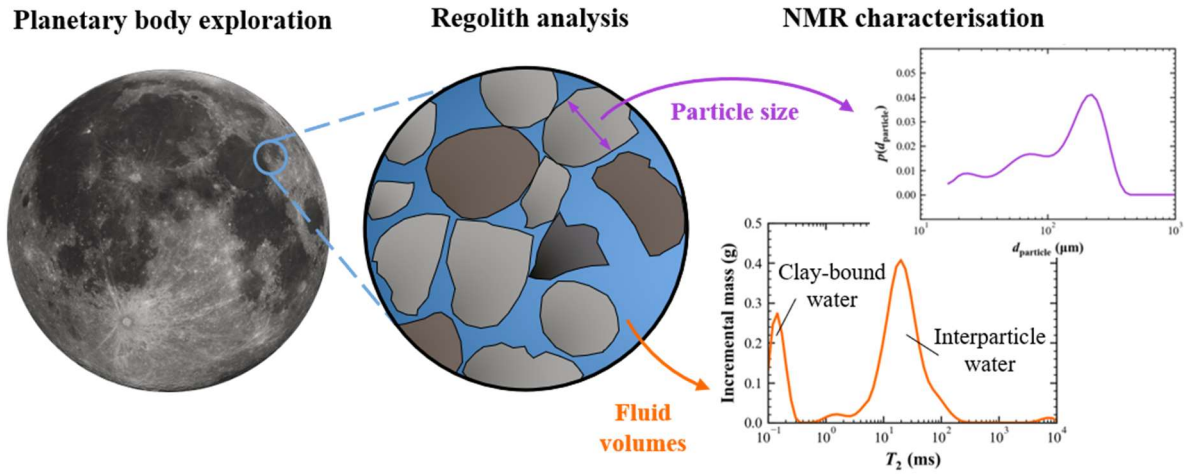

Fig. 3: Conceptual image of using NMR for planetary regolith analysis. Low-field NMR is capable of estimating particle size distributions as well as quantifying the fluid volumes (bound and interparticle) in such samples [3].

References: [1] O'Neill *et al.* J Magn Reson (2022), [2] O'Neill *et al.* Geophys J Int (2022), [3] O'Neill *et al.* Icarus (2023).

Investigating synergistic effects between cellulose and lignin for advanced forest carbon fibers: mass transport characterization with magnetic resonance methods

F. Guerroudj[1], *J. Bengtsson*[2], *K. Jedvert*[2] *and D. Bernin*[1]

[1]Chalmers University of Technology, Gothenburg, Sweden; [2]RISE, Mölndal, Sweden

Introduction

Carbon fibers (CFs) have a high specific strength and stiffness, which makes them very efficient reinforcements in composite materials for light-weight applications. The production of CFs requires a high carbon content precursor that later can be carbonized. Forest-based products: lignin and cellulose are an attractive alternative to the fossil-based polymer commonly used. Cellulose contributes to the strength of the precursor fibers, while lignin, to the high carbon content.

To obtain fibers, these materials need first to be dissolved in e.g. ionic liquids before being coagulated in an non-solvent e.g. water. It has been shown that wet spinning of lignin-cellulose ionic liquid solutions is a promising method for producing forest-based CFs precursors [1]. Several synergistic effects of using lignin and cellulose have been identified and affect the performance during spinning and consequently the produced CFs. These synergetic effects are very poorly understood and not deeply explored.

A special focus is on the mass transport of the solvent and non-solvent occurring during the coagulation process, where cellulose and lignin precipitate to form a rigid fiber. Complementary to some theoretical and experimental studies [2,3], *in-situ* NMR- and MRI-based methodologies are used to characterize the mass transport: solvent exchange and lignin leaching, under different coagulation conditions, as well as morphological analysis of the coagulated cellulose-lignin films.

Materials and methods

A tube-shaped membrane was used as a model system for filament coagulation during wet spinning. The cellulose-lignin ionic liquid membrane was coagulated in a bath containing a non-solvent, illustrated in Figure 1. Several coagulation conditions are considered including different thicknesses of the membrane (1 to 3 mm), solvents, non-solvents, and lignin with different molecular weights and functional groups.

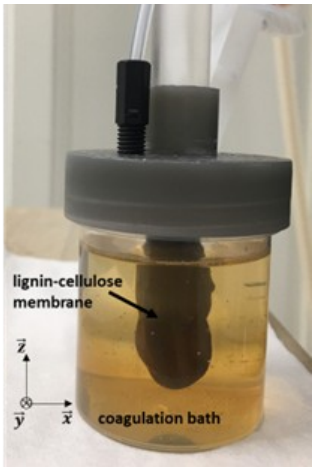

Figure 1. MRI set-up for in-situ mass transport characterization with MRI

The MR experiments are performed on a Bruker Avance III 300 MHz, with a ^{1}H transmit/receive probe of 66 mm diameter.

To visualize the mass transport, a single shot RARE sequence combined with slice saturation was applied and 2D resolved signal intensity maps were recorded throughout the coagulation process.

In addition, spectroscopic information in a voxel was measured to characterize and follow the coagulation bath composition. Lignin leaching over time was accessed using high-field NMR spectroscopy.

Solid state NMR spectroscopy was used to study the morphological structure of cellulose, its crystallinity and the functional groups of lignin of the coagulated and carbonized cellulose-lignin films.

Results and discussion

During the coagulation process the solvent molecules (ionic liquid) are exchanged by the non-solvent molecules. The slice saturation method allowed for a visualization of these dynamics, and an estimation of the stabilization time of the mass transport, when lignin-cellulose precipitate and form a rigid film. In addition, a swelling of the membrane due to the solvent/non-solvent exchange is observed and characterized by MRI.

The obtained MR images showed that the coagulation conditions affect the dynamics of the mass transport. Figure 2 illustrates this impact, when different non-solvents: water and ethanol, were used. As the slice saturation is sensitive to the mass transport of the molecules, the recorded maps showed intense exchange and mixing in the beginning. Analysis of these maps allowed to estimate the time of stabilization of the mass transport depending on the non-solvent.

a. b.

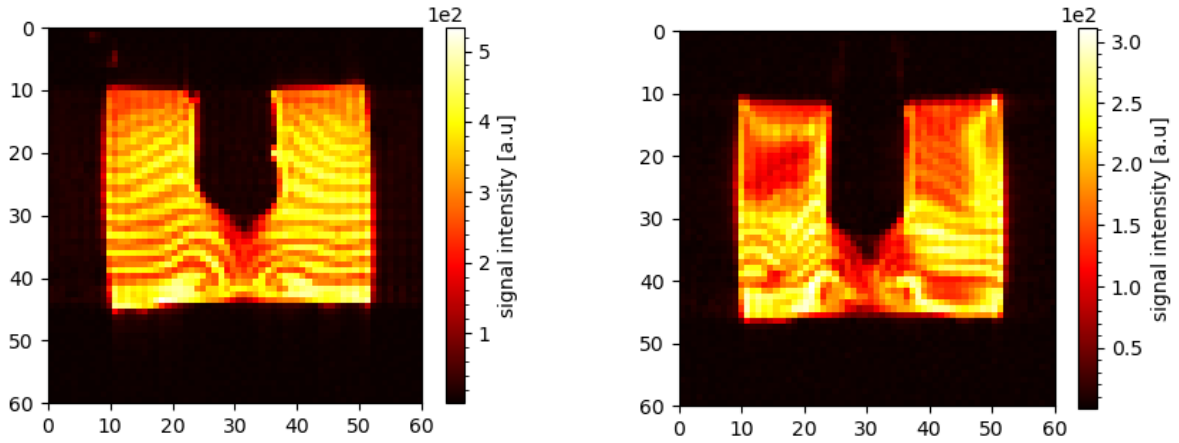

Figure 2. Mass transport measurements: 2D signal intensity map in xz plan (geometric axis in mm) showing the dynamics of solvent exchange in the coagulating bath containing water (a) and ethanol (b).

Following the coagulation bath composition using the voxel spectroscopy allowed further analysis of the exchange. Quantification of the lignin leaching during the coagulation showed that the coagulation process depends on the non-solvent used.

The NMR/MRI including the solid-state ^{13}C NMR results showed furthermore that the chemical and the morphological properties of the coagulated cellulose-lignin membranes are highly dependent on the coagulation conditions. These coagulated films were also carbonated at different temperatures, up to 1000 °C. The ^{13}C solid-state NMR spectroscopy results showed different morphologies of the cellulose depending on the considered temperature.

In summary, the provided information provided a better understanding to optimize the stabilization/carbonization process used for transforming cellulose-lignin films into bio-based CFs.

Conclusion

In this study, applying a wide range of different NMR/MRI methods revealed how variations in the raw materials affect the quality of the fibers, and how the process, and consequently the CFs, can be further optimized. For a more in-depth investigation of the mass transport, we aim to compare our results with computational fluid dynamic simulation models to validate and quantify the dynamics during the coagulation process. These models could then be applied to the wet spinning process.

References [1] Bengtsson A, *ACS Omega* (2022); [2] Bengtsson J, *Holzforschung* (2019); [3] Hedlund A, *Macromolecules* (2017).

Operando MR imaging of the products of Fischer Tropsch synthesis within catalyst pores

Q. Zheng[1]
[1]Department of Chemical Engineering and Biotechnology, University of Cambridge, UK

Introduction

To achieve insight into a heterogeneous catalytic process, it is necessary to characterize the chemical reaction directly from within the catalyst pores. Magnetic resonance (MR) techniques are excellent tools for this purpose as they are non-invasive and can probe multiple properties including chemical compositions, diffusion and flow fields from within a catalytic reactor [1]. However, using MR methods to obtain chemical information in pores is limited by the lack of spectral resolution due to the presence of field inhomogeneity.

This work [2] reports *operando* MR characterization of Fischer-Tropsch synthesis (FTS). FTS is an important industrial process that produces sustainable fuels and chemicals from renewable resources [3]. The FTS product consists primarily of *n*-alkanes that have a broad carbon number distribution. Characterization of this distribution is difficult using chemical shifts which do not discriminate *n*-alkanes of different chain lengths. Further, by-products including water, oxygenates and branched alkanes are also produced, and they have significant influence on catalyst performance. It is still challenging to discriminate these by-products from *n*-alkanes in the product mixture confined in pores. In the present work, multiple MR techniques have been developed and applied to discriminate and characterize different product species of FTS directly from within catalyst pores with spatial resolutions of one to three dimensions.

Methods

The reactor is constructed of silicon nitride, a non-magnetic material, and has an inner diameter of 20 mm. It was packed with three layers of 1 wt% Ru/TiO_2 catalyst pellets with non-porous SiC particles packed between catalyst layers to achieve isothermal operation (Fig. 1a). The reaction was operated at typical industrial conditions of 220 °C, 37 bar and three feed H_2/CO ratios of 2, 1 and 0.5.

The reactor was placed inside the magnet of a Bruker Avance III HD spectrometer with the catalyst bed located at the center of a 66 mm i.d. birdcage r.f. coil. The 7.1 T magnet is equipped with a gradient set providing a maximum gradient strength of 83.24 G cm^{-1} in three directions. The characterization of product carbon number distribution was achieved by measuring the distribution of diffusion coefficients of the products which was then transformed to the carbon number distribution using a recently developed method that links the diffusion coefficients and carbon numbers of *n*-alkanes [4]. The spatially-resolved diffusion measurement was obtained using a APGSTE sequence followed by RARE imaging. Characterization of water and oxygenates was achieved by measuring the distribution of T_1 relaxation times of the product mixture using a saturation recovery sequence. The characterization of branched alkanes in the product mixture was achieved using 2D DQF-COSY spectroscopy following a recently developed method [5].

Results and discussion

Figure 1a presents the 3D ^1H intensity image of the reactor which shows the distribution of liquid products within the reactor. It is observed that the accumulation of liquid builds up as the conversion increases down the reactor. The 2D map of the average carbon numbers of intra-pellet products at the bottom catalyst layer is shown in Fig. 1b. Distributions of diffusion coefficients are measured from individual image pixels and they are transformed to carbon number distributions. The carbon number distributions measured from a local image pixel are also shown in Fig. 1b for the three feed H_2/CO ratios. It is seen that the product carbon numbers increase with decreasing feed ratios, indicating higher chain growth probability at lower feed ratios. The image in Fig. 1b

confirms the spatial heterogeneity of the product distributions within the catalyst layer and in individual catalyst pellets. Figure 1c shows a 2D T_1 relaxation time – chemical shift correlation spectrum acquired from the reactor at feed ratio 2 where the signals of hydrocarbons, oxygenates and water are discriminated. The chemical shift and T_1 relaxation time of water suggest that a layer of liquid-phase water is present on the catalyst pore surface at the reaction conditions. The signal intensities in Fig. 1c are used to estimate the concentration of oxygenates and water in pores, which, together with their T_1 relaxation times, reveal hydrophobicity of the catalyst surface under *operando* conditions. The characterization of branched alkanes in pores is achieved using 2D NMR spectroscopy. Figure 1d shows a 2D DQF-COSY spectrum of the product mixture in pores where a pair of cross peaks associated with methyl-branched alkanes is identified. The signal intensities of the cross peaks are used to estimate the branching composition in the mixture and the result indicates the presence of multimethyl branched species in pores. The results in Fig. 1c and 1d are non-spatially resolved and these measurements are currently being combined with the MRI modality to gain insight with spatial resolution.

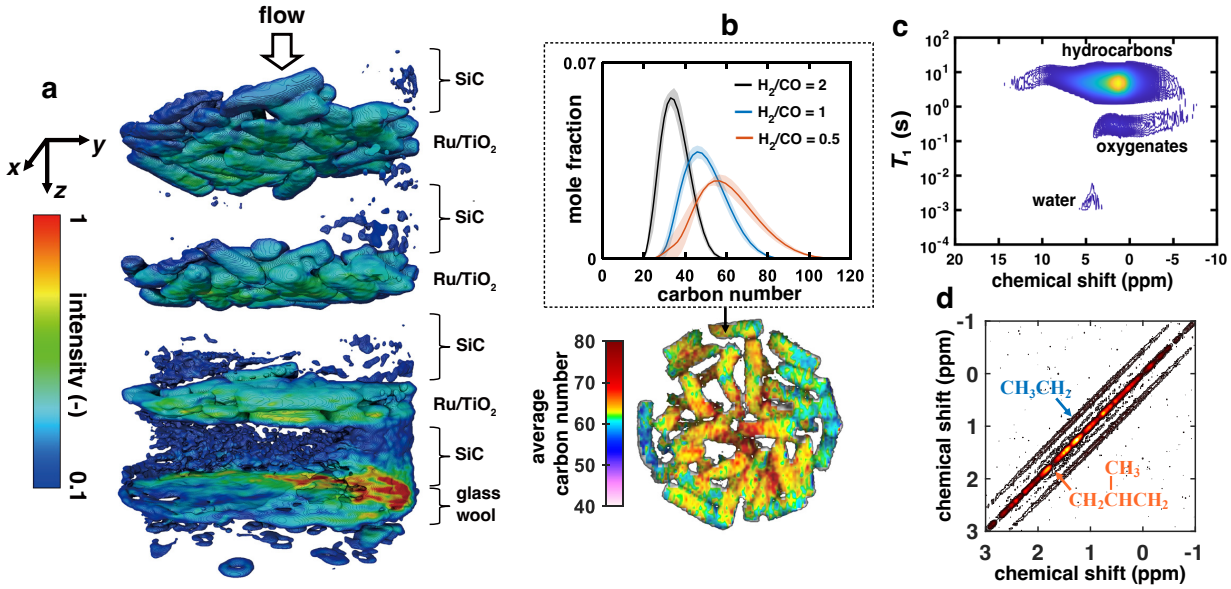

Fig. 1: (a) 3D ^{1}H intensity image of the reactor. Field of view (FOV) = 25(x)×25(y)×80(z) mm^3, spatial resolution = 195(x)×195(y)×313(z) µm^3. (b) 2D map of the average carbon numbers of intra-pellet products at the bottom catalyst layer. FOV = 22(x)×22(y) mm^2, spatial resolution = 172(x)×344(y) µm^2, 3 mm slice. The carbon number distribution measured from a local image pixel are also shown. (c) 2D correlation spectrum of T_1 relaxation times and chemical shifts. (d) 2D DQF-COSY spectrum of the product mixture in pores. The results in (a), (c) and (d) were obtained at feed H_2/CO ratio of 2 while the 2D image in (b) was measured at a feed ratio of 0.5.

Conclusion

This work applies multiple MR methods to achieve *operando* characterization of the complex product mixture of FTS directly from within the catalyst pores. The results provide unique information of the product distribution and confirm the spatial heterogeneity of the reaction. The insight obtained facilitates the optimization of the catalyst and process.

References

[1] Gladden, L. F. & Sederman, A. J., Annu. Rev. Chem. Biomol. Eng. **8**, 227-247 (2017).
[2] Zheng, Q. et al., Nat. Catal. **6**, 185–195 (2023).
[3] Panzone, C. et al., J. CO_2 Util. **38**, 314-347 (2020).
[4] Williams, J. et al., Anal. Chem. **92**, 5125-5133 (2020).
[5] Zheng, Q. et al., Anal. Chem. **94**, 3135-3141 (2022).

In situ and *operando* Spectroscopy, Imaging and Tomography of Batteries

Joseph Okeke[1,3], Ethan Williams[2], Giar Alsofi[2], Phoebe Allan[1], Emma Kendrick[2], Martinus P. Widjaja[3], Shahabeddin Dayani[3], Henning Markötter[3], Anja Waske[3], Melanie Britton[1]

[1]School of Chemistry, University of Birmingham, Birmingham, UK, [2]School of Metallurgy and Materials, University of Birmingham, Birmingham, UK [3]Bundesanstalt für Materialforschung und -prüfung, Berlin, Germany

Introduction: The development of more powerful and more efficient lithium-ion batteries (LIBs) is a key area in battery research, aiming to support the ever-increasing demand for energy storage systems. To better understand the causes and mechanisms of degradation, and thus the diminishing cycling performance and lifetime often observed in LIBs, *in operando* techniques are essential, because battery chemistry can be monitored non-invasively, in real time. Moreover, there is increasing interest in developing new battery chemistries. Beyond LIBs, sodium ion batteries (NIBs) have gained increasing interest in recent years, as they are a promising candidate to complement LIBs, owing to their improved sustainability and lower cost, while still maintaining high energy density.[1] Initial phases of NIB commercialisation have occurred in the past year. However, for the widespread commercialisation of NIBs, there are still challenges that need to be overcome in developing optimized electrode materials and electrolytes. For the development of such materials and greater understanding of sodium storage mechanisms, solid electrolyte interface (SEI) formation and stability, and degradation processes, *in operando* methodologies are crucial.

Among the techniques available for *in operando* analysis, nuclear magnetic resonance spectroscopy (NMR) and imaging (MRI) are becoming increasingly used to characterize the chemical composition of battery materials, study the growth and distribution of dendrites, and investigate battery storage and degradation mechanisms. *In situ* and *in operando* ^{1}H, ^{7}Li and ^{23}Na NMR and MRI have recently been used to study LIBs and NIBs, identifying chemical changes in Li and Na species respectively, in metallic, quasimetallic and electrolytic environment as well as directly and indirectly studying dendrite formation in both systems.[2-4] The ability of NMR and MRI to probe battery systems across multiple environments can further be complemented by the enhanced spatial resolution of micro-computed X-ray tomography (μ-CT) which can provide insight into battery material microstructure and defect distribution.

Here, we report *in operando* ^{1}H and ^{7}Li NMR and MRI experiments that investigate LIB performance, and the identification of changes in the Li signal during charge cycling, as well as the observation of signals in both ^{1}H and ^{7}Li NMR spectra that we attribute to diminishing battery performance, capacity loss and degradation. Additionally, recent *operando* methodology are adapted and implemented to study Sn based anodes in NIBs. ^{23}Na spectroscopy is performed to monitor the formation and evolution of peaks assigned to stages of Na insertion into Sn, while ^{1}H MRI is used to indirectly visualize the volume expansion of Sn anodes during charge cycling. Battery operation and degradation is further explored in these NIBs, using μ-CT, where the anode is directly visualized to a higher resolution and the loss of electrolyte in the cell, during cycling is observed.

Methods: ^{1}H and ^{7}Li NMR and MRI experiments were performed on a lithium-ion full-cell comprising a NMC622 cathode and graphite anode with 1 M lithium hexafluorophosphate in ethylene carbonate: ethyl methyl carbonate (3:7 wt%) + 2% vinyl carbonate electrolyte. *Operando* ^{1}H and ^{23}Na NMR and MRI, and μ-CT experiments were performed on a sodium-ion full-cell consisting of a NMST (2488) cathode, a Sn based anode with a with a 1 M sodium hexafluorophosphate in ethylene carbonate: fluoroethylene carbonate: diethyl carbonate (12.6: 47.1: 5.3: 35 wt%) electrolyte. All cells were assembled in a custom Swagelok type cell configuration.

Results and discussion: *In operando* ^{7}Li NMR spectroscopy enabled the observation of dilute and dense stages of lithium intercalation into the graphite anode, during the charging of well performing cells, over multiple cycles. The evolution of peaks in ^{7}Li NMR of poor performing cells is directly compared to that of well performing cells, highlighting differences in the appearance of peaks associated with Li intercalation. The appearance and growth of peaks in both ^{7}Li and ^{1}H NMR spectra have been identified and highlighted as the potential cause of battery degradation. ^{7}Li MRI has shown the irreversible build-up of non-metallic lithium in the separator of lithium-ion battery that begun to degrade after multiple operando cycles.

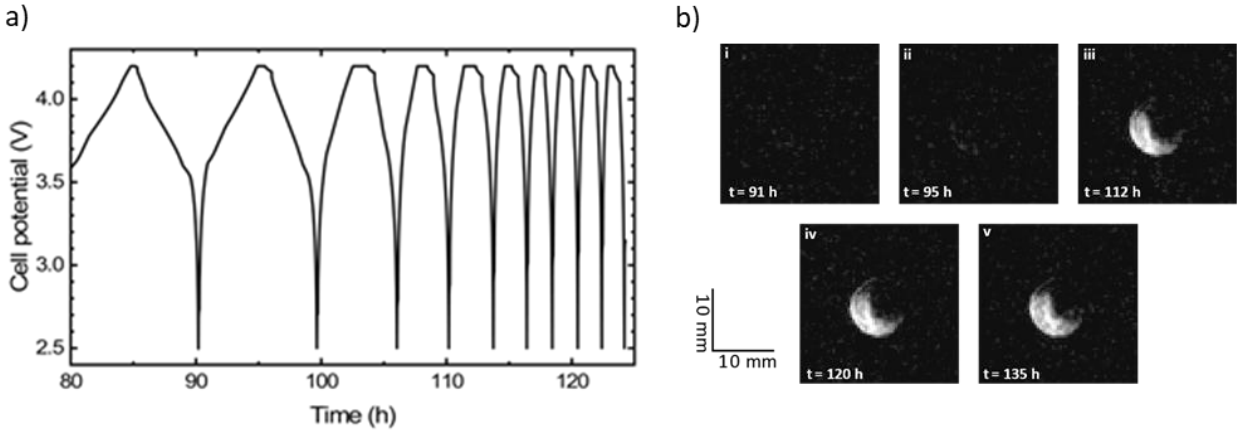

Figure 1a) Charge profile of *operando* cycles between 80 h and 125 h. b) ^{7}Li magnetic resonance (MR) images of the separator region acquired during the *operando* cycling of a LIB at a C/10 rate.

Similarly, in our NIB experiments, the appearance and evolution of peaks attributed to certain quasimetallic Na-Sn insertion stages were monitored in real time using ^{23}Na NMR spectroscopy. *In operando* ^{1}H MRI experiments enabled the indirect visualization of Sn anode volume expansion and contraction. This is observed through changes in the dimensions of the separator, in a sagittal ^{1}H MR image, after taking the difference between an image of the pristine cell and images acquired at different time points during electrochemical cycling. NIB degradation was observed using *operando* µ-CT, where the loss of electrolyte in the separator was visualized during cycling.

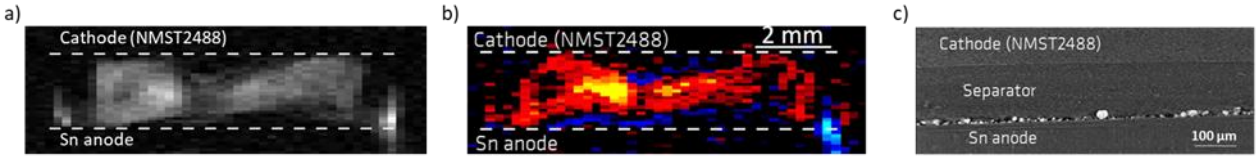

Fig. 2a) Pristine ^{1}H MR image of proton in the electrolyte contained in the battery separator. b) The result of taking the difference between the fully charged and pristine cell images, red pixels show an increase in signal intensity of the electrolyte between the fully charged and pristine cell while blue pixels show a decrease. c) a 2D µ-CT slice of the electrode stack.

Conclusion: Degradation processes have been observed, *in operando*, using NMR, MRI and µ-CT. The irreversible loss of non-metallic Li in a lithium full cell has been observed, offering a unique insight and understanding into the failure of LIBs. The volume expansion of Sn based anodes in NIBs has been indirectly visualized using ^{1}H MRI and the evolution of quasimetallic Na-Sn insertion phases monitored with ^{23}Na NMR. *Operando* µ-CT has shown degradation of NIB through the loss of electrolyte in the separator during cycling. The size and distribution of Sn in the anode has also been observed in detail.

References: [1] Li et al. Acc. Chem. Res. (2015) *48* (6), 1657-1665, [2] Bray et al. Nat. Commun. 11, 2083 (2020). [3] Märker et al. J. Am. Chem. Soc. (2020), 142, 17447-17456, [4] Mohammadi et al. J. Magn. Reson. (2014), 245, 143-149.

Paul Callaghan Young Investigator Competition II

Chair: Einar Fridjonsson, the University of Western Australia

Chebyshev nodes-based fingerprinting of magnetic nanoparticles

J. Günther[a], *T. Kampf*[b], *B. Friedrich*[c], *M.A. Rückert*[a], *T. Reichl*[a], *F. Mikoleit*[d] ,*V.C. Behr*[a], *P. Vogel*[a],
[a] Experimental Physics 5 (Biophysics) University of Würzburg, Germany
[b] Diagnostic and Interventional Neuroradiology, University Hospital Würzburg, Germany
[c] Section of Experimental Oncology and Nanomedicine (SEON), University Hospital Erlangen
[d] Department of Microbiology, University of Bayreuth, Germany

Introduction: Magnetic Nanoparticles (MNP) are of great interest in many medical and technical research fields. Depending on their properties, MNPs show a unique behavior when brought into a magnetic field. Critical Offset Magnetic Particle Spectroscopy (COMPASS) is a new technique to detect differences of the MNP properties with extremely high sensitivity. In this work, COMPASS was extended create a multidimensional fingerprint of the MNP system to characterize them.

Methods:
COMPASS is based on applying static (H_{DC}) and dynamic magnetic fields (H_{AC}) to the MNPs, which give a nonlinear response on the fields and thus cause higher harmonics in the Fourier transform of the inductively measured MNP signal. Tracking a single harmonic while applying an increasing static field leads to characteristic curves that resemble Chebyshev polynomials of 2nd kind. These curves show nodes called critical points (CP). The phase of the complex signal reveals a steep change at the CP making them highly sensitive to differences in the MNP mobility.

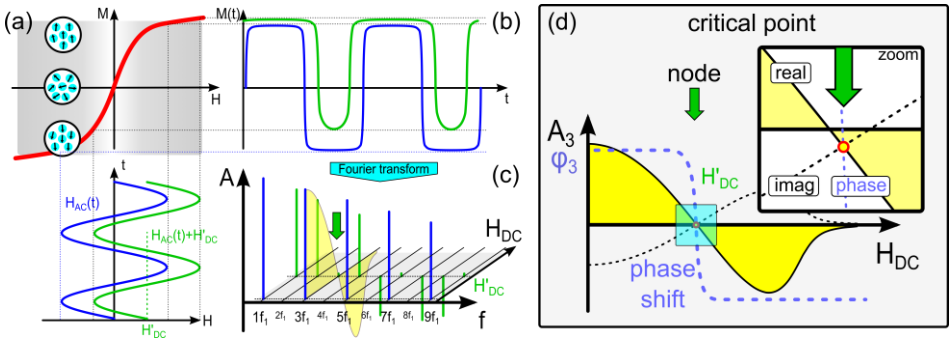

Fig. 1: Formation of the MNP signal (a,b) and the Chebyshev polynomials (c,d).

Results: For a COMPASS fingerprint, a 4D dataset is generated by varying H_{AC} and H_{DC}, the harmonic and the properties of the particle system like particle size, viscosity, or temperature. The CPs are visualized by building the derivative of the phase pattern. The fingerprint concept can be shown by comparing the sixth harmonic Synomag (Micromod) and Resovist (Bayer) and magnetosomes [3]. The fingerprint of the particle types shows differences in peak position and width, making the samples distinguishable.

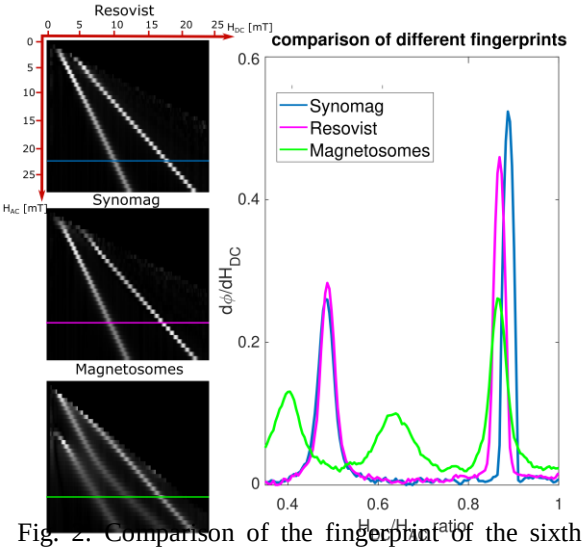

Fig. 2: Comparison of the fingerprint of the sixth harmonic of Synomag, Resovist and magnetosomes.

Conclusion: COMPASS is a new method for highly sensitive analyses of MNP ensembles and their modification based on the evaluation of Chebyshev nodes in the MNP signal. It has been shown that a dedicated fingerprinting routine can be introduced based on the COMPASS effect, characterizing the particle systems with a unique distribution of critical points depending on the particle mobility.

References: [1] Kudr, J. Nanomater. (2017), [2] Vogel, Nat. Comm. (2022), Mikoleit, F. Bioinspired, Biomim (2018). This work was funded by the DFG (BE 5293/1-2, VO 2288/3-1)

Optimization Scheme for Single-sided Inward-outward (IO)-ring Permanent Magnet Array

Ting-Ou Liang[1], Erping Li[2], Wenwei Yu[3], Shao Ying Huang[1]
[1]Singapore University of Technology and Design, Singapore, Singapore, [2]Zhejiang University, Hangzhou, China, [3]Chiba University, Chiba, Japan

Introduction: Permanent magnet array (PMA) designs are important for portable magnetic resonance imaging (MRI) for its portability. Aside from the popular Halbach array that provides transverse magnetic field, another type of PMA called inward-outward (IO)-ring has been drawing attention due to its strong field in the axial direction [1,2]. Besides, there has been works on single-sided PMA to produce built-in gradient [3,4]. In this work, we have proposed a method of optimizing an open IO-ring via elliptical and individual adjustment of magnets. It leads to a magnetic field pattern with high linearity.

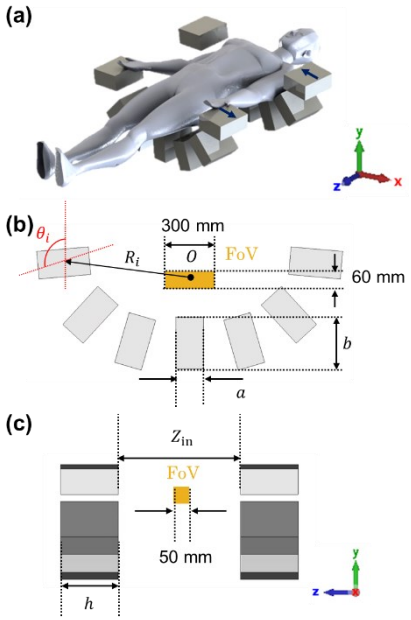

Fig. 1: (a) The 3D view, (b) the front view, and (c) the side view of the proposed design with field-of-view (FoV) indicated in yellow.

Methods: The optimization starts with an overall elliptical reshape of the IO-ring with the magnets closer to FoV, and then comes with individual adjustment of location and orientation angles for each magnet. Fig.1(a) shows the overview of the optimized design, whose cross-sectional and side views are shown in Fig.1(b) and (c), respectively. The design parameters of an IO-ring are the radius R_i from the z-axis, the inner distance Z_{in} between the two rings, the dimension of the magnet block (a, b, h), the spacing angle θ between neighboring magnets, and the number of magnets n in each ring. Before the optimization, the parameters above should be fixed to provide a "roughly" desirable pattern, e.g., a monotonic gradient in this case.
The starting point is a half-IO-ring consisting of magnet blocks (Fig. 2(a)). Then, the magnetic field strength is improved by introducing the elliptical ratio α, which brings the magnets at bottom closer to the target region (Fig.2(b)). The length of the major axis of the ellipse is the radius R_i. With the elliptical adjustment, the magnets will move along the line through the origin and their original center location in the cross-sectional view (the red dotted line on Fig.2(a)(b)).
Finally, by performing individual adjustment on location and orientation of each magnet (Fig.2(c)), higher gradient linearity is achieved. The modified variables are the cross-sectional, i.e., (x, y) center locations and the orientation angle with respect to the magnet center for each magnet. The symmetry of corresponding magnets in the two rings and the symmetry over the xz-plane are kept. Therefore, in the illustrated example, only four modifications are applied for

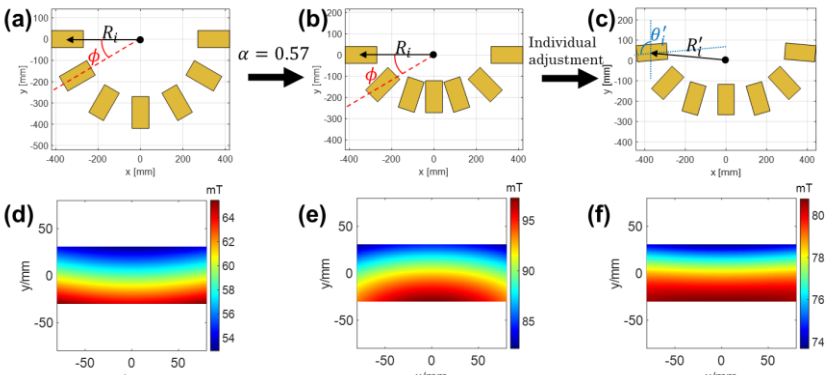

Fig. 2: (a)-(c) The cross-sectional view of a partial IO-ring, the partial IO-ring after elliptical adjustment, and that with further individual adjustment of magnets and (d)-(f) the corresponding magnetic field pattern at z=0.

the center locations and orientation angles, respectively. The corresponding field maps are shown in Fig.2(d)-(f).

Results and Discussion: The magnetic field pattern from the optimized partial IO-ring pair has good consistency along the axial direction. Fig.3 shows the Bz field of the optimized design on slices z=0, 12.5, and 25mm. The average field strength varies less than 1%, and the RF bandwidth is kept within 10%. All slices have high field linearity. Fig.4 shows the corresponding 2D field map and selected 1D field curve at different x-locations. It is shown that the gradient variation is small along the same observation plane.

z [mm]	0	12.5	25
Average B_z [mT]	78	78.2	78.8
RF bandwidth	9.1%	9.3%	10%
Linearity (R^2)	0.970	0.971	0.975

Fig. 3: The Bz field properties at z=0, z=12.5mm, and z=25mm.

The comparison between the performance of the optimized PMA and the original half-IO-ring is shown in Fig.5. Column 1-3 shows the 2D field pattern on z=0 FoV plane, the 1D field plots along the highlighted vertical lines at x=0, 12.5, and 25mm, as well as the 5-Gauss regions, respectively. As shown in Row 1, the optimized design generates a monotonic gradient, averaged at 88.6 mT/m in the y-direction, corresponding to FoV $\leq$ 160mm in the same direction. The average field strength increases from 59.0mT to 78.0mT, and the corresponding RF bandwidth covered by the range of Bz drops from 21.9% to 9.1%, where latter is valid for practical design of corresponding RF coils. The line plots of the optimized design show higher consistency of field strength along the x-direction compared to the half-IO-ring. As for the 5-Gauss region, the half-IO-ring has it in a range of $2700 \times 2630 \times 3060\text{mm}^3$, while that of the optimized design is $2680 \times 2720 \times 3060\text{mm}^3$, where the difference is negligible. The advantage of higher field strength, more practical RF bandwidth, and higher consistency along x-direction of the optimized design is obtained with only a little compromise on the overall linearity, which drops from $R^2 = 0.985$ to 0.970.

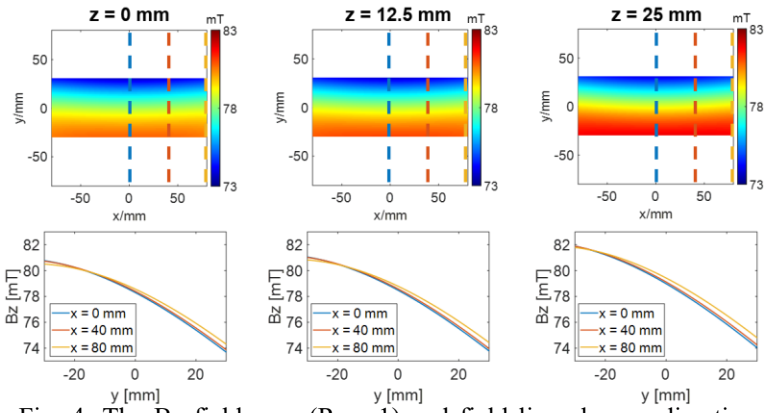

Fig. 4: The Bz field map (Row 1) and field line along y-direction (Row 2) for z=0 (Column 1), z=12.5mm (Column 2), and z=25mm (Column 3).

Conclusion: In this abstract, we propose a method for optimizing a single-sided partial IO-ring PMA. With elliptical reshape and individual adjustment on each magnet, the fine-tuning of magnetic field pattern can be achieved without involving too many magnets.

References: [1] Ting-Ou Liang, Journal of Magnetic Resonance. (2022). [2] G. Aubert,US Patent 5,332,971 (1994). [3] Patrick C. McDaniel, Magnetic Resonance in Medicine. (2019). [4] Bernhard Blümich, Magnetic Resonance Imaging. (1998).

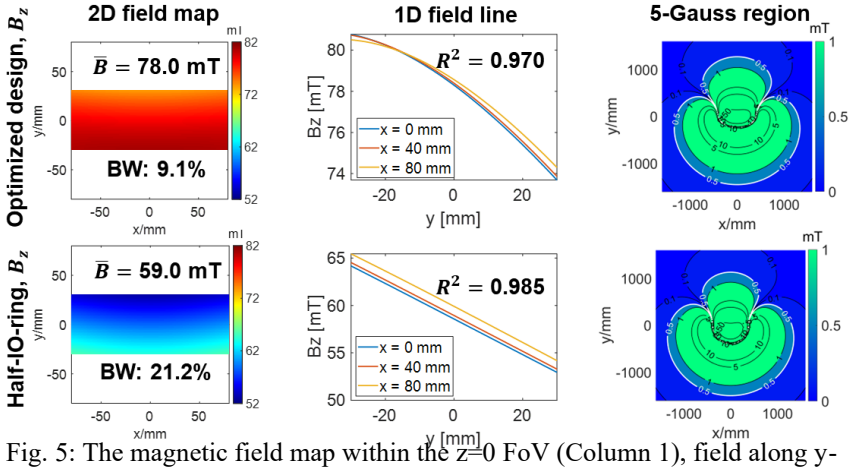

Fig. 5: The magnetic field map within the z=0 FoV (Column 1), field along y-direction (Column 2) and 5-Gauss region (Column 3) for both the optimized design (Row 1) and the original half-IO-ring (Row 2).

A Ceramic Magnet for Flow Profiling and Overhauser DNP

D. Morin, S. Richard, N. Ansaribaranghar, B. Newling, B. Balcom
University of New Brunswick, Fredericton, NB, Canada

Introduction: High field MR/MRI instruments are becoming increasingly sophisticated, capable, and expensive. We, and others, are increasingly considering instruments and measurements based on low field permanent magnets. We describe a new permanent magnet design that employs off-the-shelf, inexpensive grade C8 ceramic magnets to create a large, relatively homogeneous 1.8 MHz (^{1}H) magnetic field. Two versions of the magnet are designed. The first has a uniform static field. This magnet is employed for relaxation and Overhauser dynamic nuclear polarization (O-DNP) [1, 2, 3] studies. The second has a permanent gradient and is employed for flow studies [4, 5], simple profiling, and spatially resolved O-DNP. Pitching the magnets about the y-axis creates and gradient along the x-axis. The utility of the device is demonstrated through measurements with O-DNP, which provides order of magnitude ^{1}H signal enhancements through the irradiation of the unpaired electron of a neighboring free-radical species. With a moderate 422 gauss B_0-field, the corresponding electron paramagnetic (EPR) frequency remains in the S-band, therefore allowing for the enhancement of macroscopic samples.

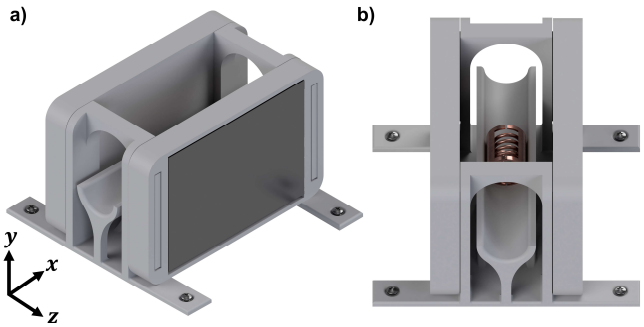

Fig. 1: a) Side and b) front orthographic projection of the ceramic magnets in a 3D printed enclosure. The solenoid RF and Alderman-Grant resonators are visible between the ceramic magnets in b).

Methods: Computer Simulation Technology Studio was used to simulate and determine the design parameters to create both a homogeneous, and 15 gauss/cm constant gradient region. The ceramic magnets have their magnetic poles aligned and are separated by a distance, determined through simulation, to maximize homogeneity. At lower field strengths, rectangular ceramic magnets are a better choice for our field topology compared to more common NdFeB. A solenoid at 1.8 MHz was used for MR excitation and detection. A home-built Alderman-Grant resonator [6, 7] at 1.2 GHz was used for the EPR irradiation. The microwave frequency permits measurement of macroscopic samples, due to the relatively large skin depth, and as such we explore samples of roughly 1 cm diameter, and 2 cm length. Enhancement is achieved with microwave irradiation for several seconds, at a power between 1 – 20 watts. Microwave irradiation ceases immediately before the CPMG part of the pulse sequence. This ensures an appropriate cooldown time to reduce sample heating and minimizes noise via crosstalk between the MR and microwave coils.

Results and discussion: The final constructed magnet used two ceramic magnets mounted on a 3D printed structure for support (Fig. 1). The homogeneous region has a field variation of less than 2 gauss/cm over x = +/- 1 cm. In the constant gradient configuration, the simulated results produced a 15 gauss/cm gradient along the x-axis with a 6° magnet pitch about the y-axis. The magnet holder can be swapped for the homogeneous or constant gradient configuration. The force of attraction is low, so magnets can be moved by hand. O-DNP enhancement measurements may be performed with a range of TEMPO species. Maximum enhancements of x30 were obtained for aqueous 4-Hydroxy-TEMPO.

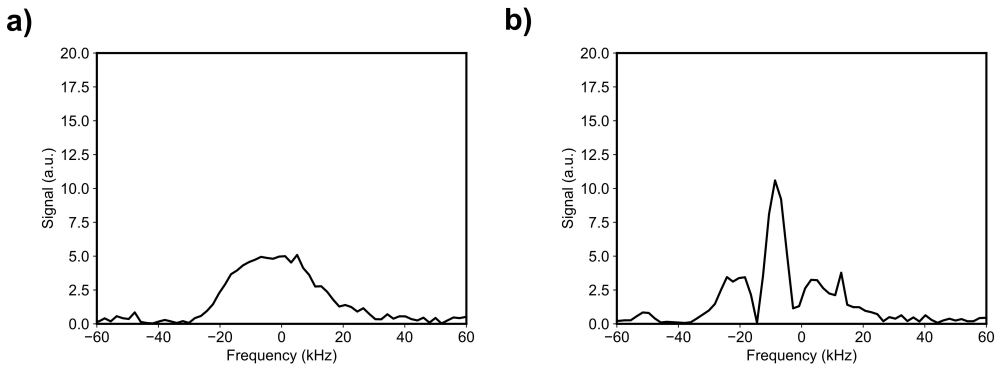

Fig. 2: 1D profile of a vial of aqueous 4-Hydroxy-TEMPO with a microwave irradiation of a) 0-watts and b) 1-watt. The microwave frequency was 1218 MHz (1.8 MHz for ^{1}H). The signal spike in b) corresponds to local enhancement. The enhancement increases with microwave power. The region of enhancement shifts with microwave frequency, permitting spatially selective enhancement. The FOV is 2 cm.

The 15 gauss/cm gradient was employed to explore local enhancement in the form of a 1D profile. Figure 2 shows the 1D profile from a vial of aqueous 4-Hydroxy-TEMPO, with a signal enhancement. The local region of enhancement at -10 kHz in Figure 2 was obtained through microwave irradiation at 1218 MHz with 1-watt of power. Increasing microwave power results in an enhancement which dominates over the non-enhanced region. We show that by simply changing the microwave irradiation frequency, this local region of enhancement can be shifted.

Employing the field gradient along the flow direction, we can measure the flow behavior index n′, and average velocity through the magnitude of odd echo signal (Fig. 3) [4]. A series of CPMG measurements were used to measure water with a flow velocity of 17 cm/s. The results of this MR measurements gave an average flow velocity of 16.5 cm/s and an n′ of 2.0 which is in agreement with the independently known values.

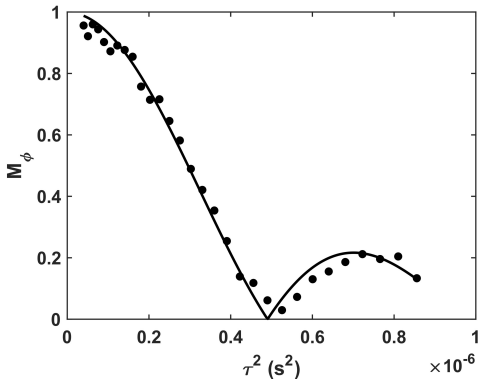

Fig. 3: Magnitude plot of the first odd echo for varying echo time squared for a laminar flow velocity of 17 +/- 1 cm/s. Values determined from fitting of data resulted in an average velocity of 16.5 cm/s and n′ of 2.0. The sample was doped water (T_1 = 26 ms).

Conclusion: This work introduced a new magnet design, which uses ceramic magnets to generate a modest 1.8 MHz magnetic field for ^{1}H. This magnet is appropriate for use with macroscopic samples, as S-band irradiation has good penetration depth. The permanent gradient permits facile flow profiling for rheology measurement. The very wide range of TEMPO and related chemical agents permits O-DNP to be introduced as a contrast parameter in material studies as we will describe.

References: [1] Hausser, Stehlik, Dynamic Nuclear Polarization in Liquids (1968). [2] Yoder, Magnelind, Appl. Magn. Reson. (2018). [3] Lurie, Nicholson, Mallard, J. Magn. Reson. (1991). [4] Guo, Ross, Newling, Lawrence, Balcom, Phys. Fluids (2021). [5] Guo, Paul Callaghan Young Investigator Finalist (2021). [6] Joël, Mihaela, André, NMR Probeheads for Biophys. and Biomed. Exper. (2006). [7] Neudert, Raich, Mattea, Stapf, Münnemann, J. Magn. Reson. (2014).

AI-BSD – a deep learning based model for DTI systematic error removal

J. Lasek[1], *A. Krzyzak*[1]
[1] AGH University of Science and Technology, 30-059 Krakow, Poland

Introduction: Spatial gradient inhomogeneity refers to variations in the strength or direction of the magnetic field gradients used in diffusion-weighted magnetic resonance imaging (MRI), which can lead to distorted or biased diffusion measurements. Systematic errors can arise in diffusion MRI due to factors such as eddy currents, background gradients, or gradient nonlinearity, which can affect the accuracy and reproducibility of the diffusion tensor imaging (DTI) metrics [1-5]. Appropriately spatially calibrated b-matrices, b(r), may successfully eliminate systematic errors, and this can be achieved with a deterministic BSD-DTI method providing more reliable spatially distributed b-matrices [2,5]. We propose a model based on deep learning for the estimation of the corrected b-matrices and, as a result, reduce systematic errors.

Methods:

MRI Acquisition: 114 MRIs of the phantoms were acquired on a 3T Siemens Magnetom scanner at the University Hospital in Krakow, Poland. The spin-echo echo planar imaging (SE-EPI) sequence was used with diffusion weighted (DW) gradients applied in 20 directions; b factor of 0 s/mm^2, 1000s/mm^2, 2000 s/mm^2; repetition time (TR): 3900 ms; echo time (TE): 88 ms; field of view (FOV): 191 x 191 mm^2; voxel size: 2,5 x 2,5 x 2,5 mm^3; 50 slices.

Data preprocessing: 4D matrices were used as input, consisting of 6 matrices of size 76x76x50. These were sequentially stacked: (1) non-diffusion-weighted (b = 0) image, (2) diffusion-weighted image in one direction, (3-5) gradient direction vector component values, (6) value of the b factor. The data were split into: 75 (150000 DW images) studies for the training set, 25 (50000 DWIs) for the validation set and 14 (28000 DWIs) for the test set.

The model output is a 4d matrix consisting of three 76x76x50 b-matrices for the three directions. Reference b matrices were calculated using BSD-DTI software (NMR LaTiS, AGH-UST, Krakow).

Network implementation: The neural network architecture was implemented using Pytorch and the Medical Open Network for Artificial Intelligence (MONAI). The model was trained for 90 epochs using two RTX 3090 GPUs, with a learning rate of 10^{-5} and an Adam optimizer. The L1 loss was utilized as the loss function to measure the absolute difference between the predicted and true output. The network was built from a sequential block consisting of a convolutional layer, an instance normalization layer, a dropout layer, and a Parametric Rectified Linear Unit (PReLU) activation function.

Results and discussion: A value of 0.998 ± 2*10^{-4} SSIM was achieved for the b-matrices predicted using the model against the reference b-matrices generated using BSD-DTI. In Fig. 1. training and validation loss over epochs obtained by training a model is depicted.

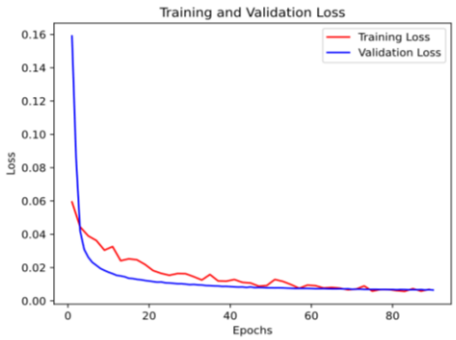

Fig. 1: Training and validation loss over epochs.

Conclusion: We have shown that the use of deep learning-based methods can be useful for generating corrected b matrices, resulting in reduced DTI systematic errors. Future research will focus on removing systematic errors directly from brain MRIs using more advanced neural network architectures.

Acknowledgments: The work was financed by Medical Research Agency contract no: 2020/ABM/01/00006-00.

References:

[1] Bammer R et al., Magn Reson Med. (2003). [2] Krzyżak AT et al., Magn. Reson. Imag. (2015). [3] Hansen, C.B. et al., Magn. Reson. Imag. (2021). [4] Mesri et al., NeuroImage (2020). [5] Borkowski et al., J. Magn. Reson. (2018).

An angle selection method for rSEM

Junqi YANG[1], Shaoying HUANG[2], Yifeng JIANG[1], Tingou Liang[2], Jose GOMEZ TAMES[2]
Wenwei YU[1]
[1]Chiba University, Chiba, Japan, [2]Singapore University of Technology and Design, Singapore

Introduction: Rotating Spatial Encoding Magnetic field (rSEM) with non-linear gradients was used for encoding and imaging in portable MRI with a cylindrical magnet array without gradient coils [1]. The number of rotation angles is linearly proportional to the scan time. And the rotation angle of magnet array will affect the reconstructed image quality because of the mechanically controlled gradient pattern. In this abstract, a method is proposed to select the rotation angles to balance image quality and scan time. Imaging in a Halbach portable system is used as an example to illustrate the method [2].

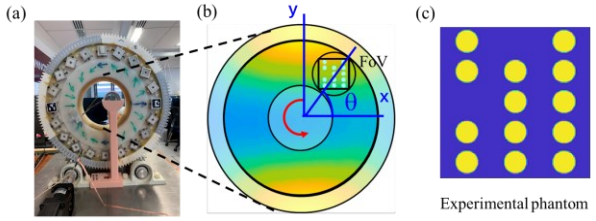

Fig. 1: Experiment setup with the Halbach array based rSEM system and phantom.

Methods: For MRI using rSEM for encoding (Fig.1(a) and (b), the image quality is location dependent, and a normal k-space used in a system with a linear gradient cannot be used while local k-spaces are more appropriate to describe the encoding capability (Fig.2(b) of a field of view (FoV) in Fig.1(b) which is split into 3 x 3 sub-regions). In a local k-space, e.g., Fig.2(a), each rotation angle (θ in Fig.1 (b)) corresponds to a k spoke with a phase angle (ϕ_s) defined by the ratio of the x- and y-component of the gradient fields at that θ at the center of the sub-region. A bigger coverage area corresponds to better image quality. Fig.2 (c) plots ϕ_s versus the number of θ. When ϕ_s of successive angles have a big difference, it compromise the coverage area in the local k-space, degrading image quality (see the red boxes in Fig. 2(c)). Moreover, angles offer the same ϕ_s (see the blue box in Fig. 2(c)) does not offer additional information. Therefore, Using an even distribution of ϕ_s and avoiding θs with the same or similar ϕ_ss are both applied as the criterion of angle selecting for the rSEM. Experiments are conducted in the Halbach array based rSEM system as shown in Fig. 1. Three rotation patterns are designed to validate the angle selection method. First case is 36 times for 360 degrees with even θ interval as shown in Fig. 3a; Second case is the even θs rotation with truncation of the repetitive ϕ_s part as shown in Fig. 3b; The third case is specifically designed to achieve an even distribution of ϕ_s while also ensuring avoidance of θs which will result a repetitive ϕ_s as shown in Fig. 3c.

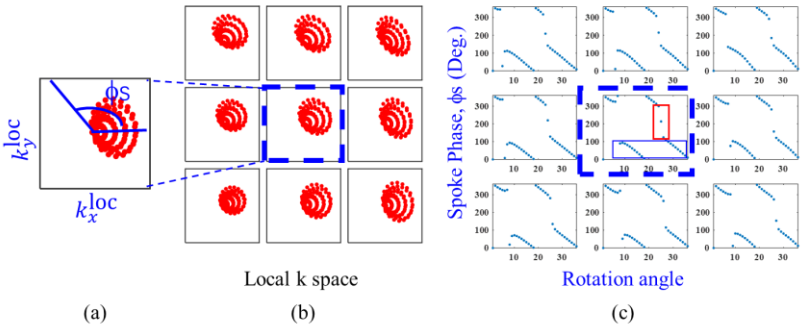

Fig. 2: The phase of k spokes vary with the rotation angle in different location.

Result: The reconstructed image of the phantom (Fig.1(c)) with different rotation angle is shown in the bottom of Fig. 3. Comparing Fig.3(c) to the case in Fig.3(b), more information of the phantom is reconstructed (the circled regions) when the number of angles is the same. Comparing Fig.3(c) to (a), less angles are needed when the image quality are similar. The result validate the higher encoding efficiency of angle selected based on the criterion this work proposed. Besides Comparing Fig.3(b) to (a), it is easy to see that although the truncated angle has the repetitive ϕ_s part, the result is still worse than the without truncation one. It is because the repetitive ϕ_s part contributes to the signal noise ratio (SNR) and make the result better.

Discussion: Since the proposed method aims to generate a uniformed ϕ_s distribution and avoid the rotation angle with repetitive ϕ_s, it is important to acknowledge that the angle selection can be further optimized in at least two aspects. One is taking the magnitude of k spoke into consideration. The magnitude of k spoke can be defined as the length of it or the k_{FOV} used in some research and it also varies at different rotation angles when the non-linear field pattern is applied. High magnitude will result in a high contribution to the resolution. But limited by the space, the magnitude is not considered in this work. A more reasonable angle selection can be achieved if both phase and magnitude of k spoke can be taken into consideration. The other is about the truncation of rotation angle with repetitive ϕ_s. Experimental result shows repetitive ϕ_ss also contribute to the quality of reconstructed image, but it satisfy the scanning time. To further balance the image quality and the scanning time, more investigate on the contribution of repetitive ϕ_s. could be done. Therefore, the proposed angle selection is not yet optimal, and further optimization can be achieved by considering the two aspects mentioned above.

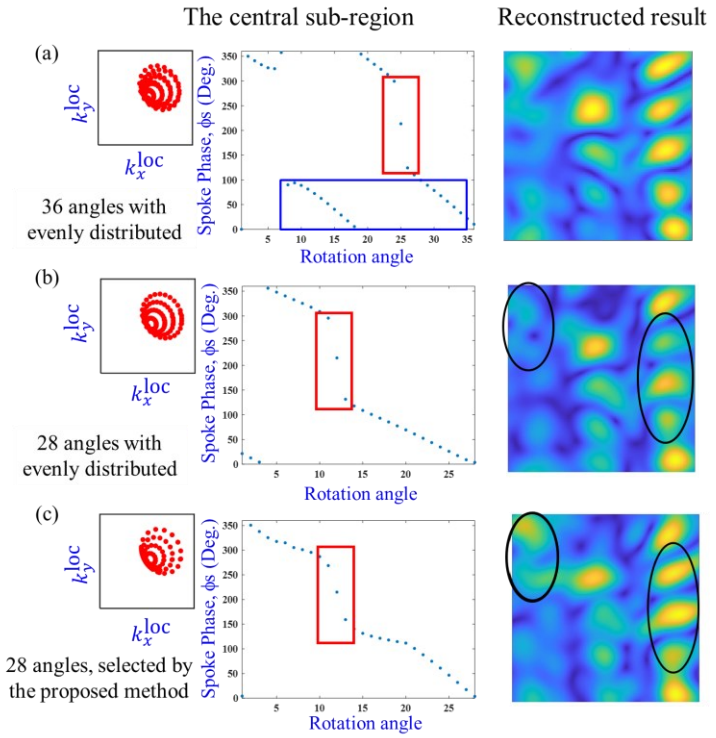

Fig. 3: Three different angle selection pattern and the corresponding reconstructed result

Conclusion: A angle selection method is proposed to improve image quality while reducing scan time for an MRI system using rSEM for encoding with a cylindrical magnet array. The effectiveness of the method was validated using experimental data in a Halbach portable MRI system. The method can be applied to any MRI system using rSEM.

been captured shown in the black circle. The result validates the higher encoding efficiency for the modified rotation pattern. Besides, compared with Fig. 3a, the proposed rotation pattern not only significantly reduces the scanning time by reducing the rotation times from 36 to 28 but also maintains a similar level of reconstructed image quality. This further validates the advantage of the proposed rotation pattern.

References:

[1] C. Z. Cooley, et al., Magn. Reson. Med., (2015)
[2] Z. H. Ren, et al., IEEE MTT-S Int. Microw. Symp. Dig., (2015)
[3] Gallichan D et al., Magn Reson Med., (2011)